UNIVERSITY OF CALIFORNIA, SAN DIEGO

Infrared Nano-Spectroscopy and Nano-Imaging of Graphene Plasmons

A dissertation submitted in partial satisfaction of the
requirements for the degree
Doctor of Philosophy

in

Physics

by

Zhe Fei

Committee in charge:

Professor Dimitri N. Basov, Chair
Professor Massililiano Di Ventra
Professor Michael Fogler
Professor Zhaowei Liu
Professor Mark Thiemens
Professor Congjun Wu

2014

The Dissertation of Zhe Fei is approved, and it is acceptable in quality and form for publication on microfilm and electronically:

_____

_____

_____

_____

_____

_____
Chair

University of California, San Diego

2014

DEDICATION

To my parents, my wife and my daughter.

EPIGRAPH

The most beautiful experience we can have is the mysterious - the fundamental emotion which stands at the cradle of true art and true science.

− Albert Einstein

TABLE OF CONTENTS

LIST OF FIGURES

ACKNOWLEDGEMENTS

First and foremost, I would like to express my deepest gratitude to my advisor Prof. Dimitri Basov for his guidance, support, encouragement and patience in the last five years. I have been extremely lucky to have an advisor like Dimitri who has so strong expertise, intense enthusiasm, deep insights and immense knowledge in physics, and who cared so much about my work, my career and my life.

I would also like to acknowledge other committee members, Prof. Massililiano Di Ventra, Prof. Congjun Wu, Prof. Michael Fogler, Prof. Mark Thiemens, and Prof. Zhaowei Liu, for their time and effort in strengthening my thesis.

I am indebted to all my past and current fellow lab-mates, especially Dr. Gregory Andreev, Dr. Tom Driscoll, Dr. Alexander Schafgans, Dr. Margaret Stewart, Dr. Martin Wagner, Dr. Mengkun Liu, Alexander McLeod, Michael Goldflam, Eric Iwinski, Guangxin Ni, and Siyuan Dai, for their numerous help with instruments and experiments. I would like to thank Prof. Michael Fogler, Prof. Antonio Castro Neto, Dr. Matt Zhang and Dr. Alex Rodin for their theoretical support throughout my thesis work. I would also like to thank Dr. Fritz Keilmann, Dr. Rainer Hillenbrand and other members of Neaspec for sharing their expertise and for bringing us the most powerful instrument in nano-optics. Collaboration with all these brilliant scientists makes life much easier.

I am grateful to my parents for their care and support throughout my life. They are always with me no matter where I am or what I’m doing. I would like to thank my wife

Yan for accompanying me through this journey with her love and support. I couldn't imagine my life without her. Special thanks go to my daughter Irene for bringing me so much joy and happiness. Her smile is the most beautiful thing I have ever seen in my life.

Chapter 2, in full, is a reprint of the material as it appears in Z. Fei, G. O. Andreev, W. Bao, L. M. Zhang, A. S. McLeod, C. Wang, M. K. Stewart, Z. Zhao, G. Dominguez, M.Thiemens, M. M. Fogler, M. J. Tauber, A. H. Castro-Neto, C. N. Lau, F. Keilmann, and D. N. Basov, "Infrared Nanoscopy of Dirac Plasmons at the Graphene-SiO_2 interface", Nano Lett. 11(11), 4701-4705 (2011). The dissertation author was the primary investigator and author of this paper.

Chapter 3, in full, is a reprint of the material as it appears in Z. Fei, A. S. Rodin, G. O. Andreev, W. Bao, A. S. McLeod, M. Wagner, L. M. Zhang, Z. Zhao, G. Dominguez, M.Thiemens, M. M. Fogler, A. H. Castro-Neto, C. N. Lau, F. Keilmann, and D. N. Basov, "Gate-tuning of graphene plasmons revealed by infrared nano-imaging", Nature 487, 82–85 (2012). The dissertation author was the primary investigator and author of this paper.

Chapter 4, in full, is a reprint of the material as it appears in Z. Fei, A. S. Rodin, W. Gannett, S. Dai, W. Regan, M. Wagner, M. K. Kiu, A. S. McLeod, G. Dominguez, M.Thiemens, M. M. Fogler, A. H. Castro-Neto, F. Keilmann, A. Zettl, R. Hillenbrand, M. M. Fogler, and D. N. Basov, "Electronic and plasmonic phenomena at graphene grain

boundaries", Nature Nanotech. 8, 821-825 (2013). The dissertation author was the primary investigator and author of this paper.

Chapter 5, in part, is currently being prepared for submission for publication of material. Z. Fei, E. G. Iwinski, G. X. Ni, L. M. Zhang, W. Bao, A. S. Rodin, Y. Lee, M. Wagner, M. K. Liu, S. Dai, M. D. Goldflam, F. Keilmann, C. N. Lau, A. H. Castro Neto, M. M. Fogler, and D. N. Basov, "Infrared nano-imaging of surface plasmons in bilayer graphene revealing an effective plasmon-off state". The dissertation author was the primary investigator and author of this paper.

VITA

2006	B.S. in Physics, Nanjing University
2006-2009	Graduate Student Researcher, Nanjing University
2009	M.S. in Physics, Nanjing University
2009-2014	Graduate Student Researcher, University of California, San Diego
2014	Ph.D. in Physics, University of California, San Diego

PUBLICATIONS

Z. Fei, E. G. Iwinski, G. X. Ni, L. M. Zhang, W. Bao, A. S. Rodin, Y. Lee, M. Wagner, M. K. Liu, S. Dai, M. D. Goldflam, F. Keilmann, C. N. Lau, A. H. Castro Neto, M. M. Fogler, and D. N. Basov, "Infrared nano-imaging of surface plasmons in bilayer graphene revealing an effective plasmon-off state", In preparation (2014).

M. K. Liu, M. Wagner, J. Zhang, A. S. McLeod, S. Kittiwatanakul, Z. Fei, E. Abreu, M. Goldflam, A. Sternbach, S. Dai, K. West, M. M. Fogler, J. Lu, A. Stuart, D. N. Basov, "Symmetry breaking and geometric confinement in VO2: Results from a three-dimensional infrared nano-imaging", Appl. Phys. Lett. 104, 121905 (2014).

S. Dai, Z. Fei, A. S. Rodin, W. Gannett, M. Wagner, W. Regan, A. S. McLeod, M. Liu, M. Thiemens, G. Dominguez, A. H. Castro Neto, A. Zettl, F. Keilmann, M. M. Fogler, D. N. Basov, "Tunable Phonon Polaritons in Atomically Thin van der Waals Crystals of Boron Nitride", Science 343, 1125-1129 (2014).

M. Wagner, Z. Fei, A. S. McLeod, A. S. Rodin, W. Bao, E. G. Iwinski, Z. Zhao, M. Goldflam, M. K. Liu, G. Dominguez, M. Thiemens, M. M. Fogler, A. H. Castro Neto, C. N. Lau, S. Amarie, F. Keilmann, and D. N. Basov, "Ultrafast and Nanoscale Plasmonic Phenomena in Exfoliated Graphene Revealed by Infrared Pump-Probe Nanoscopy", Nano Lett. 14 (2), 894–900 (2014).

Z. Fei, A. S. Rodin, W. Gannett, S. Dai, W. Regan, M. Wagner, M. K. Kiu, A. S. McLeod, G. Dominguez, M. Thiemens, A. H. Castro Neto, F. Keilmann, A. Zettl, R. Hillenbrand, M. M. Fogler, D. N. Basov, “Electronic and plasmonic phenomena at graphene grain boundaries”, Nature Nanotech. 8, 821-825 (2013).

M. K. Liu, M. Wagner, E. Abreu, S. Kittiwatanakul, A. S. McLeod, Z. Fei, M. Goldflam, S. Dai, M. Fogler, J. Lu, S. A. Wolf, R. D. Averitt, D. N. Basov, “Anisotropic electronic state via spontaneous phase separation in strained Vanadium dioxide films”, Phys. Rev. Lett. 111, 096602 (2013).

A. S. Rodin, Z. Fei, A. S. McLeod, M. Wagner, A. H. Castro Neto, M. M. Fogler, and D. N. Basov, “Plasmonic hot spots in triangular tapered graphene microcrystals”, Submitted to Phys. Rev. B (2014).

Z. Fei, A. S. Rodin, G. O. Andreev, W. Bao, A. S. McLeod, M. Wagner, L. M. Zhang, Z. Zhao, M.Thiemens, G. Dominguez, M. M. Fogler, A. H. Castro Neto, C. N. Lau, F. Keilmann, D. N. Basov, "Gate-tuning of graphene plasmons revealed by infrared nano-imaging", Nature 487, 82–85 (2012).

L. M. Zhang, G. O. Andreev, Z. Fei, A. S. McLeod, G. Dominguez, M. Thiemens, A. H. Castro Neto, D. N. Basov, and M. M. Fogler, "Near-field spectroscopy of silicon dioxide thin films", Phys. Rev. B 85, 075419 (2012).

Z. Fei, G. O. Andreev, W. Bao, L. M. Zhang, A. S. McLeod, C. Wang, M. K. Stewart, Z. Zhao, G. Dominguez, M. Thiemens, M. M. Fogler, M. J. Tauber, A. H. Castro Neto, C. N. Lau, F. Keilmann, and D. N. Basov, “Infrared Nanoscopy of Dirac Plasmons at the Graphene-SiO_2 interface”, Nano Lett. 11(11), 4701-4705 (2011).

M. K. Liu, B. Pardo, J. Zhang, M. M. Qazilbash, Sun Jin Yun, Z. Fei, Jun-Hwan Shin, Hyun-Tak Kim, D. N. Basov, and R. D. Averitt “Photo-induced Phase Transitions by Time-Resolved Far-Infrared Spectroscopy in V_2O_3”, Phys. Rev. Lett. 107, 066403 (2011).

Z. Fei, Y. Shi, L. Pu, F. Gao, Y. Liu, L. Sheng, B. Wang, R. Zhang, and Y. Zheng, “High-energy optical conductivity of graphene determined by reflection contrast spectroscopy”, Phys. Rev. B 78, 201402 (2008).

ABSTRACT OF THE DISSERTATION

Infrared Nano-Spectroscopy and Nano-Imaging of Graphene Plasmons

by

Zhe Fei

Doctor of Philosophy in Physics

University of California, San Diego, 2014

Professor Dimitri N. Basov, Chair

This dissertation presents infrared nano-spectroscopy and nano-imaging studies of graphene plasmons using scattering-type scanning near-field microscope – a unique technique allowing efficient excitation and high-resolution imaging of graphene plasmons. With this technique, we show in real space that common graphene/SiO_2/Si back-gated structure support propagating surface plasmons in the infrared frequencies.

The observed plasmons are highly confined surface modes with a wavelength around 200 nm that are conveniently tunable by the back gate voltages. In addition, we perform spectroscopic studies on graphene by varying the probing frequencies. The spectroscopy results not only show direct signature of graphene plasmons but also provide evidence of strong coupling between graphene plasmons and SiO_2 optical phonons. Furthermore, we investigate the plasmonic properties of Bernal-stacking bilayer graphene (BLG) and find that BLG supports gate-tunable infrared plasmons with higher confinement compared to graphene and randomly stacked graphene layers. Moreover, BLG plasmons can be turned off completely in wide gate voltage close to the charge neutrality point. Those unique plasmonic properties are attributed to both interlayer tunneling and bandgap opening in BLG. Finally, we are able to map and characterize grain boundaries inside graphene film fabricated with chemical vapor deposition (CVD) method by launching surface plasmons. We found grain boundaries, as well as other line defects in CVD graphene, trigger distinct plasmonic twin fringes patterns due to plasmon interference. Theoretical modeling and analysis unveil unique electronic properties associated with grain boundaries.

Chapter 1

Introduction

Plasmonics, which is surface plasmon based nanophotonics, merges electronics and photonics at the nanometer length scale. It is promising for future applications in nanoscale information transfer, photodetection nanosensing, and transformation optics. Graphene was predicted to be a novel plasmonic material supporting propagative surface plasmons since years ago. But this remains a prediction other than an established fact only until recently, when groundbreaking works about nano-spectroscopy and nano-imaging of graphene plasmons were reported.

In this dissertation, we employ tip-based infrared nanoscope to investigate graphene plasmons both in both frequency space and real space. Our nanoscope, which is called scattering-type scanning near-field microscope (s-SNOM), allows us to investigate infrared properties of samples with nanometer scale resolution and wide momenta range. This technique has been widely applied in studying surface phonon polariton of polar materials, surface plasmon polaritons of bulk metals, metal-insulator transitions and so on.

As shown in Fig. 1.1, the s-SNOM is built based on a tapping-mode atomic force microscope (AFM). The AFM tip that is illuminated by infrared light from various laser sources acts like both launcher and probe of graphene plasmons underneath it.

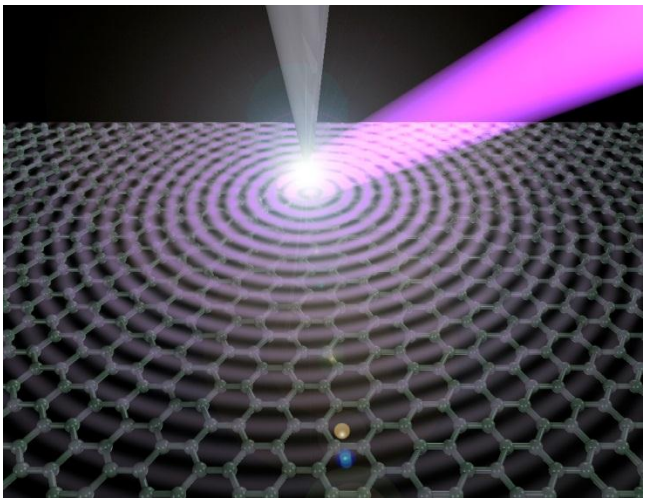

Figure 1.1: Launch and probe graphene plasmons with tip-based nanoscope.

In Chapter 2 we introduce the first nano-spectroscopy of graphene plasmons revealing strong plasmon-phonon interaction. Infrared nano-spectroscopy has becoming a powerful technique in characterizing and fingerprinting materials with nanoscale resolution. In our experiment, in order to gain spectral properties of graphene, we employed both tunable continuous-wave lasers and broadband pulse lasers as excitation sources in our nano-optic system. Those lasers cover a broad range of mid-infrared frequencies, where the most dominate spectra feature is a strong resonance originated from the surface optical phonon of SiO_2 at around 1130 cm^{-1}. Remarkably, graphene, one

atomic layer of carbon atoms, greatly enhances the resonance and causes obvious blue-shift to higher frequencies. Further analysis and modeling indicate that such enhancement and blue-shift are due to strong coupling between graphene plasmons and SiO_2 surface optical phonons. Our spectroscopy results not only show direct signature of graphene plasmons but also provide evidence of strong mode-repulsion phenomenon that strongly enhance the light-matter interaction in the nanometer length scale. Such a novel phenomenon can only be observed in nano-optic regime thus has never been reported in traditional far-field optics.

In Chapter 3 we introduce the first nano-imaging of gate-tunable propagating graphene plasmons. By using s-SNOM operating in the mid-infrared frequencies, we showed for the first time the real-space features of graphene plasmons. Quantitative analysis unveiled all the essential properties of graphene plasmons such as confinement, damping, reflection, interference and so on. According to our experiments, graphene plasmons appear at infrared frequencies with higher confinement and relative lower losses compared to plasmons in noble metals. In addition, we were able to control and manipulate graphene plasmons by back gating – a common structure similar to the state-of-the-art MOSFET. Furthermore, we found that the plasmon damping in graphene is much higher than theoretical predictions based on a single-particle picture. Such a high damping was attributed to many-body physics such as electron-electron interaction, electron-phonon interaction and so on.

Chapter 4 introduces a novel nano-characterization technique based on surface plasmon interference and how we implemented this technique in characterization of electronic and plasmonic properties of atomic scale line defects in graphene fabricated with chemical vapor deposition (CVD) method. For centuries, scientists strive to design more efficient and effective techniques to characterize material structures and properties. Those techniques apply various types of probing media such as photons, electrons, neutrons, scanning probes and so on. We demonstrated for the first time that surface plasmons are also powerful probing media for surface nano-characterization. The general mechanism is based on the fact that plasmon waves are able to be reflected or scattered by any physical or electronic discontinuities. And interference between launched and reflected/scattered waves generates real-space patterns containing rich information about the sample surface. We showed that this method enables high resolution, high efficiency, and spectroscopic study of surface nanostructures in ambient conditions. It can be widely applied in any plasmonic materials, such as metals, superconductors, topological insulators, graphene, and so on. Our testing sample is graphene fabricated with CVD method. We were able to map and characterize grain boundaries in CVD graphene film by exploring real space patterns of propagating surface plasmons. We found that grain boundaries trigger distinct plasmonic features due to plasmon interference. Further modeling and analysis indicate that grain boundaries form electronic barriers that impede both charge transport and plasmon propagation.

Lastly, Chapter 5 introduces the first nano-imaging of surface plasmons in bilayer graphene (BLG) − closest relative of graphene. BLG shares nearly all the supreme electrical, mechanical and thermal properties of graphene. Nevertheless, it has many unique electronic properties, such as split bands due to interlayer coupling, field-induced bandgap, massive quasiparticles close to charge neutrality point, et al. All these fundamental properties make BLG behave differently from graphene in (opto)electronic responses and functionalities. By using s-SNOM, we demonstrate that BLG also support gate-tunable surface plasmons in the mid-infrared frequencies, with nevertheless higher confinement compared to graphene and randomly-stacked graphene layers. More interesting, these plasmons can be turned off effectively and efficiently by back gate voltages. Further analysis indicated that these intriguing plasmonic properties were attributed to both interlayer tunneling and bandgap opening in BLG.

Chapter 2

Infrared nanoscopy of Dirac plasmons at the graphene-SiO_2 interface

2.1 Abstract

We report on infrared (IR) nanoscopy of 2D plasmon excitations of Dirac fermions in graphene. This is achieved by confining mid-IR radiation at the apex of a nanoscale tip: an approach yielding two orders of magnitude increase in the value of in-plane component of incident wavevector q compared to free space propagation. At these high wavevectors, the Dirac plasmon is found to dramatically enhance the near-field interaction with mid-IR surface phonons of SiO_2 substrate. Our data augmented by detailed modeling establish graphene as a new medium supporting plasmonic effects that can be controlled by gate voltage.

2.2 Introduction

Surface plasmons are fundamental collective modes of electrons that enable functionalities at the intersection of nanophotonics and electronics [1-5]. Dirac plasmons of graphene, which are the density waves of Dirac fermions, are predicted to enable both low loss and efficient wave localization up to mid-IR frequencies [6-10]. Theoretical studies show that the combination of tunability and low loss is highly appealing for implementation of nanophotonics, optoelectronics, and transformation optics based on Dirac plasmons [9-12]. Electron-energy-loss spectroscopy studies of epitaxial graphene on SiC substrate verified plasmonic effects [13-15]. So far, optical phenomena associated with surface plasmons of the massless quasi-particles in graphene have remained unexplored. This is in part due to the difficulty of carrying out IR experiments at wavevectors matching those of plasmons, which are beyond the reach of conventional transmission or reflection measurements [16]. To overcome this limitation, we employed scattering-type scanning near-field optical microscope (s-SNOM). Previously, this technique was widely applied to studying surface phonons and phonon polaritons [17,18]. In this letter, we identified spectroscopic signatures attributable to the Dirac plasmon and its interaction with the surface phonon of the SiO_2 substrate. Our work affirms the under-exploited capability of tip-based optical nanoscopy to probe collective charge modes far away from $q \sim 0$ of conventional optical spectroscopy.

2.3 Experimental details

In our experiments, we utilized a commercial s-SNOM (NeaSNOM, neaspec.com) coupled to several interchangeable lasers: two quantum cascade lasers (daylightsolution.com) and two CO_2 lasers (accesslaserco.com). These lasers allow coverage of the mid-IR region from 883 to 1270 cm^{-1} (Figs. 2.1 and 2.2). This region accommodates characteristic features of the electromagnetic response of monolayer graphene [19-21] along with vibrational modes of SiO_2. The IR nanoscope is built on the basis of an Atomic Force Microscope (AFM) operating in tapping mode. We acquired near-field images with tapping frequency $\Omega \sim 270$ kHz and tapping amplitude $\Delta z = 40$ nm at ambient conditions. The back-scattered signal is demodulated at the 2^{nd}, 3^{rd} and 4^{th} harmonics of the tapping frequency yielding background-free images [22]. The scattering amplitude s and phase ϕ at all harmonics are obtained simultaneously with AFM topography by pseudo-heterodyne interferometric detection [23].

Figure 2.1a displays a schematics of the nanoscopy experiment. The beam of an IR laser is focused on the metalized tip of an AFM cantilever. The strong near-field confinement of mid-IR radiation at the tip apex has two principal effects. First, the collection of back-scattered light from a confined volume characterized by the tip radius a enables IR imaging/spectroscopy at sub-diffractional resolution [22]. Second, the light-matter interaction induced at the vicinity of the tip peaks for in-plane momenta $q \approx 1/a$ far beyond the light line given by $q = \omega/c$. It is this combination of high spatial

resolution and high-q coupling that enables us to investigate the spectroscopic signatures of Dirac plasmons by means of IR nanoscopy.

Graphene samples were fabricated by mechanical cleavage of graphite and then transferred to the surface of a 300 nm thick SiO_2 on a Si wafer. Commonly, graphene on SiO_2 is characterized by a rather high carrier density due to unintentional doping [24,25]. Raman spectroscopy [26] was used to select monolayer samples with nearly identical hole doping $n = (2.9 \pm 1.0) \times 10^{12}$ cm^{-2} corresponding to a chemical potential of $|\mu| = (1600 \pm 300)$ cm^{-1} that we determined as $|\mu| = \hbar v_F \sqrt{\pi n}$ ($v_F \approx 1\times 10^6 m/s$ is the Fermi velocity of graphene). The uncertainty in the estimate of the graphene chemical potential is due to ambiguities in Raman measurements of the carrier density as well as data for the Fermi velocity of graphene. For the purpose of absolute spectroscopic measurements, we etched off SiO_2 in several regions of the wafer to access the Si surface. The near-field response of Si is frequency-independent in the mid-IR region. Therefore, Si can serve as a convenient reference for a quantitative analysis of the nanoscale electrodynamics of graphene on SiO_2. For gating experiments, we fabricated electric contacts to the graphene surface. By varying back-gate voltage V_g, we are able to tune the carrier density of graphene $n = C_g \times |V_g - V_{CN}|/e$, where $C_g = 115$ aF μm^{-2}, and V_{CN} is the gate voltage corresponding to the charge neutral graphene.

2.4 Experimental data

In Fig. 2.1b we show representative IR nanoscopy images, in which we plot the backscattering amplitude normalized to Si: $s(\omega) = s_3(\omega) / s_3^{Si}(\omega)$. Here, the backscattering amplitude $s_3(\omega)$ is demodulated at the 3rd harmonic of the tip tapping frequency. The simultaneously recorded AFM topography is displayed in Fig. 2.4 in the Supplementary Information. These images reveal nearly uniform signals in either SiO_2 or graphene regions with characteristics varying systematically with IR frequency. In Fig. 2.2a,c we present these results in the form of both amplitude $s(\omega)$ and phase $\phi(\omega) = \phi_3(\omega) - \phi_3^{Si}(\omega)$ spectra. Each data point in Fig. 2.2a,c was obtained by averaging over corresponding areas in images similar to those displayed in Fig. 2.1b.

We first consider the amplitude spectra of SiO_2 which reveal a near-field resonance centered at ω = 1128 cm^{-1} due to the surface phonon of SiO_2 in accord with the earlier data [27,28]. The dominant feature of the $s(\omega)$ spectrum for graphene on SiO_2 is similar to that for SiO_2 alone. However, the most surprising finding is that graphene strongly enhances the amplitude $s(\omega)$ in the 1110 - 1250 cm^{-1} spectral region and also blue-shifts the peak frequency by about 10 cm^{-1}. We hypothesize that both effects are related to the high density of mobile carriers present in our graphene samples. In order to verify this hypothesis, we monitored the evolution of the resonance with gating voltage V_g that enables controlled variation of the carrier density in graphene. In the inset of Fig. 2.2a, we show the results of gating experiments performed at ω = 1150 cm^{-1} where

graphene-induced enhancement of the scattering amplitude is most prominent (160% compared to SiO_2). At negative V_g corresponding to the increase of the hole density, the scattering amplitude is further enhanced (up to 300% at V_g = -50 V). On the contrary, positive V_g, which reduces the hole density, significantly suppresses the contrast between graphene and the oxide. The contrast is minimized at $V_g = (40 \pm 5)$ V, which we assign to charge neutrality voltage V_{CN}. This estimate of V_{CN} is in accord with the Raman probe of the carrier density in ungated graphene layers (see Supplementary Information). In addition, graphene induces a steep increase of the near-field phase below 970 cm^{-1} (Fig. 2.2c). We will show that the latter effect stems from direct interaction of ultra-localized IR light with the Dirac plasmon whereas SiO_2 resonance modifications originate from plasmon-phonon coupling at the graphene-SiO_2 interface.

2.5 Theory and Analysis

2.5.1 Near-field coupling

The physics of the near-field interaction is that the tip, polarized by incident IR light, gives rise to evanescent fields with a wide range of in-plane momenta q. When the tip approaches a polar and/or conducting surface, the evanescent fields are altered which in turn affects the tip polarization. To quantify this interaction we introduce the reflection coefficient, $r_P(q,\omega)$, defined as the ratio of the amplitude of the P-polarized reflected field E_r to that of the P-polarized incident field E_i. This frequency- and momentum-dependent

response function completely describes the electrodynamics of the graphene-SiO_2 interface, not only in the near field, but also in the far field (see Supplementary Information):

$$r_P(q,\omega) = \frac{\varepsilon_1 k_0 - \varepsilon_0 k_1 + (4\pi k_0 k_1 \sigma / \omega)}{\varepsilon_1 k_0 + \varepsilon_0 k_1 + (4\pi k_0 k_1 \sigma / \omega)} \tag{2.1}$$

In Eq. 2.1, ε_0 is the dielectric constant of vacuum, ε_1 is the complex dielectric function of SiO_2, $k_j = \sqrt{\varepsilon_j (\omega/c)^2 - q^2}$ are the out-of-plane components of momenta, and $\sigma = \sigma(q,\omega)$ is the in-plane optical conductivity of graphene that was obtained from the Random Phase Approximation (RPA) method (see Supplementary Information).

From Eq. 2.1, one can see that the in-plane properties of graphene are responsible for its response in sSNOM experiments. This is possibly due to the radial component of the tip's scattered field, which drives charges within graphene. Likewise, these charges impact the tip polarization in response. Note that $r_P(q,\omega)$ diverges at q and ω values given by the dispersion of the two surface modes at the graphene/SiO_2 interface: the SiO_2 surface phonons 1128 cm^{-1} and Dirac plasmon of graphene. A formal connection between $r_P(q,\omega)$ and the direct experimental observable of IR nanoscopy, $se^{i\phi}$, is worked out in the Supplementary Information (Eq. 2.4) by modeling the apex of the tip as a point dipole. Here we only briefly comment on the essential aspects of the modeling procedure. An important parameter of our point-dipole model is the AFM tip radius a, which we have set at a = 30 nm according to the specifications of our cantilevers. The tip radius

determines the effective dipole polarizability a^3. Another significant parameter b is the distance between the point dipole and the apex of the tip. Finally, we stress the central result of the dipole-model analysis: the near-field coupling integral G has the weight function of the form $q^2 \exp(-2qz_d)$, where $z_d = b+\Delta z(1-\cos\Omega t)$ is the distance between the tip dipole and the sample surface (Eq. 2.3 in Supplementary Information). The magnitude of z_d is varying with time due to tip tapping. The plot of the time-averaged weight function $\left\langle q^2 \exp(-2qz_d)\right\rangle_t$ reveals a bell-shaped momentum dependence that peaks around $q = 1/a$ (Fig. 2.3a). Thus the dominant in-plane momenta contributing to near-field coupling are distributed around $q = 1/a$ (dashed line in Fig. 2.3a-d). For that reason, the $s(\omega)$ spectra show resonances if and only if the dispersion curve of a mode intersects the dashed line that marks the dominant near-field momentum. For a typical value of our tip radius, a = 30 nm, the probing in-plane momentum exceeds that of the incident light at $\omega \sim 1000$ cm^{-1} by about two orders of magnitude. These virtues of tip-enhanced near-field coupling enable the exploration of both the Dirac plasmon of graphene and plasmon-phonon coupling, which are fundamentally finite-momenta effects.

2.5.2 Near-field modeling

The dipole model of the near-field interaction [17,27-30], which we have adapted to the graphene-SiO_2 interface and augmented with the explicit account of the

high-momentum coupling, reproduces all aspects of the data (Fig. 2.2b,d). We first consider the near-field spectra of SiO_2. Comparing the results of dipole-model calculations with measurements, we find near quantitative agreement. Despite overall agreement between the data and modeling, one witnesses minute discrepancies that may stem from two main factors. First, we used bulk optical constants of SiO_2 extracted from far-field ellipsometry measurements of our wafers in modeling the surface response (see Supplementary Information). Second, the point-dipole model neglects the actual geometry of the tip that may introduce finite dipole or even higher multi-poles to the near-field interaction [28,31,32].

We now proceed to describe the dipole-model results for graphene on SiO_2. In Fig. 2.2b,d we plot spectra of both amplitude and phase, displaying the evolution of the near-field response with variations in the chemical potential μ. For the specific choice of $|\mu| = 1600$ cm^{-1} (consistent with our Raman measurements and also gating experiments), we find that the model spectra reproduce the key characteristics of the data: enhancement of the resonance and its blue shift. The net result is that the Dirac plasmon of graphene radically modifies the SiO_2 surface phonon response, which is the experimental manifestation of the plasmon-phonon interaction at the graphene/SiO_2 interface.

2.5.3 Plasmon dispersion

In order to map the dispersion of the plasmon, we evaluated the divergence of

$r_P(q,\omega)$ using Eq. 2.1 (Fig. 2.3c,d). The dispersion of the Dirac plasmon approximately follows the square-root q-dependence $\omega_P(q) \propto v_F\sqrt{k_F q}$ for q values smaller than the Fermi wavevector k_F [33]. Moreover, the plasmon frequencies are also governed by the chemical potential or carrier density n in the graphene layer since $k_F = \sqrt{\pi n}$. The value of the chemical potential also determines the onset of interband transitions and cut-offs for intraband excitations [20] (white dotted lines in Fig. 2.3b-d). Within the RPA approximation and considering constant scattering rate of quasiparticles in graphene (due to phonons or impurities), the chemical potential alone defines the optical conductivity of graphene in the mid-IR region (see Supplementary Information) [19,20,34].

In weakly doped graphene, the Dirac plasmon and the surface phonon of SiO_2 are well separated from each other (Fig. 2.3b). Both modes can be excited in the near-field experiment since their dispersion curves fall within the momentum range of the probe. We note here that surface phonons are extremely localized in real space: a product of their nearly flat dispersion. In contrast, the Dirac plasmon of graphene is a propagating mode, and the real-space aspects of this plasmon will be a subject of future imaging experiments. At moderate levels of carrier density, the plasmon approaches the surface phonon of SiO_2 leading to the familiar effects of mode repulsion and hybridization (Fig. 2.3c). Increasing the carrier density further leads to drastic changes in the dispersion of both the plasmon and the surface phonon (Fig. 2.3d). In panels Fig. 2.3b-d one can also notice a structure near 850 cm^{-1} originating from the plasmon coupling to a weaker

low-frequency phonon mode of SiO_2.

The dipole model predicts that the plasmon-phonon interaction and hybridization at the graphene-SiO_2 interface (Fig. 2.3b-d) can be readily observed by near-field nanoscopy. We focus again on the chemical potential $|\mu|$ = 1600 cm^{-1}. The dipole model calculations show that the anti-crossing of the Dirac plasmon and the phonon not only causes the blue shift of the peak in $s(\omega)$ spectra but also increases the strength of the resonance (Fig. 2.2b). Both effects were observed by our experiment. Furthermore, the model predicts the systematic variation of the scattering amplitude with the chemical potential in the 1100 - 1250 cm^{-1} range, which was observed by our gating experiments (inset of Fig. 2.2a). Because graphene on SiO_2 is unintentionally doped, the enhancement of $s(\omega)$ is expected to show an non-monotonic variation with the gate voltage, and have the minimum near charge neutrality point. This is also in accord with the data presented in the inset of Fig. 2.2a. In combination, near-field spectra in Fig. 2.2 and gating data at a selected probing frequency attest to the hybrid character of the resonance, involving coupled plasmon-phonon oscillations which dominate the mid-IR response of the graphene-SiO_2 interface. One can also anticipate a hardening of the phonon resonance of SiO_2 due to screening associated with mobile charge in the graphene layer, a complimentary viewpoint on the effects reported in Fig. 2.2a.

2.5.4 Direct signature of plasmon mode

Yet another salient feature of the modeled spectra is a strong near-field resonance close to the low-energy cut-off of our data (Fig. 2.2b,d), which originates from the direct near-field coupling to the Dirac plasmon of graphene. This low-frequency resonance is clearly broadened compared to the hybrid plasmon-phonon mode discussed above. A detailed discussion about the linewidth of both modes is provided in the Supplementary Information. Resonance structure due to the Dirac plasmon is clearly visible both is in the $s(\omega)$ and $\phi(\omega)$ spectra (Fig. 2.2b,d); these features systematically shift to higher frequencies with increasing doping level of graphene. For $|\mu|$ = 1600 cm^{-1}, the amplitude resonance of the Dirac plasmon appears at ω = 600 cm^{-1}, which is beyond the accessible range of our lasers. Modeling also shows that the feature in the phase spectra $\phi(\omega)$ originating from the Dirac plasmon occurs at higher frequency compared to the amplitude spectra, and can therefore be probed by our experimental setup (Fig. 2.2d). We attribute the observed increase of the phase at low frequencies (Fig. 2.2c) to direct near-field coupling to the Dirac plasmon. This finding, along with the fingerprints of plasmon-phonon interaction, establishes graphene as a new medium supporting plasmonic effects. Unlike noble metals: traditional materials supporting surface plasmons, graphene is inherently tunable by electric and magnetic fields, thus enabling functionalities not attainable with metal plasmonics.

2.6 Conclusion and Outlook

The combination of high-momentum spectroscopy and nano-imaging demonstrated in our work sets the stage for studying many other properties of Dirac plasmons in graphene. Of special interest are effects pertaining to the real-space confinement and propagation of plasmons in nano-structures/ribbons [35,36]. A modification of the plasmon dispersion and/or ultra-fast modulation [37] of the Dirac plasmon can be conveniently carried out through back-gating with a degree of control that is difficult to obtain within all-metal plasmonics. Turning to the high-q spectroscopy aspects of tip-induced light-matter interaction, we wish to point out that a much broader range of q may be interrogated using super sharp silicon tips (a < 10 nm) and even sharper tips based on carbon nano-tubes (a down to 1 nm) [38]. Such a further expansion of the momentum space accessible by IR nanoscopy, combined with the improved spatial resolution, is especially appealing in the context of studying collective modes in the vicinity of the single-particle excitation continuum, and manipulating light in graphene-based nanostructures or transformation optics elements.

2.7 Supplementary information

2.7.1 Addition experimental information

AFM images were collected simultaneously with the infrared (IR) images displayed in Fig. 2.1b. In Fig. 2.4, we show two separate parts of a typical AFM image

together with two height profiles. The profile across the SiO_2/graphene boundary shows about 1 nm thickness which is typical for exfoliated monolayer graphene on SiO_2/Si substrate. The profile across the Si/SiO_2 boundary shows that the 300 nm thick SiO_2 layer is etched away in the left part where we can get access to the Si surface. Thus, we are able to use Si as the reference for quantitative near-field analysis of both SiO_2 and graphene on SiO_2.

The approach curves shown in Fig. 2.5 measure the IR amplitude as a function of the separation between the oscillating tip apex and the sample surface. The observed sharp decrease within a 20 nm scale verifies that the experimental parameters are set to record the genuine near-field interaction [31].

Raman spectroscopy was used to select monolayer graphene samples with nearly identical doping level. According to Refs. 24 and 25, ungated graphene can be doped either by SiO_2 substrate or ambient atmosphere. Raman spectroscopy was performed with a homebuilt Raman microscope system using excitation at 514.5 nm provided by mixed-gas Kr-Ar laser (Coherent Innova 70C). In Fig. 2.6, we show Raman spectra for two graphene samples studied in this work (Figs. 2.1 and 2.2). We stress that the 2D mode reveals symmetric single peak for both samples. The full widths at half maximum (FWHM) of the 2D mode are 29 and 27 cm^{-1} for sample 1 and 2 respectively. Both facts attest that the samples are monolayer graphene [40,41]. The Raman shift for the G mode of both samples is close to (1587.6 $\pm$ 0.2) cm^{-1} corresponding to charge density of $n = (2.9 \pm 1.0) \times 10^{12}$

cm^{-1} according to Ref. 26. This carrier density yields the chemical potential $|\mu|$ = (1600 ± 300) cm^{-1} calculated with $|\mu| = \hbar v_F \sqrt{\pi n}$ (v_F = 1.0 × 10^6 m/s is the Fermi velocity of graphene,). Therefore the charge neutral point in either sample is expected to be close to V_{CN} = 40 V for our back-gated structures with 300 nm of SiO_2 gate insulator. In such structure, $n = C_g \times |V_g - V_{CN}|/e$, where C_g = 115 aF μm^{-2}, and V_{CN} is the gate voltage corresponding to the charge neutral graphene. The expectation of V_{CN} here is consistent with our near-field gating result (inset of Fig. 2.2a).

In order to model the near-field response of our SiO_2/Si wafers we performed ellipsometric characterization of these wafers. We performed the measurement using commercial IR-VASE Woollam ellipsometer capable of covering the frequency range 400 - 5600 cm^{-1}. Ellipsometric data were acquired at incident angles of 60^o and 75^o at room temperature. By constructing a two-layer model for the SiO_2/Si substrate and fitting the two ellipsometry parameters Ψ and Δ defined by the equation $\tan(\psi)e^{i\Delta} = R_P / R_S$, where R_P and R_S are the reflection coefficients for *P*- and *S*-polarized light, we are able to get the optical constants of SiO_2 that are shown in Fig. 2.7.

2.7.2 Point-dipole model

The experimental technique used in this work is commonly referred to as scattering-type scanning near-field optical microscopy (s-SNOM) [28,29]. Our theoretical analysis follows the formalism developed previously for multilayer systems [27] with

some modifications needed to account for the 2D nature of graphene.

The measured s-SNOM signal represents the electromagnetic field backscattered by the tip and the scanned sample. In the tapping mode, the distance z between the sample and the tip apex undergoes harmonic oscillations with a typical tapping amplitude Δz = 40 nm. As a result, the complex amplitude $s(\omega,t)$ of the backscattered field varies periodically with the tapping frequency Ω. The experimental observables are the absolute values $s_n(\omega)$ and phases $\phi_n(\omega)$ of n-th tapping harmonics. Extracting s_n and ϕ_n from $s(\omega,t)$ is termed demodulation. The data presented in the Figs. 2.1 and 2.2 were demodulated at order n = 3. The demodulation suppresses the unwanted background and isolates the part of the signal scattered by the appex of the tip (size of tip radius a). Therefore, the demodulation procedure allows one to study the genuine near-field interaction between the tip and the sample, which modifies the dipole moment $\mathbf{p}(z)e^{-\omega t}$ induced on the tip by the incident light.

Previous s-SNOM studies demonstrated that the dipole moment **p** can be computed analytically if the tip is approximated by a spheroid [32,42,43], a small sphere [43-47], a “finite” dipole [28,31], or a point dipole [29,27,30]. Adopting the last model, we characterize the tip by two parameters: tip radius a that determines the tip polarizability a^3, and the distance b between the effective dipole and the tip apex. Tip radius a = 30 nm accrding to manufacturer specifications. The distance between the dipole and the sample interface is therefore:

$$z_d(t) = b + z(t) = b + \Delta z(1 - \cos\Omega t). \tag{2.2}$$

Considering that the actual AFM tip has the highest polarizability along its longest dimension (similar to an antenna), we used *P*-polarized incident light to get maximum tip polarization in our experiment. The reflection coefficient $r_P(q, \omega)$ for the *P*-polarization is important for computing the tip-sample coupling function *G*:

$$G(z_d, \omega) = \int_0^\infty dq\, q^2 e^{-2qz_d} r_P(q, \omega). \tag{2.3}$$

The weight function $q^2 e^{-2qz_d}$ inside the integral is a function of time. Time averaged result $< q^2 e^{-2qz_d} >_t$ has a maximum centered at $q \sim 1/a$ (Fig. 2.3a) and defines a range of momenta where the s-SNOM can probe the surface excitations of the system most effectively. In our experiments, this range of memonta is peaked at $q \sim 3.4\times10^5\,\mathrm{cm}^{-1} >> \sqrt{\varepsilon_0}\,\omega / c$ .The final result for the demodulated signal is (cf. Ref. 7)

$$s_n e^{i\phi_n} \propto \int_0^{2\pi} \frac{e^{in\phi} d\phi}{1 - G(b + \Delta z(1 - \cos\phi), \omega) a^3}. \tag{2.4}$$

As a first application of Eqs. 2.3 and 2.4, consider a bulk SiO_2 sample. The reflection coefficient is given by the Fresnel formulae:

$$r_P(q, \omega) = \frac{\varepsilon_1 k_0 - \varepsilon_0 k_1}{\varepsilon_1 k_0 + \varepsilon_0 k_1}, \tag{2.5}$$

where subscripts j = 0 and 1 refer to vacuum and SiO_2, respectively, ε_j are the dielectric functions (e.g., ε_0 = 1), and k_j are the *z*-components of the momenta:

$$k_j = \sqrt{\varepsilon_j \frac{\omega^2}{c^2} - q^2}, \quad \mathrm{Im} k_j \geq 0. \tag{2.6}$$

At $q >> \sqrt{\varepsilon_0}\omega/c$, the reflection coefficient r_p becomes q-independent. In previous literature[1,16,17] this q-independent value was denoted by $\beta(\omega)$:

$$r_P \approx \beta(\omega) \equiv \frac{\varepsilon_1 - \varepsilon_0}{\varepsilon_1 + \varepsilon_0} = 1 - \frac{\varepsilon_0}{\kappa(\omega)}, \tag{2.7}$$

$$\kappa(\omega) = \frac{\varepsilon_0 + \varepsilon_1}{2}. \tag{2.8}$$

The main spectroscopic feature of $|\beta(\omega)|$ is a maximum at the surface phonon frequency, which is approximately 1150 cm^{-1} in our sample. Function $|G|$ mirrors the behavior of $|\beta(\omega)|$ because for q-independent r_P, Eq. 2.3 yields $G(z_d, \omega)a^3 = \beta(\omega)a^3/4z_d^3$.

The 3rd harmonic component $s_3 e^{i\phi_3}$ of the s-SNOM signal, needed for comparison with the experiment, is obtained from G via the nonlinear operation of demodulation (Eq. 2.4). Using a = 30 nm and treating b as an adjustable parameter, we find good agreement between this simple model and the measurements for $b = 0.7a$ (Fig. 2.2). Note that demodulation causes a red shift of the s_3 to $\omega \approx 1128\ cm^{-1}$. Our results for SiO_2 are also in a good agreement with a recent s-SNOM study of SiO_2 (both crystalline and amorphous), in which the main maxima in s_n were found at 1120 – 1130 cm^{-1} (In crystalline SiO_2 additional weak maxima have also been reported.) [28].

2.7.3 Near-field response of the graphene-SiO_2 interface

We now apply point dipole model to the case where the surface of SiO_2 is

covered with graphene. Consider the in-plane momenta satisfy the strong inequality $\omega/c << q << \omega/v_F$. For q satisfying the above inequality, the expression for $r_P(q,\omega)$ can be brought to the form analogous to Eq. 2.7:

$$r_P(q,\omega) = 1 - \frac{\varepsilon_0}{\kappa(\omega)\varepsilon(q,\omega)}, \tag{2.9}$$

where the 2D dielectric function of graphene $\varepsilon(q,\omega)$ calculated with Random Phase Approximation (RPA) method is given as:

$$\varepsilon(q,\omega) = 1 - \frac{2e^2}{\kappa(\omega)}\frac{q}{\hbar\omega}\left[\frac{|\mu|}{\hbar\zeta} - \frac{1}{4}\ln\left(\frac{2|\mu| + \hbar\zeta}{2|\mu| - \hbar\zeta}\right)\right], \quad \zeta \equiv \omega + i\gamma. \tag{2.10}$$

μ is the chemical potential of graphene, and $\gamma > 0$ is the phenomenological scattering rate of quasiparticles [33,48,49]. In our calculations, we adopted $\gamma \sim 0.09\omega$ to mimic experimental optical conductivity of graphene in Ref. 20.

The *P*-polarized (i.e. TM) collective mode spectra of the graphene-SiO_2 interface can be extracted from Eq. 2.9 and 2.10 as follows. The first method is to look for poles of r_P. This leads us to the equation:

$$\varepsilon(q, \omega_P(q)) = 0, \tag{2.11}$$

which is a familiar result for the dispersion of a plasmon. Under the earlier assumption $\omega >> v_F q$, it has a solution of the form [6,33,48,50-52] $\omega_P(q) \approx v\sqrt{2\alpha(\omega_P)k_F q}$, where $\alpha(\omega) = e^2/\hbar v\kappa(\omega)$ is a dimensionless measure of the Coulomb interaction strength. For constant α, Eq. 2.11 gives the usual $\sqrt{q}$-dispersion of a 2D plasmon. A frequency-dependent dielectric function of the substrate causes α to become a

complex-valued function of ω. This introduces shift and broadening of the plasmon mode [13,14,53,54].

Equation 2.11 has another solution, which becomes more apparent if this equation is rewritten as:

$$\kappa(\omega) = \frac{2e^2 q}{\hbar\omega}\left[\frac{|\mu|}{\hbar\zeta} - \frac{1}{4}\ln\left(\frac{2|\mu| + \hbar\zeta}{2|\mu| - \hbar\zeta}\right)\right] \tag{2.12}$$

At $q = 0$ and $\omega \neq 0$, it gives $\kappa(\omega) = 0$, which corresponds to the pole of r_P in the absence of graphene, cf. Eq. 2.7. Therefore, this solution represents the surface phonon. By continuity, it gives rise to the entire branch of dispersion — surface phonon coupled with plasmon — at finite q. Therefore, our formalism captures both types of surface collective modes as well as their interaction.

Solving Eq. 2.12 is not the most practical way to extract the desired mode spectra. Instead, we follow another common procedure and obtain these spectra from the condition of maximum dissipation, which is realized at the maxima of $\mathrm{Im} r_P$. The spectra can be conveniently visualized by a pseudocolor plot of $\mathrm{Im} r_P$ as a function of q and ω. These plots for various choices of μ are presented in Fig. 2.3 where one can clearly see two sets of dispersion curves.. We remark that the blue shift of the 1150 cm^{-1} mode in Fig. 2.3c-d originated from the phonon-plasmon hybridization and can also be understood as the result of screening effects. At frequencies near the phonon resonance of SiO_2, Eq. 2.10 can be witten as $\varepsilon(q, \omega_P(q)) = 1 - \omega_p^2(q)/\omega^2$. Thus $\varepsilon(q, \omega_P(q))$ of graphene is

smaller than 1 close to SiO_2 phonon frequency, which hardens the frequency of the resonance in accord with the data.

Finally, after substituting Eq. 2.9 into Eqs. 2.3 and 2.4 and with doing numerical quadrature, we compute the near-field coupling G and the demodulated s-SNOM signal for the point-dipole model of the tip. We use the same parameters a and b as in the previous section. As shown in Fig. 2.2, the amplitude $s_3(\omega)$ has two resonances: the high-freqeuncy one corresponds to surface phonon resonance and the low-frequency one corresponds to the plasmon resonance. This latter mode is somewhat red-shifted compared to the intrinsic plasmon frequency estimated from dispersion diagram in Fig. 2.3b: about 800 cm^{-1} at the dominating momentum $q = 1/a$. Various factors can impact the frequencies of both resonances in the model spectra including: tip geometry, modulation amplitude, and others.

Now we discuss the lineshape characteristics of both resonances in the amplitude spectra in Fig. 2.2b. The low-frequency plasmon resonance shows up as a rather broad feature. The width of the high-frequency plasmon-phonon resonance is systematically enhanced by highly-doped graphene. To understand these special spectral features, it is imperative to consider the tip coupling weight function in Fig. 2.3a and dispersion diagrams in Fig. 2.3b-d. From Fig. 2.3a, one can see that the tip is coupled to a wide range of momenta centered at $q = 1/a$ with a full width at half maximum (FWHM) of about $\Delta q = 1.25/a$. Because of this rather broad spread of momenta, the actual width of the near-field

resonance $\Delta\omega$ is enhanced by a factor related to the group velocity of a given mode u_g = dω/dq. For weakly doped graphene (Fig. 2.3b), plasmon and phonon modes are separated. In this case the phonon mode is flat (u_g=0), so the observed phonon resonance (Fig. 2.2a) is quite narrow. In contrast, the plasmon mode is quite dispersive (u_g>0) in the region near q = 1/a, thus the predicted plasmon resonance is much wider than phonon resonance (Fig. 2.2b). At higher dopings (Fig. 2.3c,d), the plasmon and phonon become coupled. The new hybrid plasmon-phonon mode acquires dispersion (u_g>0), which increases the near-field resonance width. In the case of low-frequency resonance that is due to direct coupling to the plasmon, the issue of the resonance width is more complex. The increasing doping level can certainly increase the group velocity u_g of plasmon. However, as soon as the doping level becomes sufficiently high to promote plasmon-phonon coupling, the magnitude of u_g is suppressed. These two effects compete with each other. In addition, the resonance strength of a given mode and damping by free electrons excitation will also affect the lineshape of the near-field resonance.

2.8 Acknowledgements

This work is supported by ONR, DOE, AFOSR, NASA, MURI and Deutsche Forschungsgemeinschaft through the Cluster of Excellence Munich Centre for Advanced Photonics.

Chapter 2, in full, is a reprint of the material as it appears in Z. Fei, G. O. Andreev,

W. Bao, L. M. Zhang, A. S. McLeod, C. Wang, M. K. Stewart, Z. Zhao, G. Dominguez, M.Thiemens, M. M. Fogler, M. J. Tauber, A. H. Castro-Neto, C. N. Lau, F. Keilmann, and D. N. Basov, “Infrared Nanoscopy of Dirac Plasmons at the Graphene-SiO2 interface”, Nano Lett. 11(11), 4701-4705 (2011). The dissertation author was the primary investigator and author of this paper.

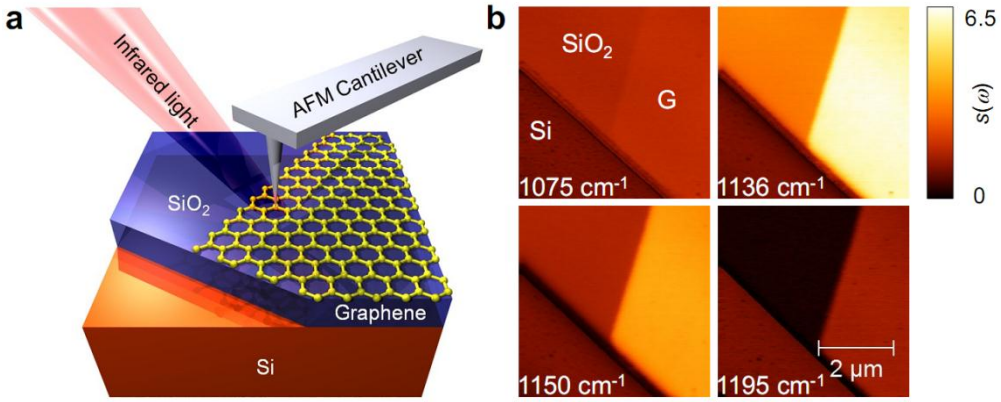

Figure 2.1: Schematics and imaging data of our near-field measurement. (a) Schematics of the near-field nanoscopy experiment used to study monolayer graphene on top of SiO_2/Si substrate. In the bottom left corner of the structure, SiO_2 has been etched away to enable tip contact with Si wafer. (b) Infrared near-field images displayed at four representative frequencies. The strong IR contrast between Si, SiO_2 and graphene (G) is clearly seen to vary systematically with the probing frequency. The plotted quantity $s(\omega)$ is the normalized backscattering amplitude defined in the text.

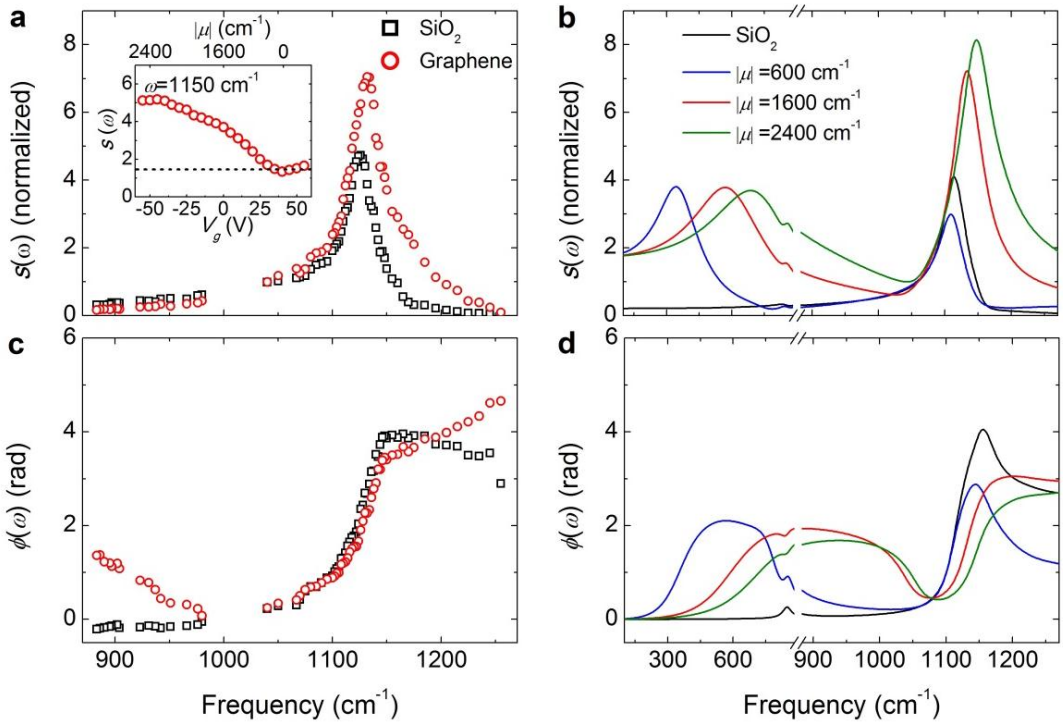

Figure 2.2: Spectra of the near-field amplitude $s(\omega)$ and phase $\phi(\omega)$. Panels (a),(c): experimental data extracted from images as in Fig. 2.1b for SiO_2 (black squares) and graphene on SiO_2 (red circles). The inset of Fig. 2.2a shows gating measurement results for the graphene near-field amplitude at $\omega = 1150$ cm^{-1}. The dotted line marks the value of gate-independent SiO_2 amplitude also probed at 1150 cm^{-1}. Top axis of the inset marks the calculated chemical potential of graphene. Panels (b),(d): dipole model spectra for SiO_2 (black) and graphene on SiO_2 (colors) for three different choices of the chemical potential $|\mu|$ = 600, 1600, and 2400 cm^{-1}; the predicted low-frequency resonance, the onset of which is seen in (c), reveals direct near-field coupling to the Dirac plasmon of graphene

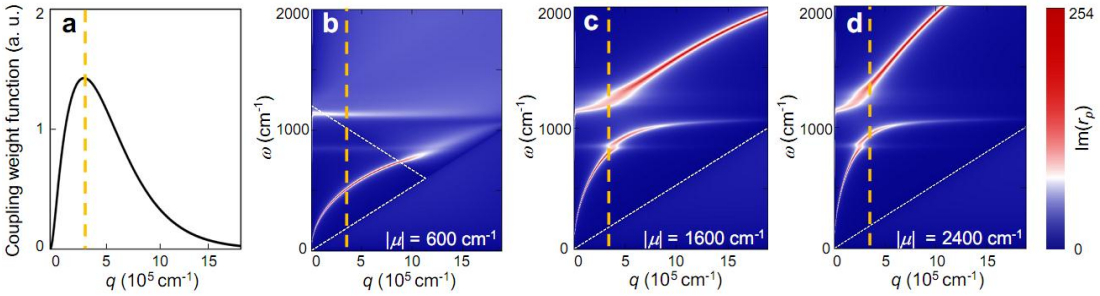

Figure 2.3: Dispersion diagrams of graphene plasmons and SiO_2 phonons. (a) The momentum dependence of time-averaged near-field coupling weight function $q^2 \exp(-2qz_d)$ which peaks at $q = 3.4 \times 10^5\ \text{cm}^{-1}$ for our tip radius $a = 30$ nm. (b)-(d) Imaginary part of the reflection coefficient $r_P(q, \omega)$ calculated using Eq. 2.1 with chemical potentials $|\mu| = 600$, 1600, and 2400 cm^{-1}, respectively and displayed in false color scale. Vertical yellow dashed lines in (a)-(d) mark the dominant q for maximum near-field coupling. White dotted lines in (b)-(d) mark the boundaries of single-particle intra- and inter-band excitation continua of graphene; these two boundaries meet at ($q = k_F$, $\omega = |\mu|/\hbar$).

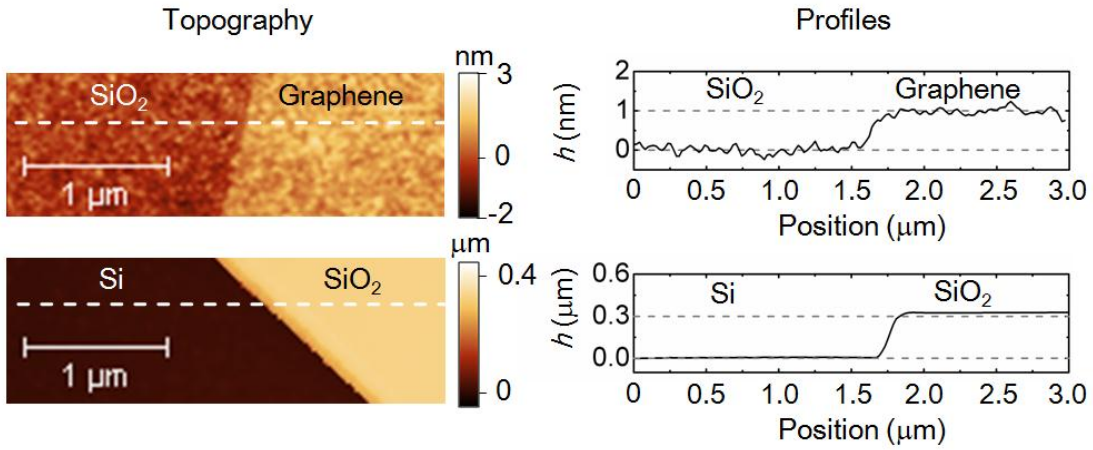

Figure 2.4: AFM topography and horizontal line profiles of graphene and SiO_2.

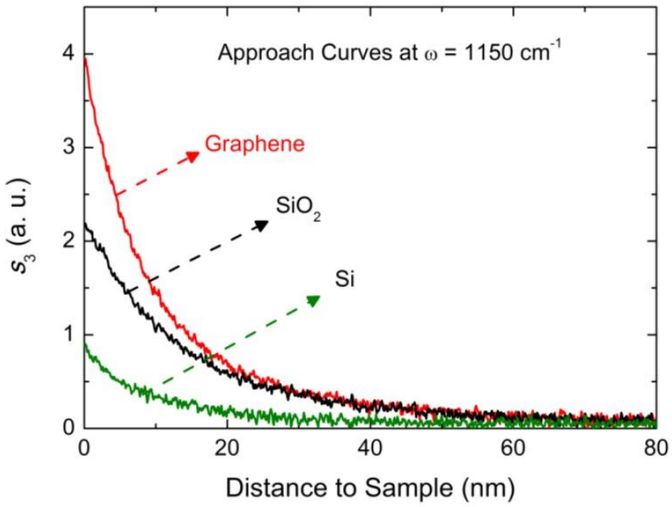

Figure 2.5: Near field approach curves of graphene, SiO_2 and silicon.

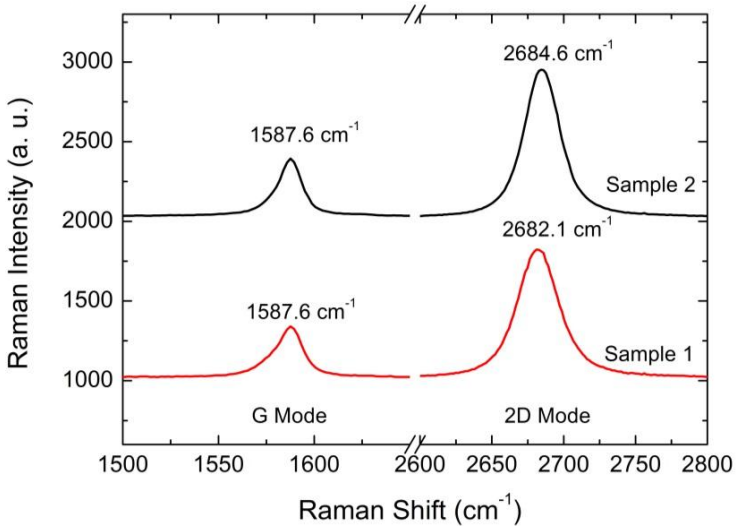

Figure 2.6: Raman spectroscopy data of our graphene samples.

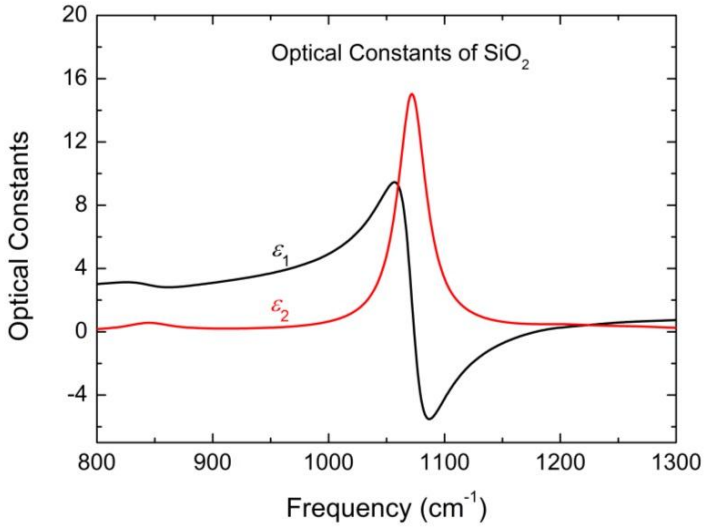

Figure 2.7: Real and imaginary part of SiO_2 permittivity from ellipsometry.

2.9 Bibliography

1. H. A. Atwater, Sci. Am. **296**, 56–63 (2008).

2. P. R. West, S. Lshii, G. V. Naik, N. K. Emani, V. M. Shalaev, and A. Boltasseva Laser & Photon. Rev. 1-13 (2010).

3. J. A. Schuller, E. S. Barnard, W. Cai, Y. C. Jun, J. S. White, and M. L. Brongersma, Nature Mater. **9**, 193-204 (2010).

4. M. I. Stockman, Phys. Today **64**, 39-44 (2011).

5. C. Jones, R. L. Olmon, S. E. Skrabalak, B. J. Wiley, Y. N. Xia, and M. B. Raschke, Nano Lett. **9**, 2553-2558 (2009).

6. K. W. -K. Shung, Phys. Rev. B **34**, 979-993 (1986).

7. R. J. Koch, T. Seyller, and J. A. Schaefer, Phys. Rev. B **82**, 201413 (2010).

8. F. H. L. Koppens, D. E. Chang, and F. J. Garcia de Abajo, Nano Lett. **11**(8), 3370-3377 (2011).

9. M. Jablan, H. Buljan, and M. Soljacic, Phys. Rev. B **80**, 245435 (2009).

10. F. Bonaccorso, Z. Sun, T. Hasan, and A. C. Ferrari, Nature Photon. **4**, 611-622 (2011).

11. Vakil and N. Engheta, Science **332**, 1291-1294 (2011).

12. Y. Nikitin, F. Guinea, F. J. Garcia-Vidal, and L. Martin-Moreno, Phys. Rev. B **84**, 195446 (2011).

13. Y. Liu, R. F. Willis, K. V. Emtsev, and T. Seyller, Phys. Rev. B **78**, 201403(R) (2008).

14. Y. Liu and R. F. Willis, Phys. Rev. B **81**, 081406(R) (2010).

15. R. J. Koch, T. Seyller, and J. A. Schaefer, Phys. Rev. B **82**, 201413 (2010).

16. D. N. Basov, R. D. Averitt, and D. van der Marel, and M. Dressel, Rev. Mod. Phys. **83**(2) 471-541 (2011).

17. R. Hillenbrand, R. Taubner, and F. Keilmann, Nature **418**, 159-162 (2002).

18. Huber, N. Ocelic, and D. Kazantsev, and R. Hillenbrand, App. Phys. Lett. **87**, 091103 (2005).

19. F. Wang, Y. Zhang, C. Tian, C. Girit, A. Zettl, M. Crommie, and Y. R. Shen, Science **320**, 206-209 (2008).

20. Z. Q. Li, E. A. Henriksen, Z. Jiang, Z. Hao, and M. C. Martin, P. Kim, H. L. Stormer, and D. N. Basov, Nature Phys. **4**, 532-535 (2008).

21. D. N. Basov, R. D. Averitt, D. van der Marel, M. Dressel, and K. Haule, Rev. Mod. Phys. **83**, 471-541 (2011).

22. L. Novotny, and B. Hecht, Principles of nano-optics. Cambridge University Press (2006).

23. N. Ocelic, A. Huber, and R. Hillenbrand, Appl. Phys. Lett. **89**, 101124 (2006).

24. S. Berciaud, S. Ryu, L. E. Brus, and T. F. Heinz, Nano Lett. **9**, 346-352 (2009).

25. F. Schedin, A. K. Geim, S. V. Morozov, E. W. Hill, P. Blake, M. I. Katsnelson, and K. S. Novoselov, Nature Mater. **6**, 652-655 (2007).

26. S. Pisana, M. Lazzeri, C. Casirachi, K. S. Novoselov, A. K. Geim, A. C. Ferrari, F. Mauri, Nature Mater. **6**, 198-201 (2007).

27. J. Aizpurua, T. Taubner, F. J. G. Abajo, M. Brehm, and R. Hillenbrand, Opt. Express **16**, 1529-1545 (2008).

28. S. Amarie and F. Keilmann, Phys. Rev. B **83**, 045404 (2011).

29. R. Hillenbrand and F. Keilmann, Phys. Rev. Lett. **85**, 3029-3032 (2000).

30. T. Taubner, F. Keilmann, and R. Hillenbrand, Nano Lett. **4**, 1669-1672 (2004).

31. Cvitkovic, N. Ocelic, and R. Hillenbrand, Opt. Express **15**, 8550-8565 (2007).

32. J. A. Porto, P. Johansson, S. P. Apell, and T. López-Ros, Phys. Rev. B **67**, 085409 (2003).

33. Wunsch, T. Stauber, F. Sols, and F. Guinea, New J. Phys. **8**, 318 (2006).

34. T. Stauber, N. M. R. Peres, and A. H. Castro Neto, Phys. Rev. B **78**, 085418 (2008).

35. M. Y. Han, B. Ozyilmaz, Y. Zhang, and P. Kim, Phys. Rev. Lett. **98**, 206805 (2007).

36. X. Li, X. Wang, L. Zhang, S. Lee, and H. Dai, Science **319**, 1229-1231 (2008).

37. F. Xia, T. Mueller, Y. -M. Lin, A. V. Garcia, and P. Avouris, Nature Nano. **4**, 839-843 (2009).

38. R. Hillenbrand, F. Keilmann, P. Hanarp, D. S. Sutherland, J. Aizpurua, Appl. Phys. Lett. **83**, 368-370 (2003).

39. L. Ju, B. Geng, J. Horng, C. Girit, M. Martin, Z. Hao, H. A. Bechtel, X. Liang, A. Zettl, Y. R. Shen, and F. Wang, Nature Nano. **6**, 630-634 (2011).

40. C. Ferrari, J. C. Meyer, V. Scardaci, C. Casiraghi, M. Lazzeri, F. Mauri, S. Piscanec, D. Jiang, K. S. Novoselov, S. Roth, A. K. Geim, Phys. Rev, Lett. **97**, 187401 (2006).

41. Graf, F. Molitor, K. Ensslin, C. Stampfer, A. Jungen, C. Hierold, and L. Wirtz, Nano Lett. **7**(2), 238-242 (2007).

42. R. Esteban, R. Vogelgesang, and K. Kern, Opt. Express **17**, 2518-2529 (2009).

43. J. Renger, S. Grafström, L. M. Eng, and R. Hillenbrand, Phys. Rev. B **71**, 075410 (2005).

44. P. K. Aravind and H. J. Metiu, Phys. Chem. **86**, 5076-5084 (1982).

45. P. K. Aravind and H, Metiu, Surf. Sci. **124**, 506-528 (1983).

46. R. W. Rendell and D. J. Scalapino, Phys. Rev. B **24**, 3276-3294 (1981).

47. S. V. Sukhov, Ultramicroscopy **101**, 111-122 (2004).

48. H. Hwang and S. Das Sarma, Phys. Rev. B **75**, 205418 (2007).

49. H. Castro Neto, F. Guinea, N. M. R. Peres, K. S. Novoselov, and A. K. Geim, Rev. Mod. Phys. **81**, 109-162 (2009).

50. O. Vafek, Phys. Rev. Lett. **97**, 266406 (2006).

51. S. Gangadharaiah, A. M. Farid, and E. G. Mishchenko, Phys. Rev. Lett. **100**,166802 (2008).

52. Hill, S. A. Mikhailov, and K. Ziegler, Euro. Phys. Lett. **87**, 27005 (2009).

53. H. Hwang, R. Sensarma, and S. Das Sarma, Phys. Rev. B **82**, 195406 (2010).

54. S. A. Mikhailov and K. Ziegler, Phys. Rev. Lett. **99**, 016803 (2007).

Chapter 3

Gate-tuning of graphene plasmons revealed by infrared nano-imaging

3.1 Introduction

Surface plasmons are collective oscillations of electrons in metals or semiconductors enabling confinement and control of electromagnetic energy at subwavelength scales [1-5]. Rapid progress in plasmonics has largely relied on advances in device nano-fabrication [5-7], whereas less attention has been paid to the tunable properties of plasmonic media. One such medium—graphene—is amenable to convenient tuning of its electronic and optical properties with gate voltage [8-11]. Through infrared nano-imaging we explicitly show that common graphene/SiO_2/Si back-gated structures support propagating surface plasmons. The wavelength of graphene plasmons is of the order of 200 nm at technologically relevant infrared frequencies, and they can propagate several times this distance. We have succeeded in altering both the amplitude and wavelength of these plasmons by gate voltage. We investigated losses in graphene using

plasmon interferometry: by exploring real space profiles of plasmon standing waves formed between the tip of our nano-probe and edges of the samples. Plasmon dissipation quantified through this analysis is linked to the exotic electrodynamics of graphene [10]. Standard plasmonic figures of merits of our tunable graphene devices surpass that of common metal-based structures.

3.2 Experimental details

In general, surface plasmons can exist in any material with mobile charge carriers whose response to electric field remains reactive, i.e., whose in-plane momentum- and frequency-dependent complex conductivity, $\sigma(q,\omega)=\sigma_1+i\sigma_2$, is predominantly imaginary. Of particular interest are plasmons with high momenta $q_p >> \omega/c$, which may be utilized for extreme concentration of electromagnetic energy [1-5]. In conventional bulk metals, the frequencies of such high-q plasmons reside in the visible or ultraviolet ranges. In graphene, they are expected to appear in the terahertz and infrared (IR) domains [12]. However, these high-q IR plasmons are dormant in conventional spectroscopy of graphene. Here we utilized the scattering-type scanning near-field optical microscope (s-SNOM) to experimentally access high-q plasmons by illuminating the sharp tip of an atomic force microscope (AFM) with a focused IR beam (Fig. 3.1a). The momenta imparted by the tip extend up to a few times $1/a$, where $a \approx 25$ nm is the curvature radius of the tip [13], thus spanning the typical range of IR plasmon momenta q_p in graphene [12]. The spatial resolution of s-SNOM is also set by a, and proves to be an order of magnitude smaller than the plasmon wavelength λ_p. The direct observable of our

method—the scattering amplitude $s(\omega)$—is a measure of the electric field strength inside the tip-sample nanogap. Consequently, the s-SNOM technique enables spectroscopy [13] and IR nano-imaging of graphene plasmons without the need to fabricate specialized periodic structures [14]. Our imaging data elucidate real-space characteristics of IR plasmons in graphene such as reflection, interference and damping. All these phenomena can be readily manipulated with gate voltage – a noteworthy property unattainable in metal-based plasmonics.

3.3 Experimental data

To probe directly the properties of graphene plasmons, we utilize a frequency ω = 892 cm^{-1} corresponding to the wavelength λ_{IR} = 11.2 μm in the IR regime where the plasmon is unimpeded by the surface optical phonon supported in graphene/SiO_2/Si structures [13]. The nano-imaging results are shown in Figs. 3.1b-e, where we plot normalized near-field amplitude $s(\omega) = s_3(\omega) / s_3^{Si}(\omega)$. Here, $s_3(\omega)$ and $s_3^{Si}(\omega)$ are the 3rd order demodulated harmonics of the near-field amplitude measured for the given sample and for a Si reference sample, respectively. The near-field amplitude $s(\omega)$ tracks real-space variations in the local electric field underneath the tip, enabling exploration of surface phonon polaritons and surface plasmons [17,18].

In Fig. 3.1b, we present a $s(\omega)$ image acquired at the graphene-SiO_2 interface revealing periodic oscillations of the $s(\omega)$ signal extending along the graphene edge. Point and circular defects (Fig. 3.1d) trigger circular fringe patterns. Line defects (Fig. 3.1b) produce elongated, elliptical patterns. We observed fringes at both sides of the

single/bilayer graphene boundary (Fig. 3.1c). Finally, strongly tapered corners of graphene (Fig. 3.1e) reveal the two groups of fringes oriented along both edges of graphene in the field of view. In all cases, the periodicity of the fringe patterns is around 100 nm.

3.4 Theory and Analysis

Images in Fig. 3.1 are consistent with the following scenario. Illuminated by focused IR light, the AFM tip launches plasmon waves of wavelength λ_p propagating radially outward from the tip. Sample edges or defects act as (imperfect) reflectors of the plasmon waves, directing them back to the tip. Therefore complex patterns of interference between launched and reflected plasmons should form inside graphene. We emphasize that our experimental technique does not capture instantaneous snapshots of these complex patterns. Instead, while the tip "launches" plasmon waves propagating in all directions, it only "detects" the cumulative near-field plasmonic signal arising underneath it. This stands in rough analogy with the operating principle of sonar echolocation. In Fig. 3.2a, we sketch the plasmon interference pattern in the form of plasmon amplitude revealing standing wave oscillations between the tip and sample edge. As the tip is scanned towards the edge, it registers these oscillations with periodicity given by $\lambda_p/2$ as shown in bottom panels of Fig. 3.2a. Our plasmon interference interpretation is supported by theoretical estimates of the wavelength λ_p. The plasmon dispersion of a two-dimensional (2D) metal residing at the interface of vacuum (dielectric constant $\varepsilon_0 = 1$) and a substrate with dielectric function $\varepsilon_{sub}(\omega)$ is given by the formula:

$$q_p = \frac{i\omega\kappa}{2\pi\sigma},\ \ \kappa(\omega) = \kappa_1 + i\kappa_2 \equiv \frac{\varepsilon_0 + \varepsilon_{\text{sub}}(\omega)}{2}. \tag{3.1}$$

Assuming that the conductivity σ of graphene takes a Drude form with relaxation time τ, one can rewrite Eq. 3.1 as:

$$q_p = \frac{\hbar^2\kappa(\omega)}{2e^2E_F}\omega(\omega + \frac{i}{\tau}) \tag{3.2}$$

Derivation of these equations and further refinements are discussed in the Supplementary Information. The real part of $q_p = q_1 + iq_2$ determines the plasmon wavelength $\lambda_p = 2\pi/q_1$ and the ratio between imaginary part and real part defines the plasmon damping rate $\gamma_p = q_2/q_1$. In graphene, the Dirac-like dispersion of the Fermi energy $E_F = \hbar v_F k_F$ with Fermi momentum $k_F = \sqrt{\pi |n|}$ [8], implies $|n|^{-1/2}$ scaling of the plasmon momentum with the carrier density n at fixed ω. Here $v_F \approx c/300 = 10^6$ m/s is the Fermi velocity. Finally, using frequency ω = 892 cm^{-1} and $n \approx 8\times10^{12}$ cm^{-2} determined from the micro-Raman probe (see below) at the graphene edge, we find $\lambda_p \approx 200$ nm from Eq. 3.2, which is roughly twice the distance between fringes in Figs. 3.1b-e.

The images in Figs. 3.1b-e contain rich insights on processes governing plasmon propagation and losses on the surface of graphene. It is therefore instructive to examine line profiles along the direction normal to the sample edges. In Fig. 3.2b we show a plot obtained by averaging 150 such profiles—a procedure used to improve the signal-to-noise ratio. We find that the fringe widths increase from the interior to the edge of graphene, implying the plasmon wavelength λ_p likewise increases. This behavior is due to enhancement of the carrier density n near the sample edge, which is verified by

our micro-Raman experiments (inset of Fig. 3.2b) [20,21]. Thus, plasmonic interference patterns reported in Fig. 3.2b uncover a utility of IR imaging for the nanoscale determination of local carrier density in graphene. In Fig. 3.2b we also show modeling results of plasmon profiles following a procedure detailed in the Supplementary Information. Our modeling provides a quantitative account of plasmon interferometry data. The carrier density profile (red curve in the inset of Fig. 3.2b) and the damping rate γ_p constitute the adjustable parameters of the model. Since plasmons in our experiments are launched and detected by the same point source (AFM tip), the interference amplitude necessarily exhibits decay from the sample edge even when the damping rate is assumed to be vanishingly small (blue trace in Fig. 3.2b). The best fit to the amplitude profile is achieved for significantly stronger damping with $\gamma_p = 0.135$.

According to Eqs. 3.1 and 3.2, the plasmon wavelength λ_p is directly determined by the carrier density *n*. We experimentally demonstrate this unique aspect of graphene plasmonics through imaging under gate bias, displayed in Fig. 3.3a. Over a range of V_g values from +30 V to -20 V, the hole density *n* in our samples increases monotonically, a consequence of significant unintentional hole doping present even in ungated graphene/SiO_2/Si structures (inset of Fig. 3.2b). This tuning of carrier density produces systematic variations in the plasmonic profiles: fringe amplitude and periodicity are both enhanced with increasing *n*. By inferring λ_p directly from the fringe width, we observe a systematic decrease in λ_p with the reduction in hole density. Our gate-dependent data for λ_p approximately follow the $\lambda_p \propto |n|^{1/2}$ law predicted for monolayer graphene [22]. In contrast, the plasmon damping rate does not show clear gate dependence and is roughly

equal to 0.135 ± 0.015 at all V_g. This magnitude of γ_p significantly exceeds theoretical estimates for graphene with similar electronic mobility $\mu \approx 8000\ \mathrm{cm}^2/\mathrm{V}\cdot\mathrm{s}$ [12].

3.5 Discussion

It is important to understand why plasmon damping in our structures is abnormally strong. According to Eqs. 3.1 and 3.2 two additive contributions define damping rate as $\gamma_p \approx (\sigma_1/\sigma_2) + (\kappa_2/\kappa_1)$. The first term is associated with plasmonic losses implicit to graphene, whereas the second term describes losses due to the SiO_2 substrate. At ω = 892 cm^{-1}, we estimate κ = 2.52 + 0.13i and hence, $\kappa_2/\kappa_1 \approx 0.05$, based on our ellipsometric measurements of SiO_2/Si wafers. The resulting value of $\sigma_1/\sigma_2 \approx 0.08$ is unexpectedly high, three to four times higher than the estimate of σ_1/σ_2 = $(\omega\tau)^{-1}$ one obtains from Eq. 3.2 using the relaxation rate $\tau^{-1} \sim 20\ \mathrm{cm}^{-1}$, corresponding to a typical DC mobility of our samples. This discrepancy affords two possible interpretations. Excessive losses may originate from an enhanced electronic relaxation rate at infrared frequencies compared to that established in DC transport. Alternatively, losses may be unrelated to free carrier mobility/dynamics and may instead be associated with extrinsic factors such as surface irregularities. Our plasmonic interferometry data in Figs. 3.2 and 3.3 provide strong support for the former hypothesis. Indeed, these images yield γ_p and λ_p (Fig. 3.3b) and thus allow us to determine the complex optical conductivity of graphene (inset of Fig. 3.3b) based on the formulae: $\sigma_2 \approx \frac{\omega\kappa}{4\pi^2}\lambda_p$; $\sigma_1 = \sigma_2(\gamma_p - \kappa_2/\kappa_1)$. We remark that these relations between plasmonic

parameters (λ_p, γ_p) and the complex optical conductivity σ of graphene hold true for any plasmonic material for which $\sigma_1 << \sigma_2$. Therefore these expressions apply even if the frequency-dependent conductivity deviates from the simple Drude model. The appeal of this analysis lies in establishing a link between real-space plasmonic profiles and the optical constants inferred from conventional IR spectroscopy. Our imaging data reveal that the real part of the conductivity of graphene is as high as $\sigma_1 \approx 0.5e^2/h$. This value greatly exceeds the theoretical estimate of $\sigma_1(\omega = 892\ \text{cm}^{-1}, n = 8 \times 10^{12}\ \text{cm}^{-2}, \tau^{-1} = 20\ \text{cm}^{-1}) = 0.13e^2/h$ obtained from a model of non-interacting Dirac quasiparticles weakly scattered by disorder [23-25], but is comparable to IR spectroscopy results for back-gated graphene on SiO_2/Si [10]. In an ideal, non-interacting graphene $\sigma_1(\omega < 2E_F)$ is vanishingly small due to the phenomenon of "Pauli blocking" [10]. Thus the source of strong plasmonic losses in our back-gated samples is traced to the unexpectedly large magnitude of σ_1. This result supports the notion of prominent many-body effects in graphene beyond the picture of non-interacting Dirac fermions [27-29]. Further experiments on suspended graphene as well as devices employing various types of dielectric substrates such as BN are needed to disentangle the roles of electron-electron and graphene-substrate interactions in the dissipation we observe at infrared frequencies. Our work uncovers an experimental path and analysis methodology for these future studies of many-body interactions in graphene.

3.6 Conclusion and Outlook

Infrared nano-imaging experiments reported here established graphene/SiO_2/Si

structures as a potent plasmonic medium that enables voltage control of both the plasmon wavelength and amplitude. Higher gate voltages than used in our study will allow for the binary on/off switching of plasmon propagation with a possibility of potentially local control by a top gate or a biased tip. The plasmon wavelength in graphene $\lambda_p \approx 200$ nm is one of the shortest imaged for any material whereas the propagation length is on par with Au in experiments monitoring strongly confined plasmons launched by AFM tips [18]. An important figure of merit λ_{IR}/λ_p = 50-60 for our back-gated devices surpasses that of conventional Ag-based structures [12]. Intrinsic plasmonic losses in graphene that we analyzed in detail can be substantially reduced or even eliminated through population inversion [30]. We stress that plasmon tuning is realized here in the architecture of a Metal(graphene)-Oxide-Semiconductor(Si) device: a ubiquitous system in modern information processing. Furthermore, the performance of even the first generation of plasmonic devices reported here and in Ref. 15 is rather promising against non-tunable metal-based structures [12]. For all these reasons we believe that graphene may be an ideal medium for active infrared plasmonics.

3.7 Methods summary

Infrared nano-imaging using s-SNOM: Our s-SNOM apparatus (Neaspec) is based on an atomic force microscope (AFM) operating in tapping-mode. Measurements were performed at an AFM tapping frequency of Ω = 270 kHz and tapping amplitude of 40 nm. The shaft of the conducting AFM tip acts as an antenna that boosts the efficiency of near-field interaction [26]. The back-scattered signal registered by the detector is

strongly dependent on the tip-sample distance. This enables isolation of the genuine near-field contribution from the overall back-scattered signal, which is periodically modulated at harmonics of the tapping frequency Ω. The m^{th} harmonic component of this signal $s_m e^{i\phi_m}$, termed the m^{th} demodulated signal (here m = 3), represents the desired near-field contribution.

Samples and devices: Our graphene samples were obtained by mechanical cleavage of bulk graphite and then transferred to SiO_2/Si substrate. To avoid surface contamination by lithographic procedures, bulk graphite connected to our graphene sample was utilized as an electrode in our back-gating experiments. To verify the gating functionality of our devices, we first performed a spectroscopic study of the hybrid plasmon-phonon resonance at various gate voltages and found good agreement with the published data [13]. Transport measurements of graphene samples fabricated following identical procedures indicate that the typical mobility of our graphene samples is about 8000 cm^2/Vs. Plasmon imaging experiments were completed for more than 30 graphene samples. All these structures exhibited highly reproducible behavior and consistent values for the plasmon wavelength and damping. The data displayed in Figs. 3.1-3.3 were obtained for devices with some of the weakest damping revealing the largest number of plasmonic oscillations. Nevertheless, even in these devices the plasmonic losses are stronger than expectations based on typical electronic mobility measurements.

Micro-Raman measurements: According to previous studies, the G-peak position of the graphene Raman signal is directly linked to its carrier density [20-22]. Therefore, the G-peak profile shown in the inset of Fig. 3.2b reflects the range of the variation in graphene carrier density close to the edge [21-22]. Our micro-Raman experiments were

carried out using a Renishaw inVia Raman microscope equipped with a $50\times$, NA = 0.75 long-distance objective, a 1800 l/mm grating and an XY stage with the resolution of 100 nm. The spot size in these experiments is limited by diffraction. Therefore, the fragment of the line profile of the G-peak frequency shown in the inset of Fig. 3.2b is instrumentally broadened.

3.8 Supplementary information

3.8.1 Origin of the observed spatial modulations

The qualitative explanation of the observed interference patterns is as follows. The tip of the near-field nanoscope excites a circular surface plasmon. A complex pattern of interference between the launched plasmon and its reflection off the sample edges is formed, as sketched in Fig. 3.1. The signal $s(x, y)$ detected by the nanoscope is proportional to the plasmonic amplitude directly underneath the tip, i.e., at the same in-plane point (x, y).

For simplicity, let us treat graphene as a half-infinite homogeneous medium. Denote by $A(r)$ be the complex amplitude of a circular wave at a distance r from its origin that would be excited in an infinite sample. Function $A(r)$ oscillates with plasmon momentum q_1 and decays as $e^{-q_2 r}$ due to damping. According to the method of images, for our half-infinite sample (with the edge at $x = 0$) the near-field amplitude registered by the tip is given by

$$s(x, y) \propto | A(0) + e^{i\theta} A(2x) | \tag{3.3}$$

Here the term $A(0)$ is due to the tip-launched wave, the term $e^{i\theta}A(2x)$ is due to its image, i.e., the reflected wave, and θ is the phase shift upon reflection (a number close to π). The

interference underneath the tip is constructive at

$$x_j = \frac{\lambda_p}{2}\left(j - \frac{\theta}{2\pi} \right) \tag{3.4}$$

This condition implies that the interference fringes are straight lines parallel to the edge. The distance between adjacent fringes is one half of the plasmon wavelength $\lambda_p \equiv 2\pi / q_1$. The first fringe at $x = x_1$ is expected to be the strongest. The amplitude of the subsequent fringes should monotonically decrease because the total amount of damping grows with the roundtrip distance $2x_j$.

The described physical picture is sufficient for a qualitative explanation of our experiments. In the remaining sections we develop it into a quantitative model by properly taking into account response functions of graphene and its SiO_2 substrate, as well as the interaction between the tip and the sample.

3.8.2 Optical conductivity of graphene

Within the linear-response theory, in-plane electric field $\tilde{\mathbf{E}}_{\|}$ and current density $\tilde{\mathbf{j}}$ in graphene are related by the momentum and frequency dependent conductivity $\sigma(q, \omega)$:

$$\tilde{\mathbf{j}}(q,) = \sigma(q,\omega)\tilde{\mathbf{E}}_{\|}(q,\omega). \tag{3.5}$$

(Here and below the tilde marks the Fourier transforms.) In this section we summarize the main properties of function $\sigma(q, \omega)$ and clarify assertions made about it in the main text.

The conductivity of the two-dimensional (2D) electron gas in graphene is related to its polarization function $P(q, \omega)$ by $\sigma(q,\omega) = ie^2(\omega / q^2)P(q,\omega)$. The formula for $P(q, \omega)$ has been derived within the random-phase approximation for zero temperature and no

disorder [22,31]. We assume that the latter can be introduced by replacing ω with $\varsigma = \omega + i\tau^{-1}$, where τ is the phenomenological relaxation time. In this way, we arrive at

$$\sigma(q,\omega) = \sigma_0(q,\omega)\left[1 + \Re(\frac{\hbar\varsigma + 2E_F}{\hbar v q}) - \Re(\frac{\hbar\varsigma - 2E_F}{\hbar v q})\right] - \frac{2i}{\pi}\frac{e^2\omega E_F}{(\hbar v q)^2}, \tag{3.6}$$

where

$$\sigma_0(q,\omega) = -i\frac{e^2}{4\hbar}\frac{\varsigma}{\sqrt{v^2q^2 - \varsigma^2}} \tag{3.7}$$

is the conductivity of undoped graphene and function $\Re(\alpha)$ is defined by

$$\Re(\alpha) = -\frac{1}{\pi}\left(\alpha\sqrt{1-\alpha^2} - \arccos\alpha\right). \tag{3.8}$$

In our model and simulations we neglect the momentum dependence of $\sigma(q, \omega)$. This is justified in the $q << \omega/v$ limit, where Eq. 3.6 simplifies to [31]

$$\sigma(q,\omega) = \frac{i}{\pi}\frac{e^2}{\hbar}\left[\frac{1}{\bar{\varsigma}} - \frac{1}{4}\ln\left(\frac{2+\bar{\varsigma}}{2-\bar{\varsigma}}\right)\right],\ \bar{\varsigma} = \frac{\hbar\varsigma}{E_F} \tag{3.9}$$

The disappearance of the q-dependence means that quasiparticles perceive the perturbing electric field as locally uniform. This is because the quasiparticle displacement $2\pi v/\omega$ over the time period of the field is much smaller than its wavelength $2\pi/q$.

If, in addition to $q << \omega/v$, the condition $\hbar\omega << E_F$ is also met, so that $\bar{\varsigma} << 1$, Eq. 3.9 reduced to the Drude-like formula

$$\sigma(\omega) = \frac{e^2}{\pi\hbar^2}\frac{E_F\tau}{1 - i\omega\tau}, \tag{3.10}$$

which was used in Eq. 3.2.

3.8.3 Local approximation for graphene response

The characteristic in-plane momenta q relevant in our experiments are of order of the plasmon momentum

$$q_p = i\kappa\omega/(2\pi\sigma) \tag{3.11}$$

[same as q_p in Eq. 3.1]. It can be verified that such momenta satisfy the conditions $q << k_F$, ω/v_F. As explained in Sec. II above, in this case the q-dependence of the conductivity can be neglected. Eq. 3.5 can therefore be replaced by the simplified local relation

$$\mathbf{j}(\mathbf{r}) = \sigma(\mathbf{r})\mathbf{E}_{\|}(\mathbf{r}),\ \mathbf{E}_{\|}(\mathbf{r}) = -\nabla\Phi(\mathbf{r}),\ \nabla \equiv (\partial/\partial x, \partial/\partial y), \tag{3.12}$$

which is valid even for systems without translational invariance. Below we use this relation to derive a closed system of equations that describe the response of graphene to an arbitrary external potential $\Phi_{ext}(\mathbf{r})$.

Within the quasi-static approximation, valid if all distances of interest are much shorter than the optical wavelength $2\pi c/\omega$, the total in-plane potential $\Phi(\mathbf{r})$ is given by

$$\Phi(\mathbf{r}) = \Phi_{ext}(\mathbf{r}) + V(\mathbf{r},0) * \delta\rho(\mathbf{r}),\ V(r,z) = \frac{1}{\kappa}\frac{1}{\sqrt{|r|^2 + z^2}}, \tag{3.13}$$

where κ is defined in Eq. 3.1, the star denotes convolution,

$$(A * B)(\mathbf{r}) = \int d^2\mathbf{r}' A(\mathbf{r}-\mathbf{r}')B(\mathbf{r}), \tag{3.14}$$

And $\delta\rho(\mathbf{r})$ is the charge density induced in graphene. Combining Eqs. 3.12 and 3.13, and the continuity relation, $-i\omega\rho(\mathbf{r}) + \nabla\mathbf{j} = 0$, we get the single equation for $\Phi(\mathbf{r})$:

$$\Phi(\mathbf{r}) + \frac{\kappa}{2\pi} V(r,0) * (\nabla q_p^{-1}(\mathbf{r})\nabla\Phi) = \Phi_{ext}(\mathbf{r}). \tag{3.15}$$

In general, it has to be solved numerically. The analytical solution can be obtained for an

infinite system of constant σ using the Fourier transform method, which yields

$$\tilde{\Phi}(\mathbf{q}) = \frac{q_p}{q_p - |\mathbf{q}|}\Phi_{ext}(\tilde{q}). \tag{3.16}$$

The plasmon momentum q_p correspond to the poles of $\tilde{\Phi}(\mathbf{q})$ in the complex q plane.

Consider, in particular, the external potential

$$\Phi_d(\mathbf{r}) = \frac{1}{\kappa}\frac{z_d}{(|\mathbf{r}-\mathbf{r}_d|^2 + z_d^2)^{3/2}},\ \tilde{\Phi}_d(\mathbf{q}) = \frac{2\pi}{\kappa}e^{-i\mathbf{q}\mathbf{r}_d - |\mathbf{q}|z_d} \tag{3.17}$$

created by a unit dipole located at ($\mathbf{r}_d$, z_d). Later we will need an expression for the electric field $\mathbf{E}_g = (\mathbf{E}_{g,\|}, E_{g,z})$ induced by electrons in graphene at an arbitrary point in space (rc, zc) in response to this dipole:

$$E_{g,\|}(r_c, z_c) = -\nabla_{r_c}(V(r, z_c) * \delta\rho)(r_c), \quad E_{g,z}(r_c, z_c) = -\frac{\partial}{\partial z_c}(V(r, z_c) * \delta\rho)(r_c) \tag{3.18}$$

Using Eqs. 3.16, 3.17, and 3.18, we find

$$E_{g,z}(r_d, z_d) = -\frac{1}{\kappa}\int_0^\infty \frac{q^3 dq}{q_p - q}e^{-2qz_d}, \tag{3.19}$$

as in our previous work [13]. The induced electric field has another contribution **E** from charges on the surface of the substrate. Using the method of images, we get

$$\mathbf{E}_s(\mathbf{r}_c, z_c) = \beta\frac{3(\hat{\mathbf{z}}\mathbf{R})\mathbf{R} - \hat{\mathbf{z}}R^2}{R^5},\ \beta = 1 - \frac{1}{\kappa},\ \mathbf{R} = (\mathbf{r}_c - \mathbf{r_d}, z_c + z_d). \tag{3.20}$$

Consider next a situation where graphene occupies $x \geq 0$ half-plane, which is relevant for s-SNOM imaging near the graphene edge. Eq. 3.15 is still valid if we define $\sigma(x < 0) \equiv 0$ and also add a boundary condition $\partial\Phi / \partial x = 0$ so that $j_x = 0$ at $x = 0$ to avoid infinite charge accumulation at the edge. Let us assume that $\sigma = \sigma(x)$ is invariant along y but may be a function of x. Without loss of generality, we can choose the dipole

y-coordinate to be zero, $y_d = 0$. Taking the one-dimensional Fourier transform in *y* of both sides of Eq. 3.15, we obtain

$$\tilde{\Phi}(x) - \frac{2}{\kappa} K_0(x \mid q_y \mid) * \delta\tilde{\rho}(x, q_y) = \tilde{\Phi}_d(x, q_y) = \frac{2}{\kappa} \frac{z_d}{r} \mid q_y \mid K_1(r \mid q_y \mid), \qquad (3.21)$$

$$\delta\tilde{\rho}(x, q_y) = -\frac{\kappa}{2\pi} \left[\frac{d}{dx} \frac{1}{q_p(x)} \frac{d}{dx} - \frac{q_y^2}{q_p(x)} \right] \tilde{\Phi}(x, q_y), \qquad (3.22)$$

where the convolution (*) is now done along the *x* only, $r = \sqrt{(x - x_d)^2 + z_d^2}$, and $K_\upsilon(z)$ is the modified Bessel function of the second kind. The equations for the induced field become

$$E_{g,\alpha}(x_c, z_c) = \int_0^\infty dx \int_{-\infty}^\infty \frac{dq_y}{2\pi} \frac{2}{\kappa} \frac{u_\alpha}{r} \mid q_y \mid K_1(u \mid q_y \mid) \delta\tilde{\rho}(x, q_y), \ \alpha = \{x, z\}, \qquad (3.23)$$

where $u_x = x_c - L$, $u_z = z_c$, and $u = \sqrt{u_x^2 + u_z^2}$.

In our simulations we had to compute $E_{g,\alpha}$ numerically for a large number of collocation points (x_c, z_c) and source dipole positions (x_d, z_d). For this purpose, we converted the above integral equations into linear equations of a finite size. Instead of a semi-infinite plane, we assumed that graphene occupies a strip $0 < x < 2w$ of a large width $2w$. We discretized the *x* coordinates and replaced all derivatives by finite differences. The convolution integral was replaced by an integral sum. A special care was taken to regularize the divergence of the modified Bessel functions at zero arguments by requiring that the convolution gives the same result for $\delta\tilde{\rho} = \text{const}$ whether it is computed numerically or analytically at all points of the *x*-grid. Similarly, we introduced a grid of q_y extending up to a suitably large value. Grid parameters were adjusted to ensure that the accuracy of our solution was never less than 1%. The sequence of steps involved in our

numerical simulations is explained further in Sec. IV.

3.8.4 Tip-sample coupling

The goal of the modeling was to understand the imaging contrast, i.e., relative variations of the scattering amplitude *S* measured by s-SNOM as a function the AFM tip position.

Fully realistic simulations of the tip-sample coupling are computationally prohibitive, and so we tried several approximations. The first approximation we considered was the conventional the point-dipole model [32-34]. This simple model did grasp some of the key characteristics of the imaging contrast. However, it came short of a quantitative account of the experimental data. Much better agreement was obtained using the model in which the AFM tip is approximated by a metallic spheroid [35]. The spheroid is defined by the equation

$$(x-L)^2 = \frac{\alpha}{L_{tip}}(z-z_{tip})(2L_{tip}+z_{tip}-z),\ z_{tip} \le z \le z_{tip}+2L_{tip}, \tag{3.24}$$

where L is the x-coordinate of the tip, $2L_{\text{tip}}$ is its total length, and a is its radius of curvature at the ends. The desired scattering amplitude S is proportional to the total radiating dipole p_z of the spheroid. (For a strongly elongated spheroid, $L_{\text{tip}} >> a$, its in-plane dipole moment is much smaller than p_z and can be neglected.) In order to compute p_z, we assume that the electric potential $\Phi_{\text{ext}}(\mathbf{r}, z)$ outside both the tip and the sample can be represented as a superposition of potentials of a large number N_{d} of point dipoles positioned inside the tip:

$$\tilde{\Phi}_{ext}(\mathbf{r},z) = \sum_{j=1}^{N_d} p_j \Phi_d(r_{d,j}-r,\ z_{d,j}-z). \tag{3.25}$$

Using the formalism developed in Sec. III, we compute the full potential $\Phi(\mathbf{r}, z)$ and the corresponding electric field $\mathbf{E}(\mathbf{r}, z)$ at N_d collocation points $(x_{c,j}, z_{c,j})$ at the spheroid surface. Imposing the boundary condition that the component of $\mathbf{E}(r, z)$ tangential to this surface is zero, we obtain the system of linear equations for the individual dipole moments p_j. The total dipole moment p_z of the tip is their sum.

We tested this algorithm first on the case of infinite graphene, where the accuracy of the solution for p_z as a function of z_{tip}, L_{tip}, and a can be verified by independent numerical methods [7]. We found that accuracy better than 1% can be reached by working with $N_d \geq 2L_{tip}/a$ dipoles positioned equidistantly on the spheroid axis $z_{d,j} = z_{tip} + 2L_{tip}/N_d)\,(j - 1/2)$. The z-coordinates of the collocation points were taken to coincide with those of the dipoles, $z_{c,j} = z_{d,j}$. Their x-coordinates were all chosen to be on the same side of L, i.e., $x_{c,j} > L$. The same sets of points were later used for the problem of the graphene strip. In principle, in this case the off-axis placement of the dipoles may be warranted and also both $x_{c,j} > L$ and $x_{c,j} < L$ should be considered. However, investigation of these issues requires time-consuming computations and so it is left for future work. In any case, for aspect ratios $L_{tip}/a = 2\text{-}10$, we found our numerical results to be stable as long as N_d was about $2L_{tip}/a$ or larger and at the same time the minimal distance between the tip and the sample was not smaller than $0.1a$. Regarding the latter, we note that although the distance between the tip and the sample can nominally be zero, the tip is covered by a Pt-Ir film with a skin depth ~ 20nm. Therefore, even in this case using some finite positive value for z_{tip} is physically justified in our electromagnetic calculations.

In the experiment the AFM is used in the tapping mode and the tapping harmonics

$s_m e^{i\phi_m}$ are recorded. We modeled this by considering the time-dependent z_{tip} in the form

$$z_{tip}(t) = z_{\min} + \Delta z(1-\cos\Omega t), \tag{3.26}$$

Computing $S(t) \propto p_z(t)$ for a suitably dense grid of *t*-points and taking the discrete Fourier transform at frequency mΩ, the desired demodulated amplitudes $s_m e^{i\phi_m}$ can be obtained.

The simulations proceed as follows. Given a profile of $q_p(x)$ (see Sec. V) and a pair of the tip coordinates (L, z_{tip}), the matrices of the linear systems are generated as discussed above. These linear equations are solved and the magnitudes of the effective dipoles are computed. Their sum is taken to be the scattering amplitude S (up to an unimportant multiplicative constant). These calculations are repeated for a grid of tip positions L (typically, a hundred points) and heights z_{tip} (20 points). Upon demodulation, the spatial profile of $s_3(L)$ is computed. Normalizing it by s_3 calculated for the reference Si substrate (without graphene), the relative amplitude $s(L)$ is obtained. These results are then utilized to fit the experimental data for $s(L)$ (Fig. 3.1), as described in the next section.

3.8.5 Data fitting procedure

The input into our simulation consists of the tip modeling parameters a, L_{tip}, $z_{\min}$, the known tapping amplitude Δz = 40 nm, the value of $\kappa(\omega$ = 892 cm^{-1}) = 2.52 + 0.13i (based on our ellipsometric measurements of SiO_2/Si wafers), and also the spatial profile of $q_p(L)$. For notation consistency with Fig. 3.2c, we relabel x to L in this section.

We fixed a = 30 nm, similar to our previous work [13]. We tried several L_{tip}/a ratios and found the results not to be very sensitive to this parameter, as long as it is large. We

settled on $L_{tip}/a = 9$ for numerical efficiency. For $q_p(L) = q_1(L) + iq_2(L)$ we adopted the polynomial form

$$q_1(x) = \sum_{j=0}^{6} a_j L^j, \quad q_2(L) = \gamma_p q_1(L). \tag{3.27}$$

For simplicity, the plasmon damping parameter γ_p was taken to be position-independent. The coefficients a_j were iteratively adjusted until a good agreement with the measured s_3 profile was obtained, see Fig. 3.4. The minor discrepancies between the experiments and simulations could be due to a systematic error introduced by the spheroid approximation (after all, the tip is not an ideal metallic spheroid) and the lack of perfect translational invariance of the system along the edge.

For ungated sample, $V_g = 0$, we made additional checks. The fitted $q_1(L)$ was converted into the profile of the carrier (in this case, hole) density $n(L)$ with the help of the relation

$$n(L) = \frac{1}{\pi} k_F^2(L), \quad k_F(L) = \frac{\hbar\omega^2}{2e^2 v} \frac{|\kappa|}{q_1(L)}, \tag{3.28}$$

which follows from Eqs. 3.10 and 3.11. This determination of $n(L)$ was verified by micro-Raman measurements. As one can see from Fig. 3.2c, both the magnitude of the carrier density increase toward the graphene edge and the length scale over which this increase occurs are consistent with the Raman data. In fact, the near-field and the Raman methods give complementary information about the local density. The former is most reliable in the range $0 < L \le 400$ nm while the latter is accurate at $L \ge 1\,\mu$m. These two groups of results were interpolated by another polynomial function

$$n(L) = \sum_{j=0}^{6} c_j \, |L(nm)|^j \times (10^{12} cm^{-2}), \tag{3.29}$$

where c_7 = -4.062191×10^{-21}, c_6 = 2.999730×10^{-17}, c_5 = -8.646941×10^{-14}, c_4 = 1.210092×10^{-10}, c_3 = -8.233038×10^{-8}, c_2 = 2.506465×10^{-5}, c_1 = -0.008350, and c_0 = 8.861376. This interpolation is shown by the solid line in Fig. 3.2c of the main text.

3.9 Acknowledgements

Authors acknowledge support from AFOSR, DOE and ONR. W.B, Z.Z, and C.N.L were supported by NSF DMR/1106358, ONR N00014-09-1-0724, ONR/DMEA H94003-10-2-1003 and FENA focus center. G.D. and M.T. were supported by NASA. M.F. is supported by UCOP and NSF PHY11-25915. A.H.C.N. acknowledges NRF-CRP grant R-144-000-295-281. M.W. thanks the Alexander von Humboldt Foundation for financial support. F.K. was supported by Deutsche Forschungsgemeinschaft through the Cluster of Excellence Munich Centre for Advanced Photonics.

Chapter 3, in full, is a reprint of the material as it appears in Z. Fei, A. S. Rodin, G. O. Andreev, W. Bao, A. S. McLeod, M. Wagner, L. M. Zhang, Z. Zhao, G. Dominguez, M.Thiemens, M. M. Fogler, A. H. Castro-Neto, C. N. Lau, F. Keilmann, D. N. Basov, "Gate-tuning of graphene plasmons revealed by infrared nano-imaging", Nature 487, 82–85 (2012). The dissertation author was the primary investigator and author of this paper.

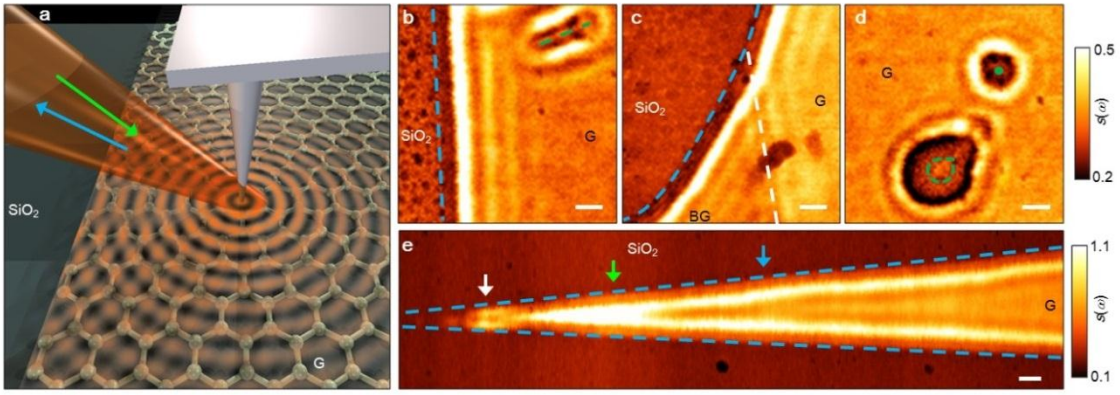

Figure 3.1: Infrared nano-imaging experiment and results. (a) Schematic of an infrared nano-imaging experiment at the surface of graphene (labeled as G) on SiO_2. Green and blue arrows display the directions of incident and back-scattered light, respectively. Concentric red circles illustrate plasmon waves launched by the illuminated tip. (b-e**)** Images of infrared amplitude $s(\omega = 892\ cm^{-1})$ defined in the text taken at zero gate voltage. These images show a characteristic interference pattern close to graphene edges (blue dashed lines), defects (green dashed lines), at the boundary between single (G) and bilayer (BG) graphene (white dashed line). Additional features marked with the arrows in (e**)** are analyzed in Refs. 15,16. Locations of boundaries and defects were determined from AFM topography taken simultaneously with the near-field data. Scale bars are 100 nm in all panels. All data were acquired at ambient conditions.

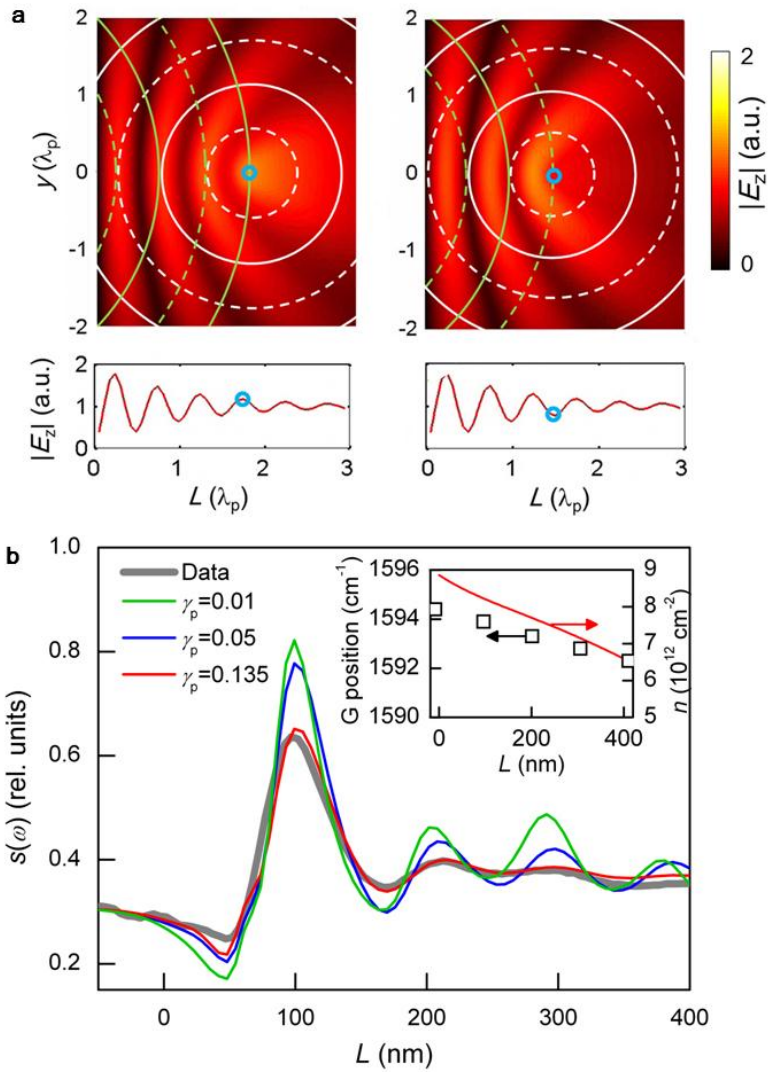

Figure 3.2: Spatial variation of the near-field amplitude at the graphene edge. For all panels, graphene extends at $L > 0$, and SiO_2 not covered by graphene is displayed at $L < 0$. (a) Illustration of interference between tip-launched plasmon waves (white) and their reflection (green) from the edge at $L = 0$. Solid and dashed lines correspond to positive and negative field maxima of the propagating plasmon, respectively. False color plots of the absolute value of electric field $|E_z|$ reveal standing waves formed between the tip and the edge. Left and right panels show snapshots of destructive (minimum signal) and constructive (maximum signal) interference underneath the tip, respectively. Scale bar, $0.5\lambda_p$. We also plot profiles of $|E_z|$ underneath the tip versus its distance to the edge. The blue circles and arrows mark the positions of the tip. (b) Experimental (grey) and calculated (color) $s(\omega)$ line profiles at zero gate voltage. Inset shows the G-peak positions inferred from micro-Raman data and the carrier density profile (red line) we used to model the plasmonic standing wave (panel b). The Raman G-peak positions are associated with the variation of the local carrier density in graphene (right-hand scale) [19-21].

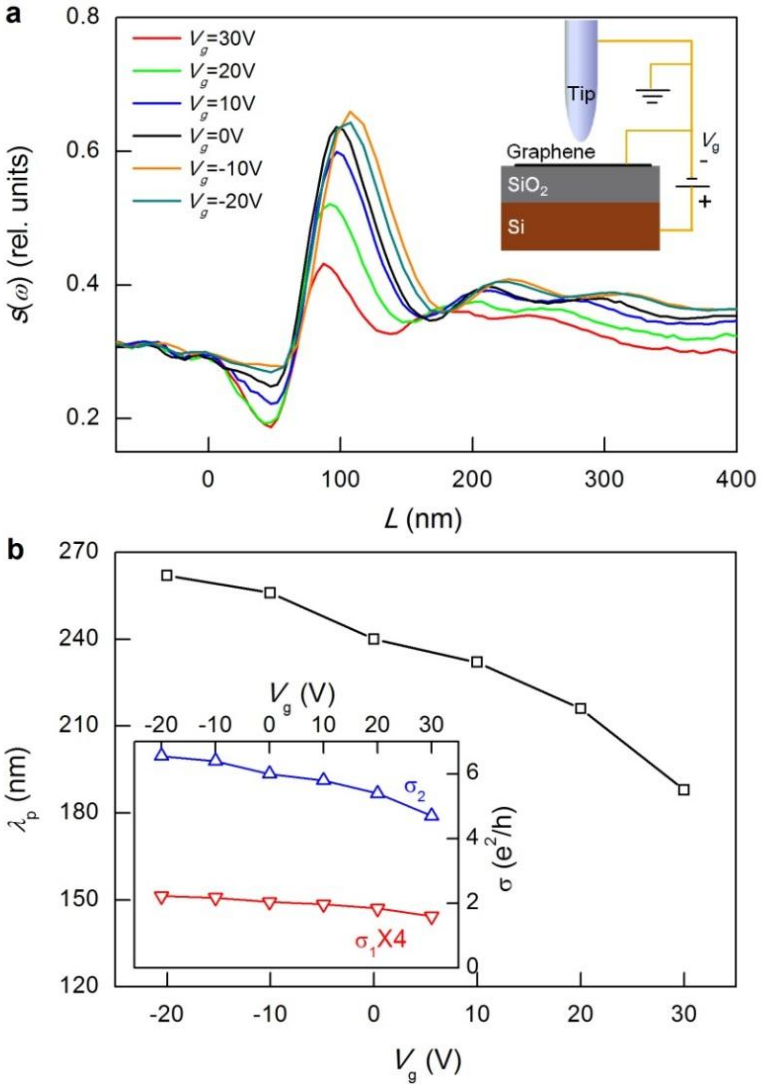

Figure 3.3: Electrostatically tunable plasmon in back-gated graphene. (a) $s(\omega)$ line profiles perpendicular to the graphene edge at various gate voltages. Inset illustrates our gate bias setup. (b) Gate-dependent plasmon wavelength λ_p. Inset displays the real and imaginary part of the optical conductivity of graphene at various gate voltages estimated from λ_p and γ_p as described in the text. These conductivity data directly show that the response of graphene is predominantly reactive: $\sigma_2 >> \sigma_1$ thus fulfilling an essential precondition for excitation of plasmons.

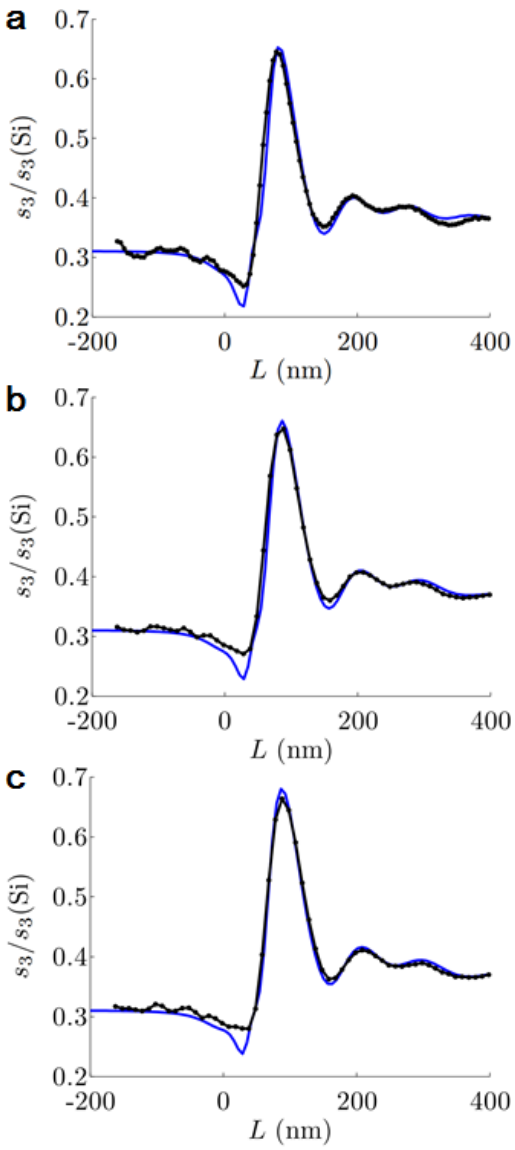

Figure 3.4: Fitting of the graphene plasmon fringe profiles taken at different gate voltages. (a-c) Line profiles of the 3rd harmonic near-field amplitude of graphene normalized to silicon for gate voltages V_g = -20, -10, and 0 V, respectively. The black dots connected by the lines are the experimental data; the blue solid lines are the theoretical fits using γ_p = 0.135.

2.10 Bibliography

1. H. A. Atwater, Sci. Am. **296**, 56–63 (2008).

2. P. R. West, Laser & Photon. Rev. 1-13 (2010).

3. M. I. Stockman, Phys. Today **64**, 39-44 (2011).

4. S. A. Maier, Plasmonics: Fundamentals and Applications Ch. 4 (Springer, New York, 2007).

5. J. A. Schuller, E. S. Barnard, W. Cai, Y. C. Jun, J. S. White, and M. L. Brongersma, Nature Mater. **9**, 193-204 (2010).

6. P. Nagpal, N. C. Lindquist, S.-H. Oh, and D. J. Norris, Science **325**, 594-597 (2009).

7. S. Lal, S. Link, and N. J. Halas, Nature Photon. **1**, 641-648 (2007).

8. A. H. Castro-Neto, F. Guinea, N. M. R. Peres, K. S. Novoselov, and A. K. Geim, Rev. Mod. Phys. **81**, 109-162 (2009).

9. F. Wang, Y. Zhang, C. Tian, C. Girit, A. Zettl, M. Crommie, and Y. R. Shen, Science **320**, 206-209 (2008)

10. Z. Q. Li, E. A. Henriksen, Z. Jiang, Z. Hao, M. C. Martin, P. Kim, H. L. Stormer, and D. N. Basov, Nature Phys. **4**, 532-535 (2008).

11. A. Vakil and N. Engheta, Science **332**, 1291-1294 (2011).

12. M. Jablan, H. Buljan, and M. Soljacic, Phys. Rev. B **80**, 245435 (2009).

13. Z. Fei, G. O. Andreev, W. Bao, L. M. Zhang, A. S. McLeod, C. Wang, M. K. Stewart, Z. Zhao, G. Dominguez, M. Thiemens, M. M. Fogler, M. J. Tauber, A. H. Castro Neto, C. N. Lau, F. Keilmann, and D. N. Basov, Nano Lett. **11**, 4701-4705 (2011).

14. L. Ju, B. Geng, J. Horng, C. Girit, M. Martin, Z. Hao, H. A. Bechtel, X. Liang, A. Zettl, Y. R. Shen, and F. Wang, Nature Nanotech. **6**, 630-634 (2011).

15. J. Chen, M. Badioli, P. Alonso-Gonzalez, S. Thongrattanasiri, F. Huth, J. Osmond, M. Spasenovic, A. Centeno, A. Pesquera, P. Godignon, A. Z. Elorza, N. Camara, F. J. G. de Abajo, R. Hillenbrand, and F. H. L. Koppens, Nature **487**, 77-81 (2012).

16. A. S. Rodin, Electronic Properties of Low-Dimensional Systems (PhD thesis of UCSD, 2012).

17. A. Huber, N. Ocelic, D. Kazantsev, and R. Hillenbrand, Appl. Phys. Letts. **87**,

081103 (2005).

18. R. Dallapiccola, C. Dubois, A. Gopinath, F. Stellacci, and L. Dal Negro, Appl. Phys. Lett. **94**, 243118 (2009).

19. A. Das, S. Pisana, B. Chakraborty, S. Piscanec, S. K. Saha, U. V. Waghmare, K. S. Novoselov, H. R. Krishnamurthy, A. K. Geim, A. C. Ferrari, and A. K. Sood, Nature Nano. **3**, 210-215 (2008).

20. C. Casiraghi, A. Hartschuk, , H. Qian, S. Piscanec, C. Georgi, A. Fasoli, K. S. Novoselov, D. M. Basko, and A. C. Ferrari, Nano. Lett. **9** 1433-1441 (2009).

21. J. M. Caridad, F. Rossella, V. Bellani, M. Maica, M. Patrini, and E. Diez, J. Appl. Phys. **108**, 084321 (2010).

22. E. H. Hwang and S. Das Sarma, Phys. Rev. B **75**, 205418 (2007).

23. T. Ando, Y. Zheng, and H. Suzuura, J. Phys. Soc. Jpn. **71**, 1318–1324 (2002).

24. N. M. R. Peres, F. Guinea, and A. H. Castro Neto, Phys. Rev. B **73**, 125411 (2006).

25. V. P. Gusynin, and S. G. Sharapov, Phys. Rev. B **73**, 125411 (2006).

26. L. Novotny and B. Hecht, Principles of Nano-Optics (Cambridge University Press, New York, 2006).

27. A. G. Grushin, B. Valenzuela, and M. A. H. Vozmediano, Phys. Rev. B **80**, 155417 (2009).

28. N. M. R. Peres, R. M. Ribeiro, A. H. Castro-Neto, Phys. Rev. Lett. **105**, 055501 (2010).

29. J. Hwang, J. P. F. Leblanc, and J. P. Carbotte, J. Phys.: Condens. Matter **24**, 245601 (2012).

30. F. Rana, Nano. IEEE Trans. **7**, 91 (2008).

31. B. Wunsch, T. Stauber, F. Sols, and F. Guinea, New J. Phys. **8**, 318 (2006).

32. R. Hillenbrand and F. Keilmann, Phys. Rev. Lett. **85**, 3029 (2000).

33. T. Taubner, F. Keilmann, and R. Hillenbrand, Nano Lett. **4**, 1669 (2004).

34. J. Aizpurua, T. Taubner, F. J. G. de Abajo, M. Brehm, and R. Hillenbrand, Opt. Express **16**, 1529 (2008).

35. L. M. Zhang, G. O. Andreev, Z. Fei, A. S. McLeod, G. Dominguez, M. Thiemens, D. N. Basov, A. H. Castro Neto, and M. M. Fogler, Phys. Rev. B **85**, 075419 (2012)

Chapter 4

Electronic and plasmonic phenomena at graphene grain boundaries

4.1 Introduction

Graphene [1], a two-dimensional honeycomb lattice of carbon atoms, is of great interest in (opto)electronics [2,3] and plasmonics [4-11] and can be obtained by means of diverse fabrication techniques, among which chemical vapor deposition (CVD) is one of the most promising for technological applications [12]. The electronic and mechanical properties of CVD-grown graphene depend in large part on the characteristics of the grain boundaries [13-19]. However, the physical properties of these grain boundaries remain challenging to characterize directly and conveniently [15-23]. Here, we show that it is possible to visualize and investigate the grain boundaries in CVD-grown graphene using an infrared nano-imaging technique. We harness surface plasmons that are reflected and scattered by the graphene grain boundaries, thus causing plasmon interference. By recording and analyzing the interference patterns, we can map grain boundaries for a

large area CVD-grown graphene film and probe the electronic properties of individual grain boundaries. Quantitative analysis reveals that grain boundaries form electronic barriers that obstruct both electrical transport and plasmon propagation. The effective width of these barriers (~10-20 nm) depends on the electronic screening and it is on the order of the Fermi wavelength of graphene. These results uncover a microscopic mechanism that is responsible for the low electron mobility observed in CVD-grown graphene, and suggest the possibility of using electronic barriers to realize tunable plasmon reflectors and phase retarders in future graphene-based plasmonic circuits.

4.2 Experimental details

Our imaging technique, which we refer to as 'scanning plasmon interferometery', is implemented in a setting of an antenna-based infrared (IR) nanoscope [6-8]. A schematic diagram of the scanning plasmon interferometry technique is shown in Fig. 4.1a. Infrared light focused on a metalized tip of an atomic force microscope (AFM) generates a strong localized field around the sharp tip apex, analogous to a "lightning-rod" effect [24]. This concentrated electric field launches circular SPs around the tip (pink circles in Fig. 4.1a). The process is controlled by two experimental parameters: the wavelength of light λ_{IR} and the curvature radius of the tip R. In order to efficiently launch SPs on our highly doped graphene films, we chose IR light with λ_{IR} close to 10 μm and AFM tips with $R \approx$ 25 nm (Methods). The experimental observable of the scanning plasmon interferometry is the scattering amplitude s that is collected simultaneously with AFM topography.

4.3 Data and Analysis

4.3.1 Crack-type line defect

Before analyzing the GBs, we first discuss a crack-type line defect with a geometric width of ~10 nm, thus visible in the AFM topography (blue arrows in Fig. 4.1b). The corresponding scanning plasmon interferometry image is displayed in Fig. 4.1c, where we plot the scattering amplitude *s* at λ_{IR} = 11.3 μm. The scattering signal shows bright twin fringes running along this line defect. In the same field of view, we also observed a region of double-layer graphene (blue dashed loop) and a microscopic line structure (green shaded region) in Fig. 4.1b. All these features are commonly found in CVD graphene (Fig. 4.3a) [12]. The bright circular fringes are observed near the edge of the double-layer region (Fig. 4.1c). By tuning λ_{IR} from 11.3 μm (Fig. 4.1c) to 10.5 μm (Fig. 4.1d), the fringe widths of both types of fringes show evident λ_{IR}-dependence, which is consistent with the plasmonic origin of these patterns [7,8]. Note that the scattering amplitude in all our scanning plasmon interferometry images is normalized to that of a sample region where no fringes exist (e.g. the green square in Fig. 4.1c).

In previous studies [7,8], plasmon fringes with a width of half the plasmon wavelength $\lambda_p/2$ were observed close to the edge of graphene microcrystals. In order to validate the plasmonic origin of the fringes found here, we plot in Fig. 4.1f the width of the twin fringes (circles) as a function of λ_{IR}. In the same diagram we also show a theoretical cacluation (see Methods for details). The agreement between the experimental data and the calculated curve confirms that the bright fringes at the line defects are of the plasmonic origin in close analogy with the oscillations of the scattering amplitude at the

edges of graphene. In either case, the near-field signal is formed by a standing wave with the periodicity $\lambda_p/2$ produced by the interference between the tip-launched and reflected plasmons [7,8].

4.3.2 Grain boundaries

We observed twin fringes not only close to the cracks but also near other types of line defects that we identified as wrinkles and grain-overlaps based on the AFM topography (Fig. 4.4). But the most prevailing line defects are grain boundaries (schematically illustrated in Fig. 4.1a with a red line). As a rule, GBs are of the atomic length scale thus are invisible in typical AFM scans (Fig. 4.2a). Yet GBs were vividly visualized by scanning plasmon interferometry producing characteristic twin fringes (Fig. 4.2b,d). We examined the λ_{IR}-dependence of the fringe width and found that it is in agreement with the theoretical calculation (red circles in Fig. 4.1f). This latter finding attests to the plasmonic origin of the scanning plasmon interferometry signal at GBs.

So far we discuss mainly the fringe width that is a direct measure of λ_p. Yet another important parameter is the separation between twin fringes D_{TF} (Fig. 4.1e). For GBs, D_{TF} can be written as $D_{TF} \approx (-\delta / 2\pi)\lambda_p$, where δ is the plasmon phase shift upon reflection off a grain boundary set to vary within [-2π, 0] (Eq. 4.19). Therefore, for a non-zero constant δ, the magnitude of D_{TF} is proportional to λ_p, which was indeed confirmed by our experiment (Fig. 4.1f). Our data indicated that D_{TF} roughly equals to $1/2\lambda_p$ for all GBs, and therefore δ is close to $-\pi$. Note that the parameter δ is not solely determined by the response of our graphene samples. The AFM tip also plays an

important role here. As detailed in Section 4.6.4, it is convenient to write δ as $\delta = \delta_{sp} + \delta_t$, where δ_{sp} is the plasmon phase shift without tip coupling to graphene, and δ_t is a tip-dependent parameter that is around $-(0.5\pm0.1)\pi$ based on our numerical modeling (Eq. 4.19).

The above analysis for D_{TF} holds true also for other types of line defects with geometric features much smaller than λ_p, such as the crack shown in Fig. 4.1b. Nevertheless, for line defects such as wrinkles and grain-overlaps (Fig. 4.4), the twin fringes are strongly affected by their geometric form. As detailed in Section 2 of the Supplementary Information, these two types of line defects generate twin fringes with considerable variations of D_{TF} governed by the details of a particular defect. A unique feature of GBs and grain-overlaps is that they together form a network of closed regions (grains) spanning over the entire graphene film (Figs. 4.2e and 4.5). In contrast, cracks and wrinkles are sporadic and discontinuous. From Fig. 4.2e, we were able to measure the average grain size (3-5μm) of our film, in agreement with reports for graphene prepared under identical conditions [21].

4.4 Modeling and Discussion

In order to gain quantitative understanding of the twin fringes in our scanning plasmon interferometry images, we performed numerical modeling that takes into account all the experimental details. In our modeling, we assumed that GBs locally modify the plasmon wavelength λ_p and damping rate γ_p. Here, γ_p is defined by the ratio

between the imaginary and real parts of the plasmon wavevector $q_p \equiv \frac{2\pi}{\lambda_p}(1+i\gamma_p)$. We found that the profiles of $\lambda_p(x)$ and $\gamma_p(x)$ displayed in Fig. 4.2f produce an accurate fit of the experimental data taken at multiple λ_{IR} in the range of 10.7–11.3 μm (Figs. 4.2c and 4.9). Details of the modeling are given in Section 4.6.5. The fact that the single set of parameters fits the totality of fringe profiles indicates that the choice of these parameters is quite robust. For example, an assumption of a dip in $\lambda_p(x)$ as opposed to a peak at the GB would almost double D_{TF} (see Fig. 4.7a and following paragraphs). We remark that strong scattering quantified with γ_p in concert with the enhancement of λ_p at the GB is needed to reproduce the line shape of the twin fringes.

We now discuss some of the implications of our modeling. According to the plasmon dispersion equation (Section 4.6), λ_p is roughly proportional to E_F. In turn, E_F scales as a square root of the carrier density n. Thus our results imply that our graphene film tends to be heavily doped with $n \approx 4\times10^{13}$ cm^{-2} at the GBs, corresponding to 0.021 holes per unit cell. This is expected since GBs are lattice defects that favor molecule adsorptions at ambient conditions [25,26]. The role of defects in enhancing doping due to molecule adsorption has been extensively studied before [27,28]. In contrast, under ultra-high-vacuum conditions, where molecule adsorption is significantly reduced, graphene films are close to the charge neutrality point and GBs perturbed the electronic properties of graphene in a totally different way as confirmed by scanning tunnel microscopy studies [18]. The plasmon damping rate depends on the carrier scattering rate of graphene τ^{-1}: $\gamma_p \approx 0.05 + (\omega\tau)^{-1}$ (Eq. 4.21). Therefore, the lineform of $\gamma(x)$ inferred from modeling implies that charge carriers experience enhanced scattering close to the

GBs. We speculate that this effect may be caused by the coulomb scattering due to the charges at the GBs. Furthermore, modeling indicates that GBs perturb electronic properties over a length scale of the order of 20 nm. A wider effective width compared to the geometric width is in fact an outcome of electron screening of the charged GBs [29]. Indeed, the charge screening length is estimated to be in the order of Fermi wavelength, roughly 10 nm in our doping range, consistent with our experimental findings.

Based on the $\lambda_p(x)$ and $\gamma_p(x)$ profiles in Fig. 4.2f, we can calculate the $E_F(x)$ and $\tau^{-1}(x)$ profiles across GBs. These latter parameters allow us to infer the DC conductivity σ_{DC} of graphene (inset of Fig. 4.2c) with a standard formula [11]: $\sigma_{DC} \approx \frac{2e^2}{h}\frac{E_F}{\hbar\tau^{-1}}$. This equation is obtained by assuming weak frequency dependence of τ^{-1} that is valid when coulomb scattering dominates [11]. Although the increase of the E_F near the GBs would normally boost σ_{DC}, this expected trend is overwhelmed by the increase in τ^{-1}. The net effect for GBs is to significantly reduce the local σ_{DC} of graphene.

Finally, we wish to point out that the plasmon reflection off GBs can be described by a reflection coefficient r_{sp}. By solving analytically the problem of SPs scattering by GBs, we were able to obtain a formula: $r_{sp} \approx iW_{eff}\Delta q_p$ (Eq. 4.14), where Δq_p is the relative change of plasmon wavevector due to GBs and W_{eff} is the effective width. Based on r_{sp}, we were able to estimate both the plasmon reflection probability $|r_{sp}|^2$ and the phase shift $\delta_{sp} = \arg(r_{sp})$. The former is closely related to the fringe intensity, and the latter determines D_{TF} as discussed above. Calculations based on the λ_p and γ_p profiles of the GB (Fig. 4.2f) yield $|r_{sp}|^2 \approx 8\%$ and $\delta_{sp} \approx -0.6\pi$. The 8% reflectivity is remarkably high.

Such a strong reflection is due to the extended effective width of the electronic perturbation induced by the GBs (Fig. 4.2f). A phase shift of $\delta_{sp} \approx -0.6\pi$ is an outcome of higher doping at the GB. If one switches the GB to a lower doping, δ_{sp} will undergo a "π" phase shift and become -1.6π, resulting in a dramatic increase of D_{TF} away from the experimental value (Fig. 4.7a). The above analysis indicates that $|r_{sp}|^2$ and δ_{sp} are sensitive to the doping of the plasmon reflector. Therefore both of these parameters governing plasmon propagation can be conveniently tunable by common electronic means, e.g. electrostatic gating.

4.5 Conclusion and Outlook

Our work provided for the first time unambiguous experimental evidence of novel plasmonic effects originating from plasmon reflection at GBs in CVD graphene. The scanning plasmon interferometry technique, aided with modeling, is a comprehensive method capable of mapping and probing the electronic properties of GBs. This method can be applied to nano-characterization of plasmonic materials beyond graphene, where GBs also play important roles in the plasmonic effects [30]. Moreover, our work provides guidelines to designing tunable electronic barriers that would realize reconfigurable plasmon reflectors [4] and phase retarders: a milestone towards graphene-based plasmonic circuits.

4.6 Methods summary

Our graphene films were grown on copper foils using a two-step low pressure

CVD method [12], and then transferred to silicon wafers with 300 nm SiO_2 layer on top. All experiments were performed under ambient conditions and in an atmospheric environment. The graphene films were unintentionally hole-doped with a carrier density of about 1.0×10^{13} cm^{-2} corresponding to a Fermi energy E_F of 0.37 eV. Such high doping is due to the SiO_2 substrate, as well as molecule adsorption in the air atmosphere [26,27]. The doping level was inferred from our Raman and near-field gating experiments (Section 4.6.1).

The scanning plasmon interferometry experiments introduced above were performed at UCSD using a scattering-type scanning near-field optical microscope (s-SNOM) [24]. Our s-SNOM is a commercial system (neaspec.com) equipped with mid-IR quantum cascade lasers (daylightsolutions.com) and CO_2 lasers (accesslaser.com) covering a wavelength range of 9.5–11.3 μm. The s-SNOM equipped with a pseudo-heterodyne interferometric detection module is based on an atomic force microscope (AFM) operating in the tapping mode with a tapping frequency around 270 kHz. The output signal of s-SNOM utilized in this work is the scattering amplitude s demodulated at n^{th} harmonics of the tapping frequency (n = 2 in the current work).

In order to efficiently couple IR light to the graphene plasmons, an AFM tip with a radius $R \approx 25$ nm was chosen as our near-field probe. This scheme allowed us to overcome the notorious "momentum mismatch" between plasmons and photons. As detailed in Ref. 13, the momenta-coupling function has a bell-shaped momenta distribution that peaks at $q \sim 1/R$. For a typical CVD graphene film on the SiO_2 substrate, the momentum of IR plasmons at ambient conditions is between $3 - 6\times10^5$ cm^{-1}. Therefore the optimum tip radius for exciting SPs of graphene in our frequency range is

about 20-30 nm.

The plasmon dispersion equation of graphene [7,11] at the interface between air and SiO_2 substrate with dielectric function $\varepsilon_{sub}(\omega)$ is given as $q_p = \frac{i2\omega\varepsilon_0\kappa(\omega)}{\sigma(\omega)}$, where $\omega=2\pi c/\lambda_{IR}$ is the IR excitation frequency, $\kappa(\omega) = [1+\varepsilon_{sub}(\omega)]/2$ is the effective dielectric function of the environment for graphene, $\sigma(\omega)$ is the optical conductivity of graphene . The plasmon wavelength λ_p of graphene can be obtained with $\lambda_p=2\pi/\mathrm{Re}(q_p)$. The optical conductivity we used to calculate the plasmon wavelength (×1/2) in Fig. 4.1f was obtained from the random phase approximation method [6,7]. We find an excellent agreement between the experimental data and calculations of $1/2\lambda_p$ assuming a Fermi energy $E_F \approx 0.37$ eV that is in accord with our Raman measurements.

Alternatively, one can use a Drude formula that is valid at a limit of long wavelength and low frequency: $\sigma(\omega) = i\frac{e^2}{\pi\hbar^2}\frac{E_F}{\omega+i\tau^{-1}}$, where e is the elementary charge, $\hbar$ is the reduced Plank constant, and τ^{-1} is the charge scattering rate in graphene. In this case, plasmon wavelength λ_p adopts an analytic form: $\lambda_p \approx \frac{e^2 E_F \lambda_{IR}^2}{h^2 c^2 \varepsilon_0 \,\mathrm{Re}\,\kappa}$.

4.7 Supplementary information

4.7.1 CVD graphene fabrication and characterization

Our graphene films were gown on copper foil using a two-step low pressure chemical vapor deposition (CVD) method as described in Ref. 12, and then transferred to

SiO_2/Si wafers. A typical image taken with optical microscope is shown in Fig. 4.3a, where one can see that our CVD graphene film is predominantly single layer graphene. In addition, there are sporadic dark spots (green arrow) and lines (blue arrows) dispersed inside the film: a common occurrence in CVD graphene films [12]. These dark spots are the regions of two- or three-layer graphene whereas dark lines are microscopic line structures. We remark that these line structures are of the microscopic length scale, orders of magnitude wider than the nanoscale line defects investigated in this work. The double-layer region in Fig. 4.1b marked with blue dashed loop is one of these dark spots, while the green shaded region in Fig. 4.1b is one of these microscopic line structures.

Raman spectroscopy (Senterra, Bruker Inc.) was applied to characterize our graphene films. All our Raman measurements were carried out using a 532 nm excitation laser, a 50× (NA=0.75) objective, and a grating with 1200 lines per millimeter. The laser spot size is roughly 1 μm, and the spectral resolution is 3 cm^{-1}. An accuracy of ~1 cm^{-1} can be achieved by band-fit when determining the peak positions for G and 2D bands. We kept our laser power below 2 mW to avoid heating [31]. Raman spectra were collected all across our graphene films to characterize our film quality and doping level. A typical spectrum taken away from any dark spots or dark lines (Fig. 4.3a) is given in Fig. 4.3b. A symmetric 2D peak verified that our film is a single layer graphene, while a vanishing D peak indicates that our film is of high crystalline quality. According to previous studies, the G peak position is sensitive to the doping level of graphene [27,32,33]. The average G peak position of Raman spectra taken at different locations is around 1595 ± 1 cm^{-1} indicating extremely high doping in our CVD graphene film.

To estimate the carrier polarity and density of our graphene film, we investigated

the gating dependence of the near-field IR response by monitoring the hybrid plasmon-phonon resonance around ω = 1150 cm^{-1}. At this frequency, the scattering amplitude *s* scales monotonically with the doping level of graphene [8], thus offering a convenient way to estimate the doping level of graphene. As shown in Fig. 4.3c, $s(\omega$ = 1150 cm^{-1}) decreases systematically with increasing gate voltage V_g. The charge neutral point V_{CN} is above V_g = 80 V and exceeds the breakdown voltage of the SiO_2 layer in our structure. Albeit incomplete, these gating results nevertheless conclusively show that our graphene films are highly hole-doped at ambient conditions.

Based on the combination of our Raman and near-field gating experiments, we estimated that the hole density of our CVD graphene film was around $(1.0\pm0.3)\times10^{13}$ cm^{-2}. The corresponding Fermi energy E_F is about 0.37 ± 0.06 eV estimated from $E_F = \hbar v_F\sqrt{\pi n}$, where $v_F \approx 1\times10^6$ m/s is the Fermi velocity. This high level of doping likely originates from both SiO_2 substrate and molecule adsorption in air atmosphere [26,34].

4.7.2 Nomenclature of line defects

In addition to the cracks and grain boundaries (GBs) introduced in above, we also found other types of line defects including wrinkles and grain-overlaps. In Fig. 4.4, we plot both atomic force microscopy (AFM) (Figs. 4.4a,d) and scanning plasmon interferometry (SPI) (Figs. 4.4b,e) images for these two types of line defects. All SPI images were taken at λ_{IR}=11.3 μm and share the same color scale. For the purpose of quantitative analysis, in the right panels of Fig. 4.4, we plot the line profiles across the

twin fringes of these line defects.

Wrinkles (i.e. film corrugations) in CVD graphene are formed during either post-growth cooling or film transfer processes [12]. Here we only discuss wrinkles in the nanometer length scale. As shown in Fig. 4.4b, wrinkles also generate twin fringes similar to cracks and GBs indicating that they also reflect surface plasmons (SPs). Nevertheless, the fringe intensity and separation between the twin fringes D_{TF} for wrinkles are different from position to position (Figs. 4.4b). Such differences are due to the variations of the structural morphologies [35] of these wrinkles at different locations.

Grain-overlaps are line defects formed when one grain overlaps with another, so that they bridge different grains [17]. Unlike GBs, grain overlaps are clearly visible in AFM topography. There are two grain-overlaps here in Fig. 4.4d (marked with OL1 and OL2), producing only ~1 nm variation in the AFM topography. Despite their similarity in the topography, OL1 and OL2 trigger totally different twin fringes (Fig. 4.4e). The twin fringes of OL1 are very close to each other, while those of the OL2 are much further apart. Both of them are different from the twin fringes triggered by a GB (marked with a red arrow in Fig. 4.4e). The different SPI response of the two grain-overlaps might be related to the stacking order of the overlapped region.

In Fig. 4.5, we show a larger-area scan of our CVD graphene film including various types of line defects. Based on the AFM topography (Fig. 4.5a) and SPI (Fig. 4.5b) images, we were able to sketch a map for various types of line defects (Fig. 4.5c). Topographic and SPI signatures allowing us to distinguish different types of line defects are described in the manuscript and the above paragraphs. Being sub-nm wide defects, GBs have no obvious topography features, yet they trigger clearly observable plasmonic

twin fringes. Grain overlaps and wrinkles show up in both the AFM topography and the SPI images. The main difference between grain-overlaps and wrinkles is the degree of continuity and the intensity of the twin fringes. The wrinkles are sporadic and discontinuous with fringe intensity varying from position to position. The grain-overlaps are continuous (similar to GBs) with almost constant fringe intensities. High-resolution AFM and SPI images (like Figs. 4.3 and 4.4) are well suited to discriminate between all these different types of line defects.

4.7.3 Reflection of plasmons from a linear defect

The observed fringes originate from interference of the plasmon waves launched by the AFM tip and those backscattered by a linear defect. Here we only consider line defects with negligible geometric width, such as a GB. Theoretical modeling of such waves is a challenging problem that requires solving complicated integro-differential equations. The problem becomes more manageable once one introduces certain approximations for the response functions of graphene and the tip, as described in our previous work [6]. However, even after these approximations the solution can be obtained only numerically. Before we go into details of our numerical simulations (Section 4.6.5), we first consider a simpler scattering problem, which can be tackled analytically.

Instead of a complicated waveform launched by the tip, we consider a plane wave incident from the left on the line defect located at $x = 0$. We take the scalar potential of this wave to be $\phi(x, y) = e^{iq_x x + iq_y y}$ in the graphene plane. The system is assumed to be uniform along y, so that q_y is conserved. The x-component of the incident plasmon momentum is

$$q_x = \sqrt{q_\infty^2 - q_y^2}, \ \ \mathrm{Im}\, q_x \geq 0, \tag{1}$$

where $q_\infty \equiv q_p(\infty)$, function $q_{\mathrm{p}}(x)$ is the local plasmon momentum,

$$q_p(x) = \frac{i\kappa\omega}{2\pi\sigma(x)}, \ \ \kappa = \frac{\varepsilon_{sub}+1}{2}, \tag{2}$$

$\sigma(x)$ is the local sheet conductivity of graphene, and κ is the effective dielectric constant. We parameterize the deviation of $q_{\mathrm{p}}(x)$ from its limiting value at infinity by the dimensionless function $g(x)$ such that

$$\frac{1}{q_p(x)} = \frac{1+g(x)}{q_\infty}. \tag{3}$$

We assume that $g(x)$ rapidly decays with x (faster than $1/x$). Note that the plasmon wavelength is defined by $\lambda_p(x) \equiv 2\pi / q_1$ with $q_1 = \mathrm{Re}\, q_p(x)$

Our goal is to calculate the potential $\psi(x)e^{iq_y y}$ of the scattered wave. In particular, we are interested in the behavior of $\psi(x)$ at large negative x,

$$\psi(x) \approx r_{sp} e^{-iq_x x} = \mid r_{sp} \mid e^{-iq_x x + i\delta_{sp}}, \tag{4}$$

which defines the reflection probability $|r_{sp}|^2$ and the phase shift δ_{sp} of graphene plasmons.

Our starting equations are:

$$\Phi(x) \equiv \phi(x,0) + \psi(x), \tag{5}$$

$$\Phi(x) \equiv V_1 * \{\frac{1+g(x)}{q_\infty} q_y^2 \Phi(x) - \partial_x \frac{1+g(x)}{q_\infty} \partial_x \Phi(x)\}, \tag{6}$$

where $\Phi(x)$ is the total potential, $V_1 = \pi^{-1} K_0(q_y x)$ is the 1D Fourier transform of the Coulomb potential, $K_0(z)$ is the modified Bessel function of the second kind, and the star denotes convolution,

$$\Phi(x) \equiv \phi(x,0) + \psi(x), \tag{7}$$

We approach Eq. 4.6 using the Green's function perturbation theory method. The Green's function is defined by

$$G(x) = \int \frac{dk'}{2\pi} \frac{e^{ikx}}{\varepsilon(k, q_y)}, \ \varepsilon(k_x, k_y) = 1 - \frac{\sqrt{k_x^2 + k_y^2}}{q_\infty}. \tag{8}$$

The physical meaning of *G* is the response to the localized disturbance; $\varepsilon(k_x, k_y)$ is the 2D dielectric function of graphene. Using contour-integration techniques, the Green's function can be split into two terms:

$$G(x) = -\frac{iq_\infty^2}{q_x} e^{iq_x|x|} + \Delta G(x). \tag{9}$$

The first term represents the outgoing plane wave and the second term is a correction decaying as $\Delta G(x) \sim (q_y x)^{-3/2}$ for $q_y \neq 0$ and $\Delta G(x) \sim 2/(q_\infty x)^2$ for $q_y = 0$. In the latter case, $\Delta G(x)$ can be expressed in terms of the standard special functions, the cosine-integral Ci(*z*) and the sine-integral Si(*z*):

$$\Delta G(x) = -\frac{q_\infty}{\pi} \{\mathrm{Ci}(q_\infty x) \cos q_\infty x + [\mathrm{Si}(q_\infty x) - \frac{\pi}{2}] \sin q_\infty x\}. \tag{10}$$

Using thus defined Green's function, Eq. 4.6 can be transformed to

$$\psi(x) = \frac{1}{q_\infty} (G * V_1) * \{g(x) q_y^2 \Phi(x) - \partial_x g(x) \partial_x \Phi(x)\}, \tag{11}$$

which is analogous to the Lippmann-Schwinger equation of the usual scattering theory. Following the familiar route, at *x* much longer than plasmon wavelength λ_p, we neglect the correction $\Delta G(x)$ in $G(x)$ and recover Eq. 4.5 with the following reflection coefficient:

$$r_{sp} = -\frac{i}{q_x}\int_{-\infty}^{\infty} dx e^{iq_x x}[q_y^2 g(x)\Phi(x) - \partial_x g(x)\partial_x \Phi(x)]. \quad (12)$$

We restrict our further analysis to the case of a weak defect, i.e., small $g(x)$. In this case $|r_{sp}| << 1,\ \Phi(x) \approx e^{iq_x x}$, and the formula similar to the first Born approximation applies:

$$r_{sp} \approx i\frac{q_x^2 - q_y^2}{q_x}\tilde{g}(-2q_x),\ \tilde{g}(k) \equiv \int_{-\infty}^{\infty} dx e^{-ikx} g(x). \quad (13)$$

Notably, the reflection vanishes at the "Brewster angle" of $\pi/4$ where $q_x=q_y$. However, we are primarily interested in the normal incidence ($q_y = 0$). The most important for us is the situation where the effective electronic width of the defect is small compared to the plasmon wavelength: $W_{eff} << \lambda_p$. In this case, for $q_y = 0$, Eq. 4.4 acquires a remarkably simple form

$$r_{sp} \approx iW_{eff}\Delta q_p,\ \Delta q_p \equiv \frac{1}{W_{eff}}\int [q_p(x) - q_\infty]dx. \quad (14)$$

Parameter Δq_p has the meaning of the average deviation of $q_p(x)$ inside the defect region from its limiting value q_∞. In turn, the phase shift of graphene plasmons is given by

$$\delta_{sp} = \arg(iW_{eff}\Delta q_p). \quad (15)$$

For real Δq_p, δ can take only two values: $\delta_{sp} = -\pi/2$ if $\Delta q_p < 0$, (i.e., λ_p inside the defect is higher than outside), and $\delta_{sp} = -3\pi/2$ otherwise. On the other hand, if Δq_p also has an imaginary part, the phase shift can be arbitrary.

4.7.4 Interference pattern formation

Let us now apply the above results to the task of interpreting the positions of the

interference fringes found in the experiment, i.e., the tip positions $\boldsymbol{\rho}_t = (x_t, y_t)$ where the nanoscope registers the maxima of the signal $s(\boldsymbol{\rho}_t)$. The relation between $s(\boldsymbol{\rho}_t)$ and the previously discussed scalar potential $\Phi(\boldsymbol{\rho})$ is complicated and in fact tip-dependent[8]. However, according to our numerical simulations, the maxima of $s(\boldsymbol{\rho}_t)$ occur roughly where the scalar potentials $\phi(\boldsymbol{\rho})$ and $\psi(\boldsymbol{\rho})$ due to, respectively, the launched and the scattered waves, add in phase underneath the tip. The results of the previous section can be straightforwardly utilized provided the tip is located far away from the linear defect. Assuming that is the case, let us discuss the launched wave $\phi(\boldsymbol{\rho})$ first. Near the defect, which is far from the tip, $\phi(\boldsymbol{\rho})$ behaves as an outgoing cylindrical wave:

$$\phi(\boldsymbol{\rho}) \approx C_0 e^{i\delta_t} \frac{\phi(\boldsymbol{\rho}_t)}{\sqrt{q_p \,|\, \boldsymbol{\rho} - \boldsymbol{\rho}_t \,|}} e^{-iq_p|\boldsymbol{\rho}-\boldsymbol{\rho}_t|}, \; q_p \,|\, \boldsymbol{\rho} - \boldsymbol{\rho}_t \,| >> 1. \tag{16}$$

The coefficient $C_0 \sim 1$ and the phase shift δ_t depend on microscopic parameters of the tip, graphene, and the substrate. There is no general reason for δ_t to be negligible.

Next, consider the reflected wave $\psi(\boldsymbol{\rho})$. To compute this function, one can decompose $\phi(\boldsymbol{\rho})$ into Fourier harmonics with all possible q_y, determine the reflected wave for each harmonic, and then evaluate the inverse Fourier transform at the tip position. It is easy to see that the reflected wave is dominated by harmonics of nearly normal incidence, $q_y \sim | q_p / x_t |^{1/2} << q_p$. This allows one to replace function $r(q_y)$ in this calculation by the constant $r(0)$. In turn, it means that the method of images applies, so that $\psi(\boldsymbol{\rho})$ can be approximated by a cylindrical wave of a certain amplitude radiated from the position $(-x_t, y_t)$. This argument is the theoretical basis for the illustration shown in Fig.

4.1a. Adding together the launched and the reflected waves, we find the total potential at the tip position:

$$\frac{\Phi(\boldsymbol{\rho}_t)}{\phi(\boldsymbol{\rho}_t)} \approx 1 + \frac{C_0 \mid r(0) \mid}{\sqrt{2q_p \mid x_t \mid}} e^{2iq_p|x_t| + i\delta_g + i\delta_t},\ q_p \mid x_t \mid >> 1. \tag{17}$$

According to the earlier assumption, the interference maxima occur when $2q_1 \mid x_t \mid + \delta_{sp} + \delta_t$ is an integer multiple of 2π. They form a sequence of equidistant points on each side of the defect:

$$\mid x_t \mid = \frac{\lambda_p}{2}\left(n + \{-\frac{\delta_{sp} + \delta_t}{2\pi}\}\right), \tag{18}$$

where $n = 0, 1, \ldots$ and $\{z\}$ stands for the fractional part of z. Although Eq. 4.18 was derived assuming $n >> 1$, it should not be grossly incorrect at $n = 0$. Therefore, the separation between the maxima nearest to the defect is:

$$D_{TF} \approx \left\{-\frac{\delta_{sp} + \delta_t}{2\pi}\right\}\lambda_p. \tag{19}$$

Thus the magnitude of D_{TF} is governed both by the plasmon phase shift δ_{sp}, and by the tip-dependent parameter δ_t. Based on our numerical modeling results given in Fig. 4.7 and Eqs. 4.15 and 4.19, we were able to estimate δ_t to be $-(0.5\pm0.1)\pi$, which is fairly robust for tip radius from 10 nm to 100 nm. The estimation was done by comparing D_{TF} inferred using Eq. 4.19 with that obtained from modeled profiles. The value of $-(0.5\pm0.1)\pi$ is fairly accurate for all the test modeling profiles. Slight deviation (less than 20%) occurs when $g(x)$ or Δq_p is relatively big, i.e. when λ_p^{LD} is 100 nm or 800 nm in Fig. 4.7a.

4.7.5 Numerical modeling about the fringe profiles

Many elements of our numerical modeling have already been described in Ref. 7. In short, we model our AFM tip as a metallic spheroid (Fig. 4.6a): the length of the spheroid is 2*L* and the radius of curvature at the tip end is *R*. Here, *R* is set to be 25 nm according to the manufacturer specification and *L* is not a sensitive parameter so long as it is much larger than *R* (*L* is set to be 9*R* in all our simulations). The scattering amplitude *S* (before demodulation) is proportional to the total radiating dipole p_z of the spheroid. Therefore, in order to fit the line profiles perpendicular to the twin fringes due to a line defect, we need to calculate p_z at different spatial coordinates (x, z_{tip}). Here, *x* and *z* are the *x*- and *z*- coordinates of lower end of the AFM tip, respectively. In order to compute p_z, we assume that the electric potential Φ outside both the tip and the sample can be represented as a superposition of potentials of a large number of point dipoles positioned inside the tip. Based on this assumption, we are able to calculate the electric potential Φ and field **E** distribution at every given point of the space. Imposing the boundary condition that the component of **E** tangential to the tip is zero, we obtain individual dipole moments. The total dipole moment p_z of the tip is their sum. By calculating p_z at different *z*, we are able to perform 'demodulation' of the scattering amplitude *S* and get different harmonics of the scattering signal. While calculating p_z at different *x* allows us to plot the modeling scattering amplitude and phase profiles. In all our modeling and simulation, we assume no position dependence in the *y*- direction for the purpose of simplicity. In the current work, the scattering amplitude *s* is normalized to that far away from the line defect where no plasmon fringes exist.

As for graphene, in our previous work [7] we used the complex plasmon wavevector q_p (Eq. 4.2) as an input parameter in our modeling. Equivalently here, the plasmon wavelength $\lambda_p=2\pi/\mathrm{Re}(q_p)$ and the damping rate $\gamma_p=\mathrm{Im}(q_p)/\mathrm{Re}(q_p)$ are the input parameters. We start with a model that assumes that graphene has a constant plasmon wavelength λ_p^G and damping rate γ_p^G away from the line defect, and that a line defect with an effective width of W_{eff} is characterized by its own plasmon wavelength λ_p^{LD} and damping rate γ_p^{LD} as illustrated in Fig. 4.6b. Here and below, this model is referred to as the Discontinuous Model. Among the four parameters, both λ_p^G and γ_p^G can be estimated directly from our experimental data. λ_p^G is set to be around 260 nm by measuring the fringe width of two side fringes at $|x| \approx 230$ nm. γ_p^G is estimated to be around 0.15 by comparing the plasmon damping to that of exfoliated graphene [7].

To understand how λ_p^{LD}, γ_p^{LD} and W_{eff} affect the plasmon fringe profile, we first perform a series of modeling by varying only one parameter and fixing the other two constant. In Fig. 4.7, we show fours representative sets of modeling results by:

(1) varying λ_p^{LD} from 10 to 800 nm with $\gamma_p^{LD}=\gamma_p^G=0.15$ and $W_{eff} \approx 30$ nm (Fig. 4.7a);

(2) varying γ_p^{LD} from 0.01 to 2.0 with $\lambda_p^{LD}=500$ nm and $W_{eff} \approx 30$ nm (Fig. 4.7b);

(3) varying γ_p^{LD} from 0.01 to 2.0 with $\lambda_p^{LD}=100$ nm and $W_{eff} \approx 30$ nm (Fig. 4.7b);

(4) varying W_{eff} from 5 to 80 nm with $\lambda_p^{LD}=500$ nm and $\gamma_p^{LD}=0.5$ (Fig. 4.7d).

In all panels of Fig. 4.7, we plot the modeling scattering amplitude *s* profiles along with the experimental data for a GB in Fig. 4.2. The scattering amplitude *s* is normalized to its value far away from the line defect, $|x| \geq 300$ nm in Fig. 4.7. We monitor the evolution of both the fringe intensity (peak height) and the separation between twin

fringes D_{TF} with varying λ_p^{LD}, γ_p^{LD} or W_{eff}. As explained above, the fringe intensity is related to the reflection probability $|r|^2$ (Eq. 4.14), while D_{TF} is determined by the phase shift δ_{sp} (Eq. 4.19).

As one can see in Fig. 4.7a, the further λ_p^{LD} deviates from λ_p^{G}, the higher the fringe intensity is. This is consistent with Eq. 4.14 since larger $|\lambda_p^{LD}-\lambda_p^{G}|$ leads to larger Δq_p and hence higher reflection probability $|r|^2$. The separation between the twin fringes D_{TF} also depends on λ_p^{LD}. Assuming $\lambda_p^{LD} > \lambda_p^{G}$, we can find simulation parameters that bring D_{TF} close to the experimentally observed width 150 nm. Conversely, if we assume that $\lambda_p^{LD} < \lambda_p^{G}$, the magnitude of D_{TF} becomes too large, about 260nm, nearly twice the observed value. This is again consistent with the analytical theory above. When $\lambda_p^{LD}-\lambda_p^{G}$ switches its sign, plasmon phase shift $\delta_{sp} = \arg(iW_{eff}\Delta q_p)$ will be shifted by π (Eq. 4.15), resulting in drastic change in D_{TF} (Eq. 4.19).

Now we examine the effects of γ_p^{LD} on the plasmon fringe profiles. In Figs. 4.7b,c, we show the modeling results with λ_p^{LD} fixed at 500 nm and 100 nm, respectively. In both cases, the fringe profile evolves systematically with varying γ_p^{LD}, in agreement with Eqs. 4.14 and 4.19. Notably, in the case of λ_p^{LD}=500 nm, the scattering amplitude *s* at the line defect ($x \approx 0$) shows a sensitive dependence on γ_p^{LD}. Good agreement with the experimental data can be achieved only if $\lambda_p^{LD}>\lambda_p^{G}$, i.e., if the GB is more doped than the rest of the film

The modeling results for several W_{eff} are presented in Fig. 4d, where one can see that the fringe intensity decreases rapidly with decreasing W_{eff}. This is because $|r|$ scales with W_{eff} as shown in Eq. 4.14. At the smallest $W_{eff} \approx 5$ nm, the twin fringes almost

disappear. As W_{eff} increases, the separation between the twin fringes D_{TF} increases by about the same amount.

Figure 4.7d illustrates how the calculated $s(x)$ profiles change as a function of a single parameter of the set ($\lambda_{\text{p}}^{\text{LD}}$, $\gamma_{\text{p}}^{\text{LD}}$ or W_{eff}) while the remaining ones are kept fixed. Finally, in Fig. 4.8, we vary all the three parameters in order to get the best fit to the data. Such a fit is achieved with W_{eff} close to 20 nm, which is much larger than its geometric width < 1 nm. Effective widths much smaller than 20 nm, e.g., $W_{\text{eff}} \approx 5$ nm， require setting $\lambda_{\text{p}}^{\text{LD}}$ as high as 3000 nm to fit the data, corresponding to an unrealistic carrier density of $n = 1.2 \times 10^{15}$ cm^{-2}.

So far, for the purpose of simplicity and clarity, we use the Discontinuous model (Fig. 4.6b) for calculation. Clearly, the model grasps the gross features of the experimental data. Nevertheless, in this model both $\lambda_{\text{p}}(x)$ and $\gamma_{\text{p}}(x)$ profiles have discontinuities close to the line defect (Fig. 4.7). We also considered a more realistic model that was referred to as the Gradual Model (Fig. 4.6c). In this model the rapid increase of both λ_{p} and γ_{p} close to the line defect is modeled by exponential functions:

$$\lambda_{\text{p}}(x) = \lambda_{\text{p}}^{\text{G}} + A_1 e^{-2|x|/B},\ \gamma_{\text{p}}(x) = \gamma_{\text{p}}^{\text{G}} + A_2 e^{-2|x|/B}. \qquad (20)$$

Here A_1, A_2 and B are the new adjustable parameters. A_1 and A_2 determine the peak height of λ_{p} and γ_{p} at the center of the line defect, respectively (Fig. 4.6c), B is associated with the effective width of the line defect.

In Fig. 4.9, we show the best-fit results for the GB data taken at λ_{IR} from 10.7 to 11.3 μm using the Gradual model. The modeling parameters are: A_1 = 320 nm, A_2 = 0.9, B = 20 nm, corresponding $\lambda_{\text{p}}(x)$ and $\gamma_{\text{p}}(x)$ profiles are plotted in Fig. 4.2e.

4.7.6 Discussion about the modeling results

Our modeling with both models not only fits well the experimental data, but also uncovers many essential properties of GBs. (1) GBs tend to have higher λ_p compared to the rest of CVD film. (2) GBs tend to have higher γ_p compared to the rest of CVD film. (3) GBs tend to have higher effective width (W_{eff} ~ 20 nm) than their geometric width (W < 1nm).

According to Section 4.5, plasmon wavelength λ_p of graphene is proportional to its Fermi energy E_F. Considering that $E_F = \hbar v_F \sqrt{\pi n}$ (v_F is the Fermi velocity, n is the carrier density of graphene), higher λ_p implies an increase of the carrier densities in the vicinity of GBs. This is expected since GBs are lattice imperfections that favor molecule adsorptions at ambient conditions [25,36], which will further enhance the hole doping in ambient [27,28]. Within the Drude approximation, the plasmon damping rate γ_p in graphene can be written as [7]

$$\gamma_p = \frac{q_2}{q_1} \approx \frac{\kappa_2}{\kappa_1} + \frac{\sigma_1}{\sigma_2} = 0.05 + \frac{1}{\omega\tau}, \tag{21}$$

here κ_1 and κ_2 are the real and imaginary parts of effective dielectric constant κ (Eq. 4.2), and σ_1 and σ_2 are real and imaginary parts of optical conductivity of graphene σ, $1/\tau$ is the scattering rate of the charge carriers (as labeled in Fig. 4.8c). Therefore, higher γ_p indicates higher scattering rate $1/\tau$ close to the GBs. These additional scattering originates presumably from the strong structural and Coulomb disorder at the GB.

The effective electronic width W_{eff} ~ 20 nm of the GBs revealed by the SPI is comparable to the screening length in graphene and is much larger than the sub-nm

geometric width of the grain boundaries. The relevant screening problem has been considered in Ref. 29 within the perturbation-theory approach.

Starting from the E_F and $1/\tau$ profiles displayed in Figs. 4.8b,c, we are able to calculate the DC conductivity profile across the GB using the formula obtained under Drude approximation:

$$\sigma_{DC} = \frac{2e^2}{h}\frac{E_F}{E_\Gamma}, \tag{S22}$$

here $E_\Gamma = \hbar\tau^{-1}$ is the scattering energy. The obtained $\sigma_{DC}(x)$ is given in the inset of Fig. 4.2c, where one can see that the GB tends to have a lower DC conductivity compared to the rest of the graphene film.

Previous transport and STM studies [15,16,18,19] of GBs were all performed in vacuum. Graphene was much less doped in those studies. On the contrary, our experiments were carried out in ambient atmospheric conditions, thus revealing for the first time the transport properties of GBs in graphene films that are highly hole-doped (presumably, by oxygen and water molecules). We remark that the 'electronic' nature of the GBs are the origin for the lower DC conductivities observed in our experiments.

4.8 Acknowledgements

Authors acknowledge support from ONR. The development of scanning plasmon interferometry is supported by DOE-BES. G.D. and M.T. were supported by NASA. M.F. is supported by UCOP and NSF PHY11-25915. A.H.C.N. acknowledges NRF-CRP grant R-144-000-295-281. M.W. thanks the Alexander von Humboldt Foundation for financial

support. F.K. was supported by Deutsche Forschungsgemeinschaft through the Cluster of Excellence Munich Centre for Advanced Photonics.

Chapter 4, in full, is a reprint of the material as it appears in Z. Fei, A. S. Rodin, W. Gannett, S. Dai, W. Regan, M. Wagner, M. K. Kiu, A. S. McLeod, G. Dominguez, M.Thiemens, M. M. Fogler, A. H. Castro-Neto, F. Keilmann, A. Zettl, R. Hillenbrand, M. M. Fogler, D. N. Basov, “Electronic and plasmonic phenomena at grain boundaries in chemical vapor deposited graphene”, Nature Nanotech. 8, 821-825 (2013). The dissertation author was the primary investigator and author of this paper.

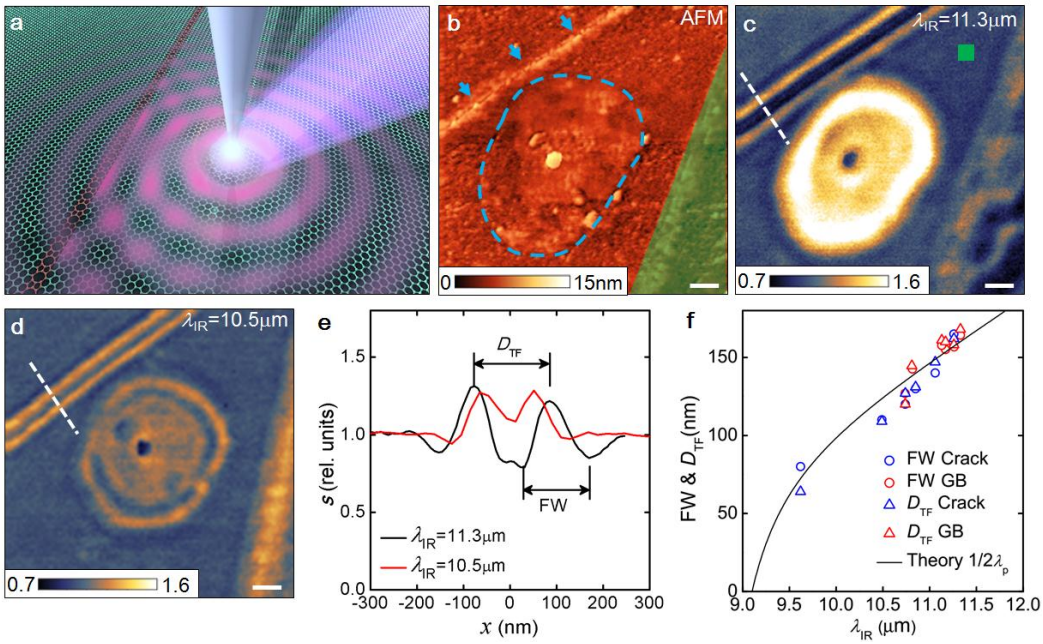

Figure 4.1: Probing CVD graphene with scanning plasmon interferometry. (a) Illustration of the scanning plasmon interferometry principle. The AFM tip (silver cone) illuminated with infrared (IR) light (purple cone) launches surface plasmon waves (pink circles) in graphene. These waves are partially reflected by the line defect (red line) thus causing interference between the launched and back-reflected plasmonic waves. (b) AFM topography of CVD graphene revealing a crack-type line defect (blue arrows), double-layer graphene region (blue dashed loop), and a microscopic line structure (green shaded region). (c, d) Scanning plasmon interferometry images taken simultaneously with the AFM topography in (b) at IR wavelength λ_{IR}=11.3 μm and 10.5 μm, respectively. (e) Line profiles taken along the white dashed lines in (c) and (d). Here we also illustrate, for the 11.3 μm case, a protocol to extract the fringe width (FW) and the separation between the twin fringes D_{TF}. (f), Evolution of fringe width (circles) and D_{TF} (triangles) with λ_{IR} for the crack (blue) in Fig. 4.1b and the grain boundary (GB) in Fig. 4.2 (red). The black solid line is a theoretical result for the magnitude of $1/2\lambda_p$ assuming the Fermi energy $E_F \approx 0.37$eV (Methods). Note that λ_p decreases rapidly for $\lambda_{IR} < 10$ μm: a consequence of the plasmon coupling to the surface optical phonon of SiO_2. The data range for GBs is narrower than that that of the crack due to the fact that GB is a less efficient plasmon reflector compared to the crack. Scanning plasmon interferometry images (c) and (d) show the normalized amplitude *s* of the nano-optic signal as described in the text. Scale bars in (b-d) are all 200 nm.

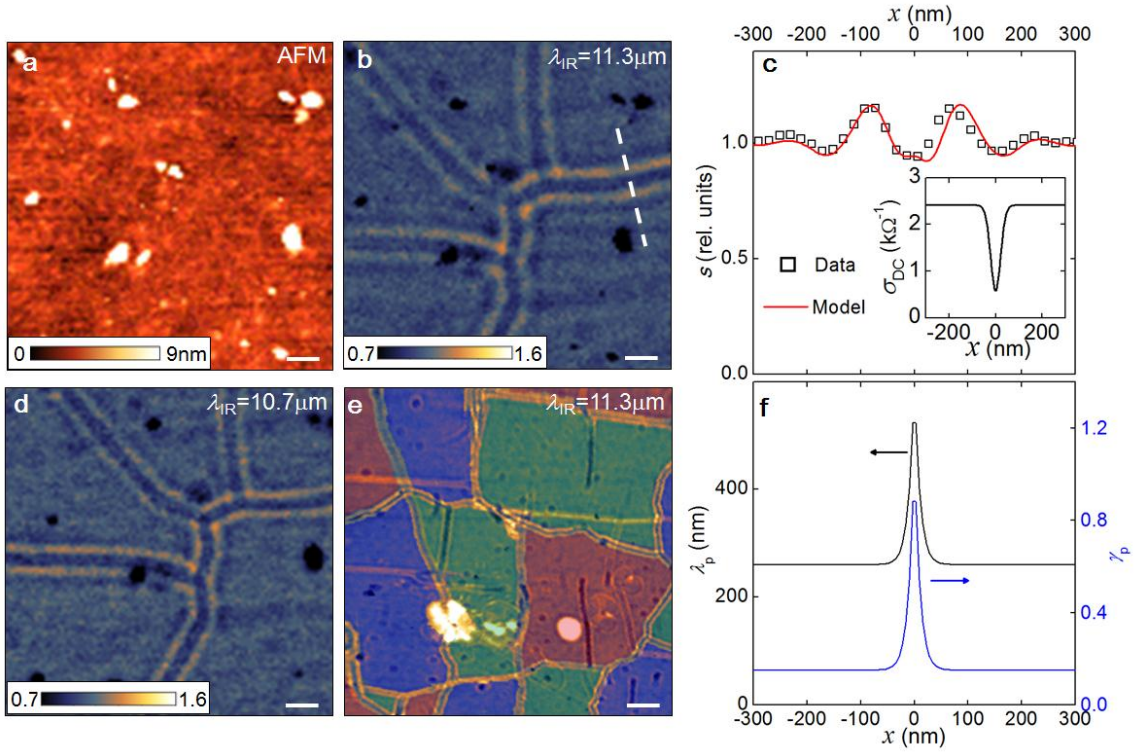

Figure 4.2: Grain boundaries observed in CVD graphene films. (a) Topography image of graphene containing GBs. (b) Scanning plasmon interferometry image simultaneously taken with (a) at λ_{IR}=11.3 μm revealing GBs. (c) Experimental (black squares) and modeled (red curves) twin fringe profiles. The experimental profile is taken along the dashed line in (b). The inset shows the profile of DC conductivity inferred from modeling. (d) Scanning plasmon interferometry image of the same sample area of (b) taken at λ_{IR}=10.7 μm. (e) A larger-area scan of a typical sample revealing multiple grains (displayed with different false colors) defined by the twin fringes due to GBs and grain-overlaps. Details of line defects arrangements in this map are given in Fig. 4.5. (f) The profiles of plasmon wavelength λ_p and damping rate γ_p used for modeling the fringe profiles of the GB shown in **c** and Fig. 4.9. Scale bars in (a, b, d) are 200 nm, and the scale bar in (e) is 1 μm.

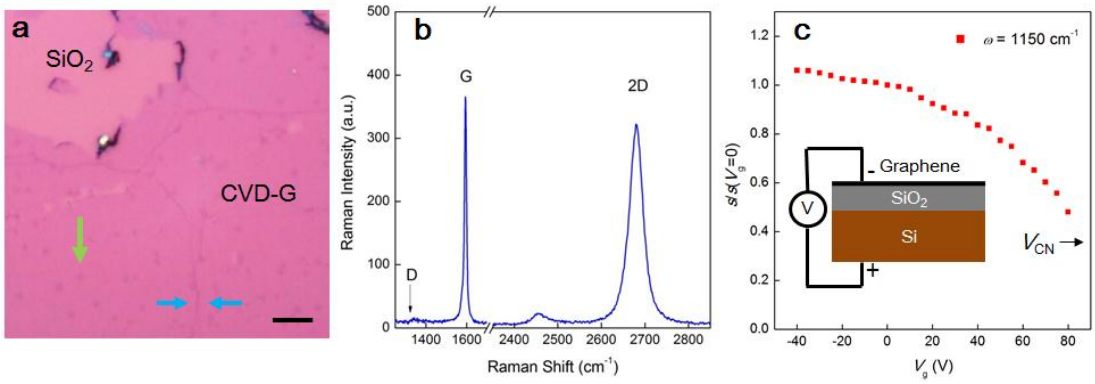

Figure 4.3: Optical and Raman characterization of CVD graphene. (a) A typical optical image of our graphene film. CVD-G represents the CVD graphene film. Green arrow marks a dark spot and blue arrows mark a microscopic line structure, both of which are commonly seen in graphene films fabricated with CVD methods. Scale bar, 10 μm. (b) A typical Raman spectrum of our graphene film away from any dark spots or dark lines shown in (a). (c) Scattering amplitude $s(\omega = 1150\ \mathrm{cm}^{-1})$ at various gate voltages V_g normalized to that at $V_g = 0$ V.

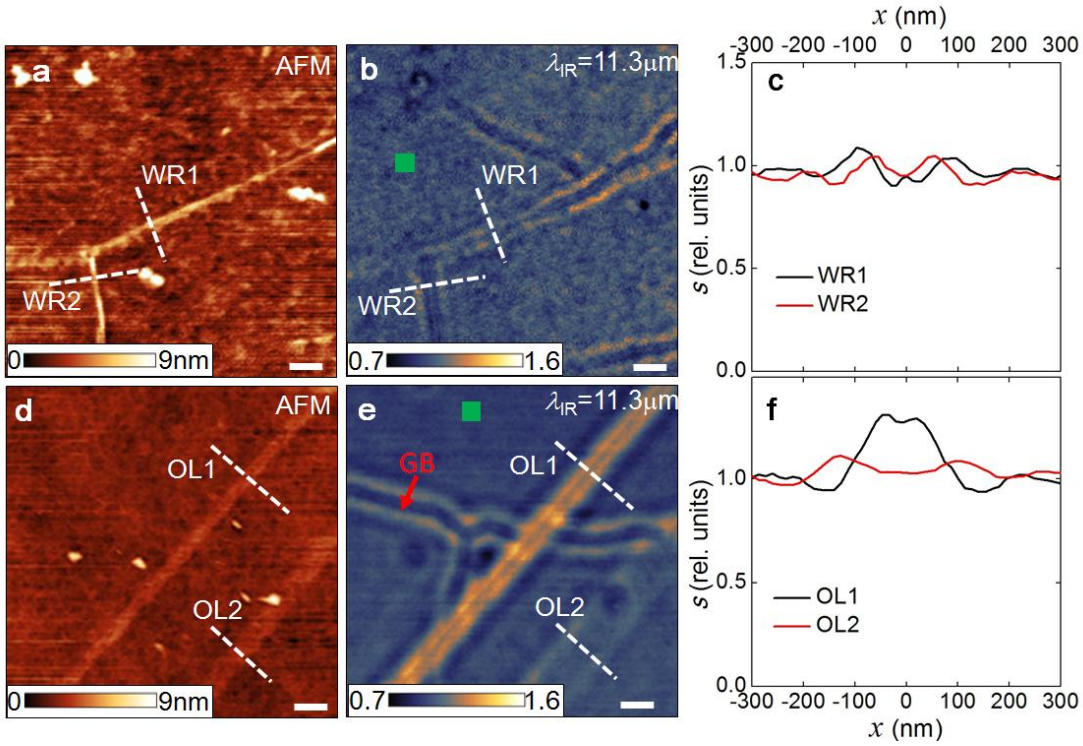

Figure 4.4: Near-field characterization of wrinkles and grain-overlaps. (a) Topography image showing wrinkles. (b) SPI image taken simultaneously with (a) at λ_{IR}=11.3 μm. WR1 and WR2 in (a,b) mark the two wrinkles. (c) The line profiles taken along the dashed lines in (b). (d) Topography image of grain-overlaps. (e) SPI image taken simultaneously with (d) at λ_{IR}=11.3 μm. Red arrow marks a GB. OL1 and OL2 in (c) and (d) mark two different types of grain-overlaps. (f) The line profiles taken along the dashed lines in (e). In both (c) and (f), the scattering amplitude *s* is normalized to the places far away from the line defects where no plasmons fringes exist (e.g. green squares in (b) and (f)). Scale bars in all panels are 200 nm.

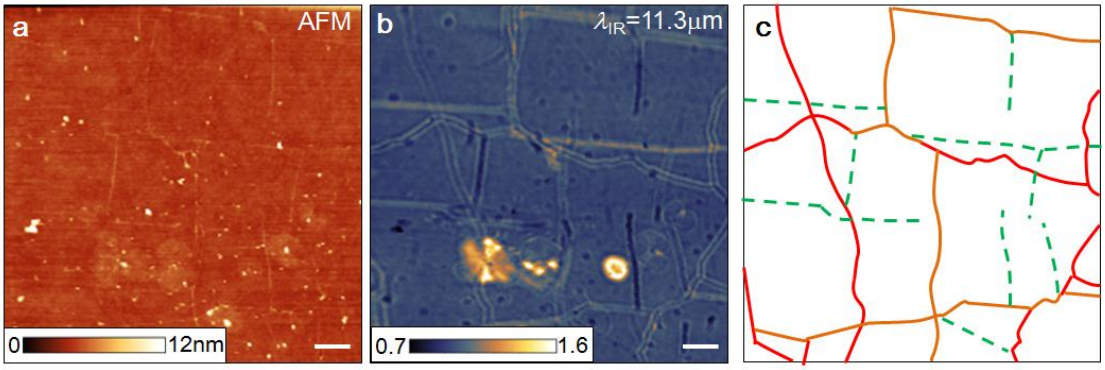

Figure 4.5: Large-area scanning revealing various types of line defects. **a**. AFM topography image. **b**. SPI image simultaneously taken with **a** at λ_{IR}=11.3 μm. **c**. The map of various types of line defects including GBs (red), grain-overlaps (orange), and wrinkles (green). Scale bar width in all the panels is 1 μm.

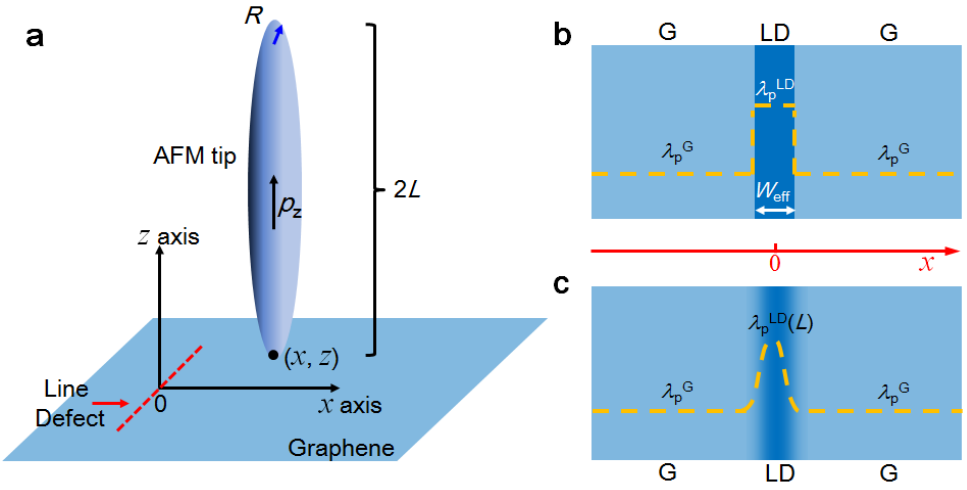

Figure 4.6: Modeling of the AFM tip and graphene. (a) Modeling parameters of the AFM tip. Red dashed line marks a line defect of graphene at x=0. (b) 'Discontinuous' model for a line defect in graphene. (c) 'Gradual' model for a line defect in graphene. 'G' and 'LD' in both (b) and (c) stand for graphene film and line defect, respectively. The fill colors and the yellow dashed lines in both (b) and (c) illustrate the variation of modeling parameters such as λ_p^G (as plotted) or γ_p^G.

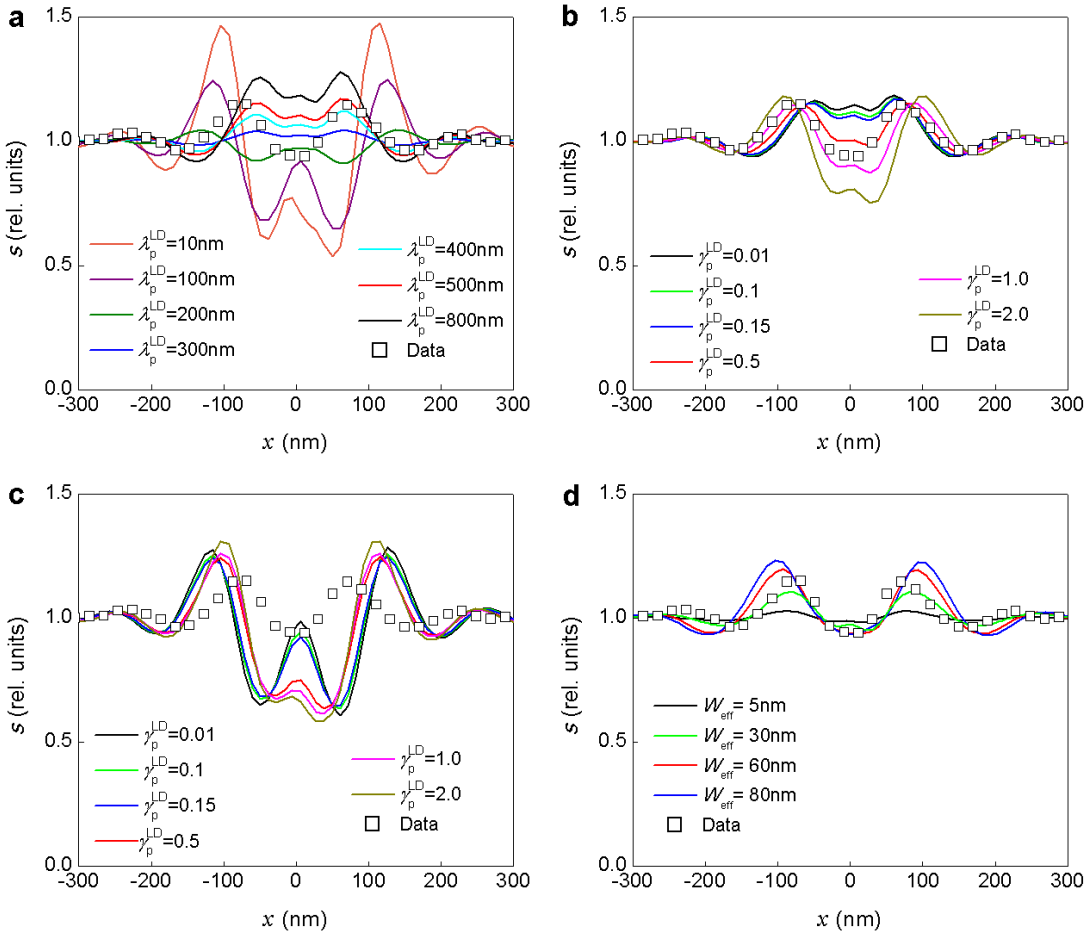

Figure 4.7: Fringe profile simulation with the Discontinuous parameter model. (a) Modeling *s* profiles with 10 nm<λ_p^{LD}<800 nm, γ_p^{LD}=γ_p^{G}=0.15 and W_{eff}≈30 nm. (b) Modeling *s* profiles with 0.01<γ_p^{LD}< 2, λ_p^{LD} =500 nm and W_{eff} ≈30 nm. (c) Modeling *s* profiles with 0.01<γ_p^{LD}< 2, λ_p^{LD} =100 nm and W_{eff} ≈30 nm. (d) Modeling *s* profiles with 5nm< W_{eff} < 90 nm, λ_p^{LD} =500 nm and γ_p^{LD} =1.0. In all panels, λ_p^{G}=260, γ_p^{G}=0.15, the line defect is at *x*=0, and experimental data of a GB taken at 11.26 μm is plotted with black hollow squares. Slightly asymmetry in our modeling results is due to limited resolution of our modeling.

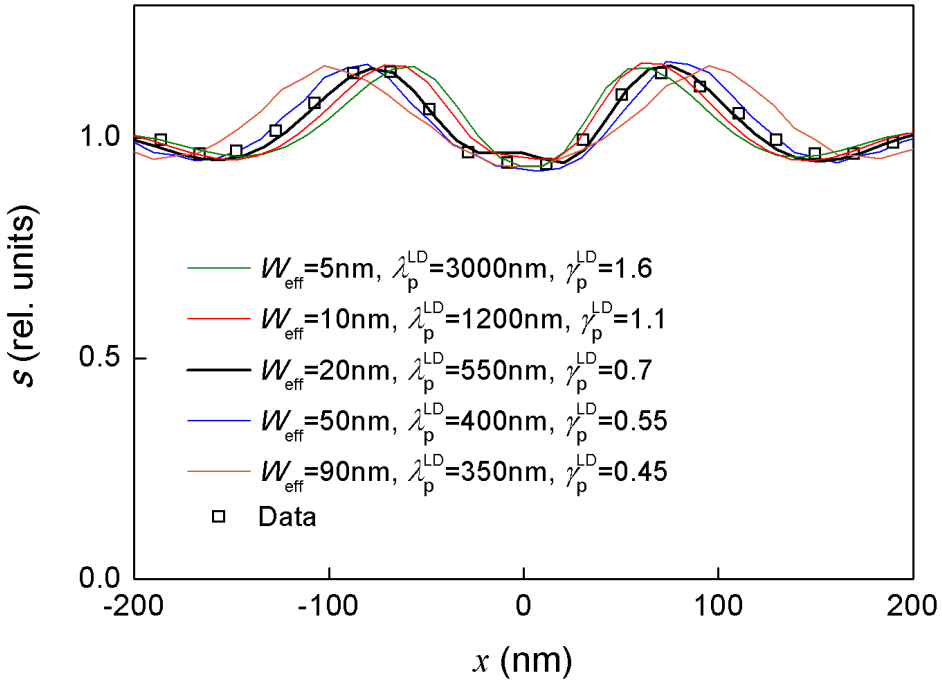

Figure 4.8: Fringe profile fitting with the Discontinuous model. Calculated $s(x)$ profiles for five different effective widths W_{eff} = 5, 10, 20, 50, 90 nm. For each W_{eff}, λ_p^G=260, γ_p^G=0.15 are fixed but λ_p^{LD} and γ_p^{LD} are adjusted to best reproduce the experimental data (squares) taken at 11.26 μm.

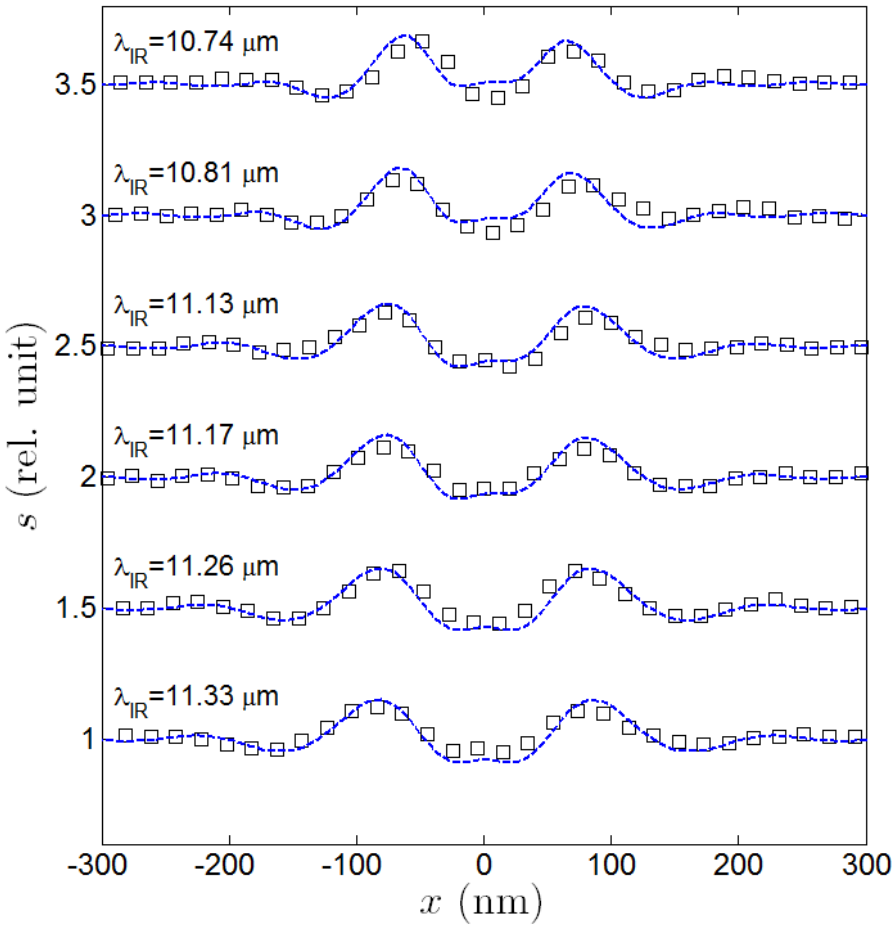

Figure 4.9: Fringe profile fitting with the Gradual parameter model. Line profiles across twin fringes at various λ_{IR} obtained from both experimental data of a GB (black squares) and modeling (blue dashed curve). Here, the scattering amplitude *s* is normalized to that far away from the line defect ($|x| > 300$ nm). All line profiles are vertically displaced for clarity.

4.9 Bibliography

1. A. K. Geim and K. S. Novoselov, Nature Mater. **6**, 183-191 (2007).

2. A. H. Castro Neto, F. Guinea, N. M. R. Peres, K. S. Novoselov, and A. K. Geim, Rev. Mod. Phys. **81**, 109-162 (2009).

3. F. Bonaccorso, Z. Sun, T. Hasan, and A. C. Ferrari, Nature Photon. **4**, 611-622 (2010).

4. A. Vakil and N. Engheta, Science **332**, 1291-1294 (2011).

5. L. Ju, B. Geng, J. Horng, C. Girit, M. Martin, Z. Hao, H. A. Bechtel, X. Liang, A. Zettl, Y. R. Shen, and F. Wang, Nature Nanotech. **6**, 630-634 (2011).

6. Z. Fei, G. O. Andreev, W. Bao, L. M. Zhang, A. S. McLeod, C. Wang, M. K. Stewart, Z. Zhao, G. Dominguez, M. Thiemens, M. M. Fogler, M. J. Tauber, A. H. Castro Neto, C. N. Lau, F. Keilmann, and D. N. Basov, Nano Lett. **11**, 4701-4705 (2011).

7. Z. Fei, A. S. Rodin, G. O. Andreev, W. Bao, A. S. McLeod, M. Wagner, L. M. Zhang, Z. Zhao, M. Thiemens, G. Dominguez, M. M. Fogler, A. H. Castro Neto, C. N. Lau, F. Keilmann, and D. N. Basov, Nature **487**, 82-85 (2012).

8. J. Chen, M. Badioli, P. Alonso-Gonzalez, S. Thongrattanasiri, F. Huth, J. Osmond, M. Spasenovic, A. Centeno, A. Pesquera, P. Godignon, A. Z. Elorza, N. Camara, F. J. G. de Abajo, R. Hillenbrand, and F. H. L. Koppens, Nature **487**, 77-81 (2012).

9. H. Yan, X. Li, B. Chandra, G. Tulevski, Y. Wu, M. Freitag, W. Zhu, P. Avouris, and F. Xia, Nature Nanotech. **7**, 330-334 (2012).

10. A. N. Grigorenko, M. Polini, and K. S. Novoselov, Nature Photon. **6**, 749-758 (2012).

11. M. Jablan, H. Buljan, and M. Slojačić, Phys. Rev. B **80**, 245435 (2009).

12. X. Li, W. Cai, J. An, S. Kim, J. Nah, D. Yang, R. Piner, A. Velamakanni, I. Jung, E. Tutuc, S. K. Banerjee, L. Colombo, and R. S. Ruoff, Science **324**, 1312-1314 (2009).

13. R. Grantab, V. B. Shenoy, and R. S. Ruoff, Science **330**, 946-948 (2010).

14. Y. Wei, J. Wu, H. Yin, X, Shi, R. Yang, and M. Dresselhaus, Nature Mater. **11**, 759-763 (2012).

15. Q. Yu, L. A. Jauregui, W. Wu, R. Colby, J. Tian, Z. Su, H. Cao, Z. Liu, D. Pandey, D. Wei, T. F. Chung, P. Peng, N. P. Guisinger, E. A. Stach, J. Bao, S.-S. Pei, and Y. P. Chen, Nature Mater. **10**, 443-449 (2011).

16. H. S. Song, S. L. Li, H. Miyazaki, S. Sato, K. Hayashi, A. Yamada, N. Yokoyama, and K. Tsukagoshi, Sci. Rep. **2**, 337 (2012).

17. A. W. Tsen, L. Brown, M. P. Levendorf, F. Ghahari, P. Y. Huang, R. W. Havener, C. S. Ruiz-Vargas, D. A. Muller, P. Kim, and J. Park, Science **336**, 1143-1146 (2012).

18. J. C. Koepke, J. D. Wood, D. Estrada, Z.-Y. Ong, K. T. He, E. Pop, and J. W. Lyding, ACS Nano. **7**, 75-86 (2013).

19. L. Tapasztó, P. Nemes-Incze, G. Dobrik, K. J. Yoo, C. Hwang, and L. P. Biró, Appl. Phys. Lett. **100**, 053114 (2012).

20. P. Y. Huang, C. S. Ruiz-Vargas, A. M. van der Zande, W. S. Whitney, M. P. Levendorf, J. W. Kevek, S. Garg, J. S. Alden, C. J. Hustedt, Y. Zhu, J. Park, P. L. McEuen, and D. A. Muller, Nature **469**, 389-392 (2011).

21. K. Kim, Z. Lee, W. Regan, C. Kisielowski, M. F. Crommie, and A. Zettl, ACS Nano **5**, 2142-2146 (2011).

22. D. L. Duong, G. H. Han, S. M. Lee, F. Gunes, E. S. Kim, S. T. Kim, H. Ki, Q. H. Ta, K. P. So, S. J. Yoon, S. J. Chae, Y. W. Jo, M. H. Park, S. H. Chae, S. C. Lim, J. Y. Choi, and Y. H. Lee, Nature **490**, 235-239 (2012).

23. D. W. Ki, Y. H. Ki, H. S. Jeong, and H.-T. Jung, Nature Nanotech. **7**, 29-34 (2011).

24. J. M. Atkin, S. Berweger, A. C. Jones, and M. B. Raschke, Adv. Phys. **61**, 745-842 (2012).

25. J. An, E. Voelkl, J. W. Suk, X. Li, C. W. Magnuson, L. Fu, P. Tiemeijer, M. Bischoff, B. Freitag, E. Popova, and R. S. Ruoff, ACS Nano **5**, 2433-2439 (2011).

26. S. Ryu, L. Liu, S. Berciaud, Y.-J. Yu, H. Liu, P. Ki,, G. W. Flynn, and L. E. Brus, Nano Lett. **10**, 4944-4951 (2010).

27. A. Das, B. Chakraborty, and A. K. Sood, Bull. Mater. Sci. **31**, 579-584 (2008).

28. D. C. Ki, D.-Y. Jeon, H.-J. Chung, Y. Woo, J. K. Shin, and S. Seo. Nanotechnology **20**, 375703 (2009).

29. T. M. Radchenko, A. A. Shylau, and I. V. Zozoulenko, Phys. Rev. B **87**, 195448 (2013).

30. Y.-J. Lu, J. Ki, H.-Y. Chen, C. Wu, N. Dabidian, C. E. Sanders, C.-Y. Wang, M.-Y. Lu, B.-H. Li, X. Qiu, W.-H. Chang, L.-J. Chen, G. Shvets, C.-K. Shih, S. Gwo, Science **337**, 450 (2012).

31. A. C. Ferrari, J. C. Meyer, V. Scardaci, C. Casiraghi, M. Lazzeri, F. Mauri, S.

Piscanec, D. Jiang, K. S. Novoselov, S. Roth, and A. K. Geim, Phys. Rev. Lett. **97**, 187401 (2006).

32. S. Pisana, M. Lazzeri, C. Casiraghi, K. S. Novoselov, A. K. Geim, A. C. Ferrari, and F. Mauri, Nature Mater. **6**, 198-201 (2007).

33. M. Kalbac, A. Reina-Cecco, H. Farhat, J. Kong, L. Kavan, and M. S. Dresselhaus, ACS Nano **4**, 6055-6063 (2010).

34. H. Sojoudi, J. Baltazar, C. Henderson, and S. Graham, J. Vac. Sci. Technol. B **30**, 041213 (2012).

35. W. Zhu, T. Low, V. Perebeinos, A. A. Bol, Y. Zhu, H. Yan, J. Tersoff, and P. Avouris, Nano Lett. **12**, 3431-3436 (2012).

36. B. Sanyal, O. Eriksson, U. Jansson, and H. Grennberg, Phys. Rev. B **79**, 113409 (2009).

Chapter 5

Infrared nano-imaging of surface plasmons in bilayer graphene revealing an effective plasmon-off state

5.1 Introduction

Bernal-stacked bilayer graphene (BLG) has attracted broad interests due to its unique electronic [1-5] and photonic [6-9] properties and potential in a wide range of applications [10,11]. Recently, plasmonic properties of BLG have also attracted research interest [12-17]. Here, we report on infrared nano-imaging of surface plasmons in BLG. We found that BLG supports gate-tunable surface plasmons at mid-infrared frequencies with higher confinement compared to single layer and randomly-stacked double layer

graphene indicating that interlayer tunneling plays an important role in the plasmonic responses. Moreover, we were able to shut off BLG plasmons completely through gating within a wide voltage range close to the charge neutrality point. Theoretical analysis indicates that such a plasmon-off region originates from a gapped insulating state [18.19] and is further extended by interband transitions at mid-infrared frequencies. Our work has uncovers many essential characteristics of BLG plasmons, and demonstrates the feasibility of developing efficient and effective plasmonic transistors and switches [20] using BLG.

5.2 Experimental details

The technique we employed for infrared nano-imaging is an antenna-based nanoscopy built on an atomic force microscope (AFM) operating in the tapping mode. As shown in Fig. 5.1a, the metalized AFM tip is illuminated by infrared light thus generating strong near fields underneath the tip. These fields have a wide range of in-plane momenta q therefore facilitating energy transfer and momentum bridging from photons to plasmons [21,22]. Our samples were fabricated by mechanical exfoliation of bulk graphite and then transferred to SiO_2/Si wafers. The thickness and stacking of the graphene layers were determined through a combination of optical microscopy, AFM and Raman spectroscopy (Fig. 5.5).

5.3 Data and Analysis

5.3.1 Comparison between SLG, BLG and DLG

In Figs. 5.1b-d, we show typical infrared nano-imaging data taken at an excitation frequency of ω_{IR} = 883 cm^{-1}, where we plot the amplitude signal *s* of the back scattered radiation (Methods). We chose sample areas where BLG is adjacent to single-layer graphene (SLG) and randomly-stacked double-layer graphene (DLG). These DLG areas are in fact folded SLG as clearly seen under an optical microscope and further verified by Raman spectroscopy (Fig. 5.5). We emphasize that it is critical to compare SLG, BLG and DLG that are adjacent to each other so that they share identical substrate and environmental conditions. This ensures that the graphene samples will have roughly the same carrier densities due to unintentional doping [23]: an assertion that we have confirmed by gating experiments (Fig. 5.2).

As shown in Fig. 5.1, bright fringes were observed close to the edges of SLG, BLG and DLG. According to previous studies [22, 24-26], such fringes are formed when surface polariton waves launched by the tip interfere with those reflected by edges or defects. These alternating bright and dark fringes have a period $\lambda_p/2$, one half of the polariton wavelength. To verify the plasmonic origin of the fringes observed here, we took imaging data at multiple excitation frequencies. In Figs. 5,1d,e, we present imaging data taken on the same sample area with ω_{IR} = 883 cm^{-1} and 943 cm^{-1}, respectively. One can see clearly that the fringe period shrinks with increasing ω_{IR}, which is consistent with the dispersion of plasmons.

It is evident from Figs. 5.1b-e that the plasmon fringes of the BLG are slightly weaker and narrower than those of SLG, while plasmon fringes of DLG appeared to be much stronger and wider than those of SLG. For the purpose of quantitative comparison, we plot in Fig. 5.1f the line profiles taken perpendicular to edges of SLG, BLG and DLG along the dashed lines shown in Fig. 5.1d. Here, we focus on the plasmon wavelength. The plasmon wavelengths, which are read off directly from the profiles by doubling the fringe period, are 158, 188 and 240 nm for BLG, SLG and DLG, respectively. We want to stress that $\lambda_p^{BLG} < \lambda_p^{SLG} < \lambda_p^{DLG}$ inequality is a common observation for all our graphene samples so long as these graphene layers are adjacent to each other (Table 5.1). Therefore the plasmon confinement factor $C = \lambda_{IR}/\lambda_p$ for surface plasmons in BLG surpasses those of adjacent SLG and DLG. Here $\lambda_{IR} = 1/\omega_{IR}$ is the excitation wavelength.

The dramatic difference between λ_p in BLG and DLG stems from their distinct electronic properties. Unlike Bernal-stacked BLG, the top and bottom layers of DLG are stacked randomly and may also be separated slightly by occasional surface deposits. As a result, interlayer hopping in DLG is strongly suppressed and the interlayer coupling is dominated by Coulomb interaction rather than tunneling. A number of interesting many-body effects have been observed in similar structures, e.g., interlay screening and Coulomb drag [26,27]. The DLG is predicted to have two branches of plasmon modes: 'optical' plasmon ($\omega_p \sim q^{1/2}$) and 'acoustic' plasmon ($\omega_p \sim q$), where ω_p is the plasmon frequency [28]. However, because of small interlayer distance in our sample, the acoustic

mode is very close to the single-particle continuum and is presumably too strongly damped to be observed experimentally. Therefore the plasmons imaged in our DLG are expected to represent the optical mode. According to ref. [28], the ratio between λ_p of DLG (optical mode) and SLG scales as $\lambda_p^{DLG} / \lambda_p^{SLG} \approx (\sqrt{n_{top}} + \sqrt{n_{bot}}) / \sqrt{n_{SLG}}$ in the long wavelength limit. Here, n_{top} and n_{bot} is the carrier density of the top and bottom layer of DLG, and n_{SLG} is the carrier density of SLG. As discussed above, due to their identical environmental conditions, $n_{SLG} \approx n_{top} + n_{bot}$ when SLG is adjacent to DLG, so we have $1 < \lambda_p^{DLG} / \lambda_p^{SLG} < \sqrt{2}$. Our experimental values of $\lambda_p^{DLG} / \lambda_p^{SLG}$ are 1.33 and 1.28 for the two samples shown in Figs. 5.1c,d respectively, which is consistent with the theoretical predictions.

5.3.2 Plasmon-off region of BLG

Analysis of BLG is more complicated than DLG due to interlayer electron hopping that leads to dramatic changes in the electronic structure. We have thus far focused on unintentional doping. In order to get a complete picture of BLG plasmons, it is imperative that we explore a broader parameter space. To this end, we employed back gating to tune both the Fermi energy and bandgap of BLG [3,6-8]. In Figs. 5.2a-e, we show near-field images of a graphene sample containing SLG and BLG taken at various gate voltages. Unless otherwise specified, we discuss mainly the voltage difference $V_g - V_{CN}$ below for the purpose of clarity, where V_g is the bias we applied to the gate and V_{CN}

is voltage for the charge neutrality point (CNP). When $V_g = V_{CN}$, graphene becomes charge neutral and λ_p of SLG drops to the zero. In Fig. 5.2a, both SLG and BLG are highly hole doped ($V_g - V_{CN}$ = -80 V), and we observed plasmon fringes at the edges of both SLG and BLG samples. When the hole doping is decreased, these plasmon fringes first become narrower (Fig. 5.2b, $V_g - V_{CN}$ = -20 V) and then completely disappear close to CNP (Fig. 5.2c, $V_g - V_{CN}$ = 0 V). As $V_g - V_{CN}$ increases to positive values, graphene become electron doped. Here the plasmon fringes in SLG are clearly visible (Fig. 5.2d, $V_g - V_{CN}$ = 20 V), however those in BLG are not observed until $V_g - V_{CN}$ reaches 40 V (Fig. 5.2e). Plasmon fringes of both BLG and SLG become wider and brighter at higher electron doping (Fig. 5.2f, $V_g - V_{CN}$ = 70 V).

Based on our real-space gating data (Fig. 5.2), we extract and plot the complete gate voltage dependence of λ_p in Fig. 5.3a for BLG (red dots, labeled as BLG-1) and SLG (black dots). In addition, we plot data points from another BLG sample (blue dots, labeled as BLG-2). From Fig. 5.3a, one can see that λ_p of all the three samples show obvious ambipolar gate dependence: λ_p increases with both higher electron and hole doping. However, as graphene approaches the CNP, where the carrier density equals to zero, the differences between SLG and BLG appear. For SLG, λ_p drops to zero right at the CNP. In contrast, for BLG, we observed a wide voltage range where there are no detectable plasmons. The width of the plasmon-off region W is 43 $\pm$ 5 V (blue double arrow in Fig. 5.3a) and 60 $\pm$ 5 V (red double arrow in Fig. 5.3a) for BLG-1 and BLG-2,

respectively. The uncertainty of the estimation is primarily due to the spatial resolution (~20 nm) of our technique.

In order to fit the gate-dependence of λ_p, we performed theoretical modeling of both SLG and BLG. The calculation of SLG plasmon wavelength is introduced in detail in previous studies [22,24]. To calculate λ_p of BLG plasmons, we introduced an important parameter V_0 that describes the layer doping asymmetry [29]. The parameter V_0 can be controlled, for example, by top gating [6] or surface molecule doping [3]. In our case, V_0 is a sample-dependent parameter due to dopants and impurities on the graphene-substrate and graphene-air interfaces. Given V_0 other band parameters (Methods), we can determine the band structure [bottom inset of Fig. 5.3b] and Fermi energy E_F of BLG at all gate voltages based on a tight-binding model [30]. We then computed the gate-dependent optical conductivity of BLG using the Kubo formula [29], which allows for direct calculation of λ_p in BLG at any given frequency (Methods). The best agreement with our data for BLG-1 and BLG-2 taken at ω_{IR} = 883 cm^{-1} is obtained with $V_0 = 0.1\gamma_1$ and $V_0 = 0.4\gamma_1$, respectively (Fig. 5.3a). Here, $\gamma_1 \approx 0.4$ eV is the interlayer hopping energy. The difference between BLG-1 and BLG-2 characterized by V_0 manifests itself mainly in the size of the bandgap Δ. As shown in the top inset in Fig. 5.3b, Δ of BLG-2 ($V_0 = 0.4\gamma_1$) is much larger than BLG-1 ($V_0 = 0.1\gamma_1$) close to the CNP. Based on the theoretical curves shown in Fig. 5.3a, we were able to determine the width of the plasmon-off region W at various V_0. In Fig. 5.3b, we plot the V_0-dependence curves of W

at ω_{IR} = 883 cm^{-1} (black solid curve) and found W scales monotonically with V_0. Therefore V_0, hence the bandgap Δ of BLG, can be estimated by measuring the width of the plasmon-off region experimentally and then comparing with the theory curve.

5.3.3 Origin of the plasmon-off region of BLG

In Fig. 5.3b, we also plot the V_0-dependent W curve at ω = 33 cm^{-1} (black dashed curve) which is in the terahertz range – another important regime for graphene plasmonics [31]. The width of the plasmon-off region at ω = 33 cm^{-1} is clearly smaller than that at ω_{IR} = 883 cm^{-1}. To gain a complete picture of the frequency dependence, we show in Figs. 5.4a-c the voltage- and frequency- dependent map of the imaginary part of the optical conductivity $\sigma_2(V_g\text{-}V_{CN}, \omega)$ for SLG, BLG-1 and BLG-2, respectively. According to [22], when the optical conductivity is predominantly imaginary ($\sigma_2 >> \sigma_1 > 0$), surface plasmons can exist and λ_p is roughly proportional to σ_2. Therefore, the red parts ($\sigma_2 > 0$) of the color maps (Figs. 5.4a-c) correspond roughly to the plasmon-on region, while those white and blue parts ($\sigma_2 \leq 0$) are the plasmon-off regions. As a result, the width of the plasmon-off region W at every given frequency can be read out conveniently here. For example, W of BLG-1 and BLG-2 at ω_{IR} = 883 cm^{-1} are defined by the blue and red arrows, respectively.

As can be seen in Figs. 5.4a-c, W increases with frequency for both BLG-1 and BLG-2. We first focus on the low frequency regime ($\omega \rightarrow 0$, e.g. terahertz region) where

Drude response dominates. Here the width of the plasmon-off region W of SLG is zero, making it impossible to turn off plasmons of SLG effectively by gating given the fact that residual conductivity always exists at the CNP – a similar dilemma as that faced by SLG field effect transistors. In contrast, for BLG, when bandgap opens up close to the CNP, an insulating region occurs (between the two black vertical dashed lines in Figs. 5.4b,c) [18,19]. Within such a region, plasmons are off over the entire frequency range. Therefore such a highly insulating region forms the central part of the plasmon-off region. The width of this insulating region W_i is directly related to the bandgap size close to the CNP (top inset of Fig. 5.3), so BLG-2 has a larger W_i than BLG-1.

Now we look at the mid-infrared regime close to our excitation frequencies. Here the plasmon-off region of BLG becomes wider than the insulating region (Figs. 5.4a-c). The widening is primarily due to the interband transitions between the nearest conduction and valence bands (green arrow in the bottom inset of Fig. 5.3b). The threshold frequency of the interband transitions is at $\omega = 2E_F$, where the $\sigma_2(V_g\text{-}V_{CN}, \omega)$ maps show minima (V-shaped blue region in Figs. 5.4a-c) [32]. The $2E_F$ interband transition suppresses σ_2 to negative values and thus extends the plasmon-off region ($\sigma_2 < 0$) further away from the CNP. The width of extended plasmon-off region in gapped BLG is above 30 V for both BLG-1 and BLG-2. Note that the $2E_F$ interband transition also open up a tiny plasmon-off region in SLG (~6 V at $\omega_{IR} = 883$ cm^{-1}, Fig. 5.4a).

To understand better the physical picture of the plasmon-off region, we plot in

Figs. 5.4d-f the frequency (ω) – momentum (q) dispersion diagrams for the surface modes at the graphene/SiO_2 interface at a typical gate voltage V_g-V_{CN} = 15 V (green dashed lines in Figs. 5.4a-c. Here surface plasmons in both BLG-1 and BLG-2 are both turned off at ω_{IR} = 883 cm^{-1} (Fig. 5.3b), but only BLG-2 is on the highly insulating state. The bright curves in these diagrams are dispersion curves for various surface modes. The relatively flat mode above ω = 1100 cm^{-1} is the surface phonon mode of SiO_2, while the mode below following a $q^{1/2}$ scaling is the surface plasmon mode. When these two modes approach each other, an anti-crossing phenomenon occurs due to plasmon-phonon coupling [21, 33]. In the current work, we mainly focused on the graphene plasmon mode. In order for us to launch and detect the plasmon mode, the plasmon dispersion curve should cross the horizontal dashed line, which is set at our excitation frequency ω_{IR} = 883 cm^{-1} (Figs. 5.4d-f). Apparently, only the SLG plasmon mode crosses our excitation frequency (horizontal dashed line), and can therefore be excited (Fig. 5.3a). For BLG-1, the plasmon mode appears at lower frequencies, precluding plasmon excitation at ω_{IR} = 883 cm^{-1}. In the case of BLG-2 that is on the highly insulating state, no plasmon mode can be seen in the entire frequency range.

5.4 Conclusion and Outlook

Our work establishes BLG as a novel plasmonic material with high confinement, wide tunability, and more importantly, the ability to turn on and off surface plasmons

effectively by back gate voltages. The latter unique property makes BLG an ideal material to achieve plasmonic transistors and switches − essential components in future plasmonic circuitry [20]. In addition, the dramatic difference between BLG and DLG plasmons indicates the possibility of achieving novel plasmonic properties by engineering the stacking order of graphene layers. Our work paves the way towards all-graphene integrated plasmonic circuits where SLG, BLG and stacked graphene layers are all functional building blocks.

5.5 Methods summary

5.5.1 Infrared nano-imaging experiments

The infrared nano-imaging experiments in our work were performed using a scattering-type scanning near-field optical microscope (s-SNOM). Our s-SNOM is a commercial system (neaspec.com) equipped with continuous wave mid-IR quantum cascade lasers (daylightsolutions.com) and CO_2 lasers (accesslaser.com). The s-SNOM is based on an atomic force microscope (AFM) operating in the tapping mode with a tapping frequency around 270 kHz and a tapping amplitude around 50 nm. A pseudo-heterodyne interferometric detection module is implemented in our s-SNOM to extract both scattering amplitude s and phase ψ of the near-field signal. In the current work, we discuss mainly the amplitude part of the signal that is sufficient enough. In order to subtract the background signal, we demodulated the near-field signal at the n^{th}

harmonics of the tapping frequency (n = 3 in the current work). All the infrared nano-imaging experiments were performed under ambient conditions and in an atmospheric environment.

5.5.2 Sample fabrication and characterization

Our graphene layers were obtained by mechanical exfoliation of bulk graphite crystals and then transferred to silicon wafers with 300 nm thermal SiO2 on the top. In order to determine the thickness and stacking of the graphene samples, we employed optical microscopy, Raman spectroscopy, and atomic force microscopy (AFM) to characterize all our graphene samples. In Fig. 5.5, we present reprehensive characterization results of the samples shown in Figs. 5.1b,c. The optical microscope images in Figs. 5.5a,d clearly show thickness contrast of the graphene layers including single-layer graphene (SLG), Bernal-Stacking bilayer graphene (BLG) and randomly stacked double-layer graphene (DLG) in the two samples. The DLG is in fact folded SLG as clearly shown in Fig. 5.1d where a triangle shape SLG (originally sitting in the area marked with yellow dashed triangle) was folded to the other side of the sample during exfoliation. Raman spectroscopy data taken on different parts of the samples are shown in Figs.5.5b,e. The 2D peaks at around 2700 cm-1 show clear signatures both the thickness and stacking of graphene layers. For example, both SLG and DLG have symmetric single-component 2D peaks while the Bernal-stacking bilayer graphene has a wider 2D

peak with a featured four-component shape. White dashed squares in Figs. 5.5a,d are the areas we chosen for infrared nano-imaging (Figs. 5.1b,c). Simultaneously collected AFM images in these areas are given in Figs. 5.5c,f, where white dashed lines mark the boundaries between SLG, BLG and DLG.

5.5.3 Calculation of the BLG plasmon wavelength

The plasmon dispersion equation of BLG at the interface between air and SiO_2 substrate with dielectric function $\varepsilon_{\text{sub}}(\omega)$ is given as $q_p = i2\omega\varepsilon_0\kappa(\omega)/\sigma_{BLG}(\omega)$, where $\kappa(\omega) = [1+\varepsilon_{\text{sub}}(\omega)]/2$ is the effective dielectric function of the environment for graphene, $\sigma_{\text{BLG}}(\omega)$ is the optical conductivity of BLG . The plasmon wavelength λ_{p} of BLG can be obtained with $\lambda_{\text{p}} = 2\pi/\text{Re}(q_{\text{p}})$. In order to calculate $\sigma_{\text{BLG}}(\omega)$, we adopted the method from Ref. 29.

5.6 Acknowledgements

Chapter 5, in part, is currently being prepared for submission for publication of material. Z. Fei, E. G. Iwinski, G. X. Ni, L. M. Zhang, W. Bao, A. S. Rodin, Y. Lee, M. Wagner, M. K. Liu, S. Dai, M. D. Goldflam, F. Keilmann, C. N. Lau, A. H. Castro Neto, M. M. Fogler, and D. N. Basov, “Infrared nano-imaging of surface plasmons in bilayer graphene revealing an effective plasmon-off state”. The dissertation author was the primary investigator and author of this paper.

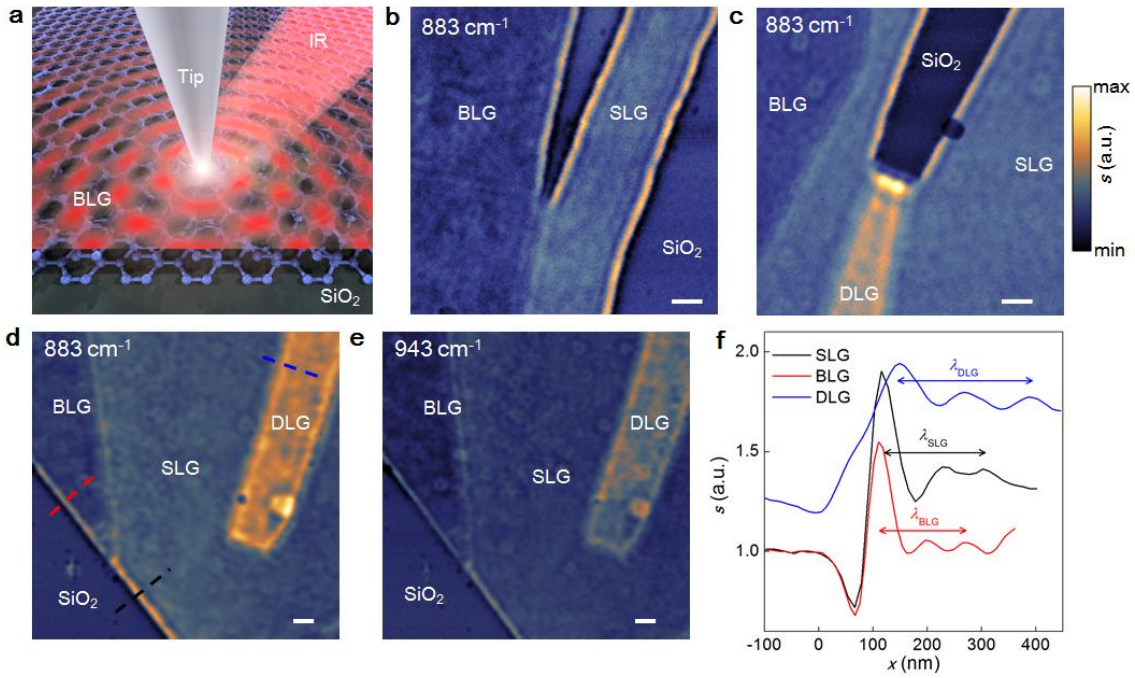

Figure 5.1: Infrared nano-imaging revealing plasmons on BLG, SLG and DLG. (a) Schematics of our infrared nano-imaging experiment. (b-d) Infrared nano-imaging data of graphene samples containing BLG, SLG and DLG taken at an excitation wavelength ω_{IR} = 883 cm^{-1}. (e) Infrared nano-imaging data of the same sample area as (d) taken at ω_{IR} = 943 cm^{-1}. Scale bars, 200 nm. (f) Line profiles taken perpendicular to the edges of BLG (red), SLG (black) and DLG (blue) of the sample in (d). The double-sided arrows mark the width of plasmon wavelength.

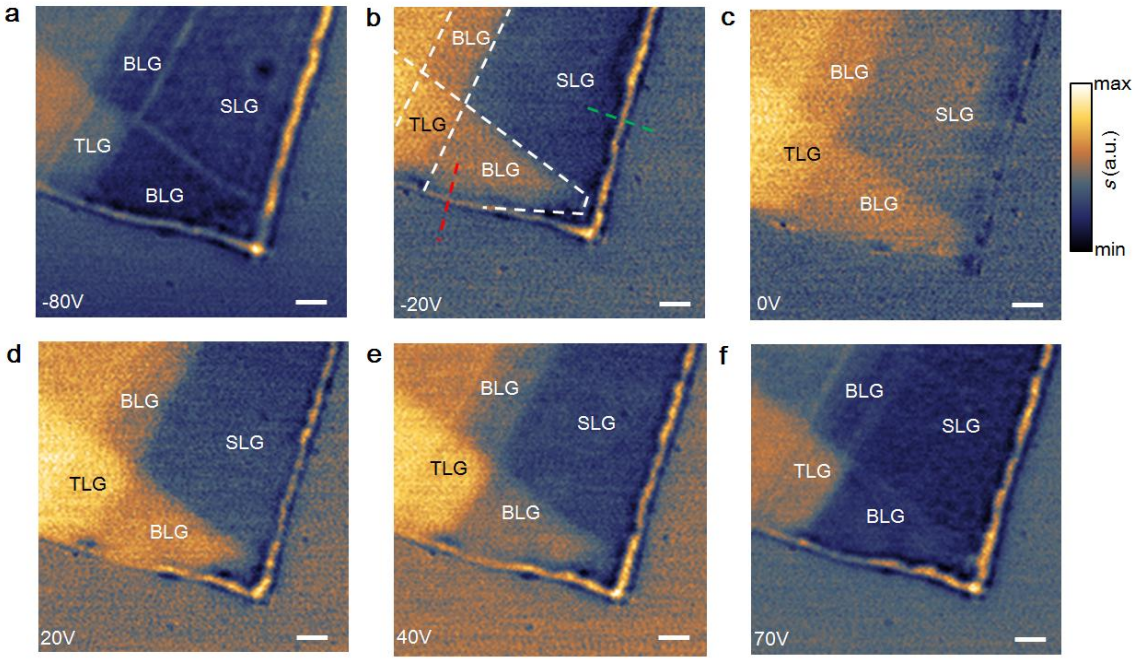

Figure 5.2: Infrared nano-imaging of SLG and BLG under back gating. (a-f) Infrared nano-imaging data of a graphene sample containing BLG, SLG and TLG taken at an excitation wavelength ω_{IR} = 883 cm^{-1} under various gate voltages $V_g - V_{CN}$. Here gate voltages were applied on the silicon side, so positive $V_g - V_{CN}$ will induce electron doping to graphene samples. The white dashed line in b marks the boundary between different graphene layers. Green and red dashed lines in b marks the edges where we measure the plasmon wavelength of SLG and BLG, respectively. Scale bars, 200 nm.

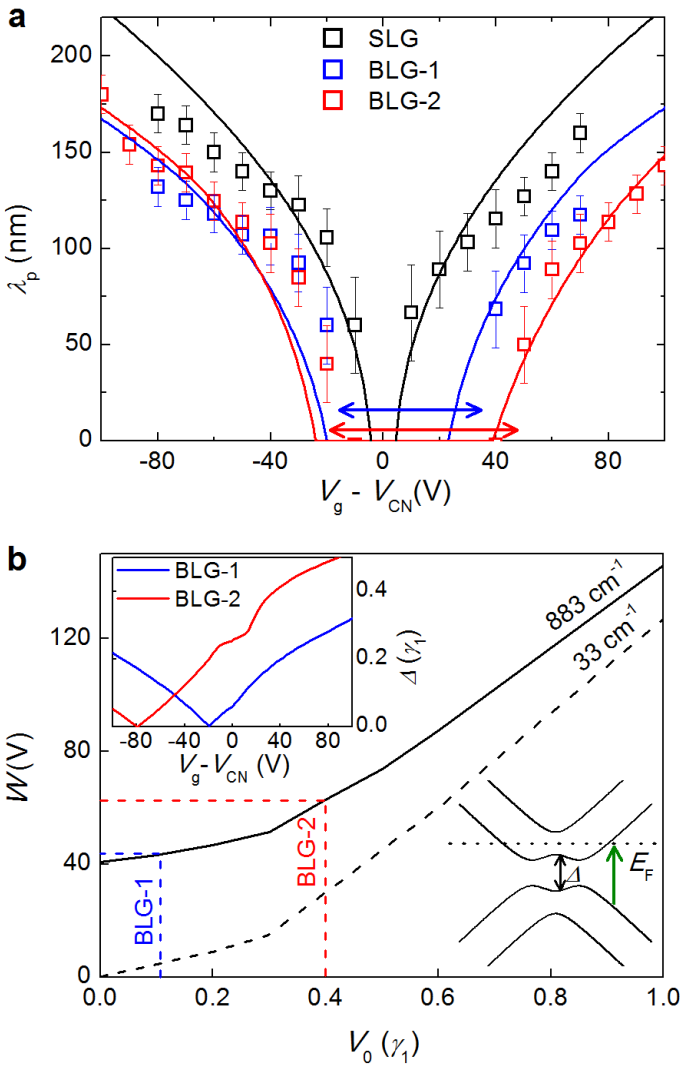

Figure 5.3: Observation of a wide plasmon-off region of BLG. (a) Plasmon wavelength taken from nano-imaging data of SLG and two BLG samples. The SLG (black dots) and BLG-1 (blue dots) data points were extracted from the profiles taken perpendicular to the edges of SLG and BLG in Fig. 5.2 (along dashed color lines as illustrated in Fig. 5.2b). The BLG-2 data points (red dots) were obtained from near-field images of a different sample (Fig. 5.6). Black, blue and red solid curves are theoretical calculations about SLG, BLG with $V_0 = 0.1\gamma_1$ and BLG with $V_0 = 0.4\gamma_1$, respectively. (b) Calculation of the width of the plasmon-off region W versus V_0 of BLG at $\omega = 883$ cm^{-1} (black solid curve) and 33 cm^{-1} (1 terahertz, black dashed curve). By comparing the experimental W with the theory curve, one can estimate V_0 of BLG-1 and BLG-2 (blue and red dashed lines, respectively). Top inset plots the voltage-dependent bandgap Δ of BLG-1 and BLG-2. Bottom inset plots a typical example of the band structure of gapped BLG. For the purpose of illustration, a very large bandgap ($\Delta = \gamma_1$) is used here. The dotted line here denotes the Fermi level and the green arrow illustrates the $2E_F$ interband transition.

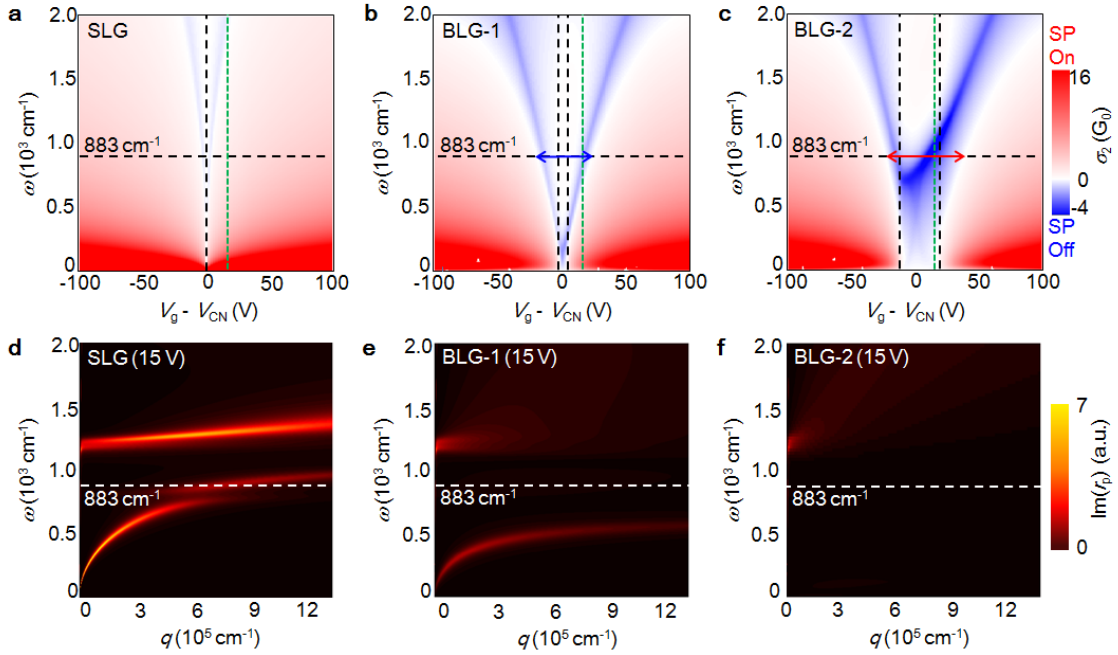

Figure 5.4: Physical picture of the plasmon-off state of BLG. (a-c) Voltage- and frequency- dependent map of the imaginary part of the optical conductivity $\sigma_2(V_g\text{-}V_{CN}, \omega)$ of SLG, BLG-1 and BLG-2. The red/(blue or white) parts of these color maps correspond to on/off state of surface plasmons. The black horizontal dashed line denotes our excitation frequency ω_{IR} = 883 cm^{-1}. The green vertical dashed line marks the gate voltage V_g - V_{CN} = 15 V. The two black vertical dashed lines define the region of the gap-induced high insulating state. The blue and red arrows mark the width of the plasmon-off region at ω_{IR} = 883 cm^{-1} for BLG-1 and BLG-2, respectively. The unit G_0 is $\pi e^2/2h$. (d-f) Dispersion diagrams for surface modes of SLG, BLG-1 and BLG-2 on SiO_2/Si substrate at V_g - V_{CN} = 15 V. Here we plot the imaginary part of the reflection coefficient Im(r_p). Horizontal dashed lines mark our excitation frequency ω_{IR} = 883 cm^{-1}.

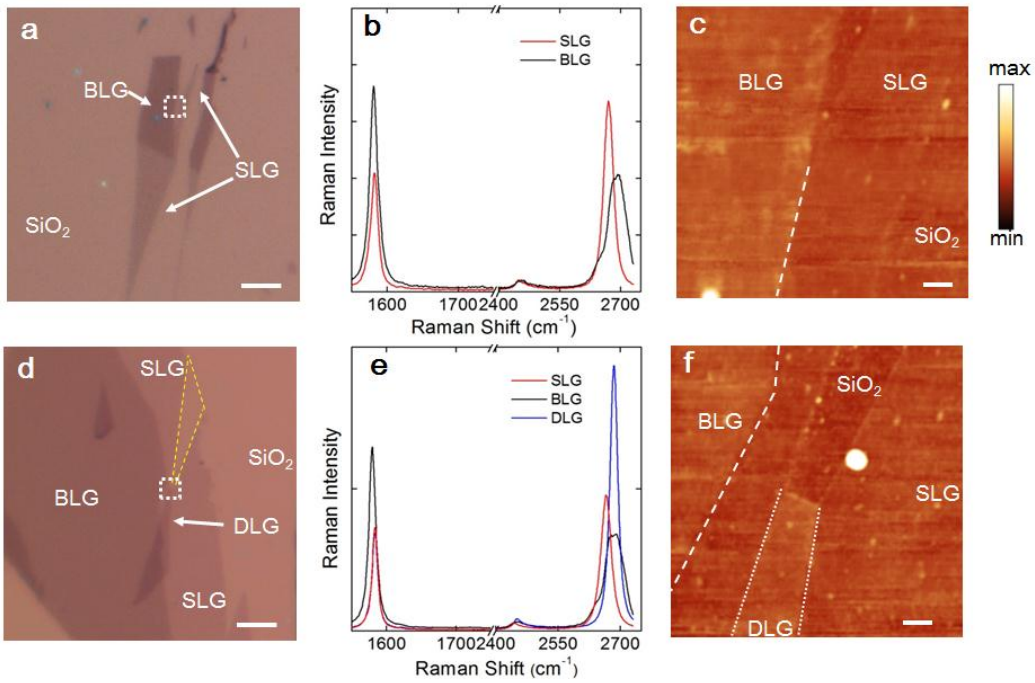

Figure 5.5: Thickness and stacking determination of graphene layers. (a-c) Optical microscopy, Raman spectroscopy and AFM characterization of graphene sample shown in Fig. 5.1b. (d-f) Optical microscopy, Raman spectroscopy and AFM characterization of graphene sample shown in Fig. 5.1c. Dashed squares in (a) and (d) mark the areas we chosen for infrared nano-imaging. Dashed lines in (c) and (f) mark the boundary between SLG and BLG.

5.7 Bibliography

1. K. S. Novoselov, E. McCann, S. V. Morozov, V. I. Fal'ko, M. I. Katsnelson, U. Zeitler, D. Jiang, F. Schedin, and A. K. Geim, Nature Phys. **2**, 177-180 (2006).

2. T. Ohta, A. Bostwick, T. Seyller, K. Horn, and E. Rotenberg, Science **313**, 951-953 (2006).

3. E. V. Castro, K. S. Novoselov, S. V. Morozov, N. M. R. Peres, J. M. B. Lopes dos Santos, J. Nilsson, F. Guinea, A. K. Geim, and A. H. Castro Neto, Phys. Rev. Lett. **99**, 216802 (2007).

4. B. E. Feldman, J. Martin, and A. Yacoby, Nature Phys. **5**, 889-893 (2009).

5. A. S. Mayorov, D. C. Elias, M. Mucha-Kruczynski, R. V. Gorbachev, T. Tudorovskiy, A. Zhukov, S. V. Morozov, M. I. Katsnelson, V. I. Fal'ko, A. K. Geim, and K. S. Novoselov, Science **333**, 860-863 (2011).

6. Y. Zhang, T.-T. Tang, C. Girit, Z. Hao, M. C. Martin, A. Zettl, M. F. Crommie, Y. R. Shen, and F. Wang, Nature **459**, 820-823 (2009).

7. A. B. Kuzmenko, E. van Heumen, D. van der Marel, P. Lerch, P. Blake, K. S. Novoselov, and A. K. Geim, Phys. Rev. B **79**, 115441 (2009).

8. M. F. Mak, C. H. Lui, J. Shan, and T. F. Heinz, Phys. Rev. Lett. **102**, 256405 (2009).

9. Z. Q. Li, E. A. Henriksen, Z. Jiang, Z. Hao, M. C. Martin, P. Kim, H. L. Stormer, and D. N. Basov, Phys. Rev. Lett. **102**, 037403 (2009).

10. F. Xia, D. B. Farmer, Y.-M. Lin, and P. Avouris, Nano Lett. **10**, 715-718 (2010).

11. J. Yan, M-H. Kim, J. A. Elle, A. B. Sushkov, G. S. Jenkins, H. M. Milchberg, M. S. Fuhrer, and H. D. Drew. Nature Nanotech. **7**, 472-478 (2012).

12. G. Borghi, M. Polini, R. Asgari, and A. H. MacDonald, Phys. Rev. B **80**, 241402(R) (2009).

13. X.-F. Wang and T. Chakraborty, Phys. Rev. B **81**, 081402(R) (2010).

14. R. Sensarma, E. H. Hwang, and S. Das Sarma, Phys. Rev. B **82**, 195428 (2010).

15. C. Triola and E. Rossi, Phys. Rev. B **86**, 161408(R) (2012).

16. H. Yan, T. Low, F. Guinea, F. Xia, and P. Avouris, arXiv: 1310.4394 (2013).

17. T. Low, F. Guinea, H. Yan, F. Xia, and P. Avouris, Phys. Rev. Lett. **112**, 116801 (2014).

18. J. B. Oostinga, H. B. Heersche, X. Liu, A. F. Morpurgo, and L. M. K. Vandersypen, Nature Mater. **7**, 151-157 (2007).

19. T. Taychatanapat and P. Jarillo-Herrero, Phys. Rev. Lett. **105**, 166601 (2010).

20. H. A. Atwater, Sci. Am. **296**, 56–63 (2008).

21. Z. Fei, G. O. Andreev, W. Bao, L. M. Zhang, A. S. McLeod, C. Wang, M. K. Stewart, Z. Zhao, G. Dominguez, M. Thiemens, M. M. Fogler, M. J. Tauber, A. H. Castro-Neto, C. N. Lau, F. Keilmann, and D. N. Basov, Nano Lett. **11**(11), 4701-4705 (2011).

22. Z. Fei, A. S. Rodin, G. O. Andreev, W. Bao, A. S. McLeod, M. Wagner, L. M. Zhang, Z. Zhao, G. Dominguez, M. Thiemens, M. M. Fogler, A. H. Castro-Neto, C. N. Lau, F. Keilmann, and D. N. Basov, Nature **487**, 82–85 (2012).

23. J. Chen, M. Badioli, P. Alonso-Gonzalez, S. Thongrattanasiri, F. Huth, J. Osmond, M. Spasenovic, A. Centeno, A. Pesquera, P. Godignon, A. Z. Elorza, N. Camara, F. J. G. de Abajo, R. Hillenbrand, and F. H. L. Koppens, Nature **487**, 77-81 (2012).

24. Z. Fei, A. S. Rodin, W. Gannett, S. Dai, W. Regan, M. Wagner, M. K. Kiu, A. S. McLeod, G. Dominguez, M.Thiemens, M. M. Fogler, A. H. Castro-Neto, F. Keilmann, A. Zettl, R. Hillenbrand, M. M. Fogler, and D. N. Basov, Nature Nanotech. **8**, 821-825 (2013).

25. S. Dai, Z. Fei, A. S. Rodin, W. Gannett, M. Wagner, W. Regan, A. S. McLeod, M. K. Liu, M. Thiemens, G. Dominguez, A. H. Castro-Neto, A. Zettl, F. Keilmann, M. M. Fogler, and D. N. Basov, Science **343**, 1125-1129 (2014).

26. L. A. Ponomarenko, A. K. Geim, A. A. Zhukov, R. Jalil, S. V. Morozov, K. S. Novoselov, I. V. Grigorieva, E. H. Hill, V. V. Cheianov, V. I. Fal'ko, K. Watanabe, T. Taniguchi, and R. V. Gorbachev, Nature Phys. **7**, 958 (2011).

27. R. V. Gorbachev, A. K. Geim, M. I. Katsnelson, K. S. Novoselov, T. Tudorovskiy, I. V. Grigorieva, A. H. MacDonald, S. V. Morozov, K. Watanabe, T. Taniguchi, and L. A. Ponomarenko, Nature Phys. **8**, 896 (2012)

28. E. H. Hwang and S. Das Sarma Phys. Rev. B **80**, 205405 (2009).

29. L. M. Zhang, Z. Q. Li, D. N. Basov, M. M. Fogler, Z. Hao, and M. C. Martin, Phys. Rev. B **78**, 235408 (2008).

30. E. McCann, Phys. Rev. B **74**, 161403(R) (2006).

31. L. Ju, B. Geng, J. Horng, C. Girit, M. Martin, Z. Hao, H. A. Bechtel, X. Liang, A. Zettl, Y. R. Shen, and F. Wang, Nature Nano. **6**, 630-634 (2011).

32. Z. Q. Li, E. A. Henriksen, Z. Jiang, Z. Hao, M. C. Martin, P. Kim, H. L. Stormer and D. N. Basov, Nature Phys. **4**, 532-535 (2008).

33. M. Wagner, Z. Fei, A. S. McLeod, A. S. Rodin, W. Bao, E. G. Iwinski, Z. Zhao, M. Goldflam, M. Liu, G. Dominguez, M. Thiemens, M. M. Fogler, A. H. Castro Neto, C. N. Lau, S. Amarie, F. Keilmann, and D. N. Basov, Nano Lett. **14**, 894-900 (2014).